Montanuniversität Leoben

Oxide-based Coatings Deposited by Thermal CVD

Diploma thesis

by

Christoph Czettl

Accomplished at the Department of Physical Metallurgy and Material Testing at the University of Leoben in cooperation with Materials Center Leoben

Leoben, May 2007

Eidesstattliche Erklärung

Ich erkläre an Eides statt, dass ich die vorliegende Arbeit selbstständig und ohne fremde Hilfe verfasst, andere als die angegebenen Quellen und Hilfsmittel nicht benutzt, wörtlich und inhaltlich entnommene Stellen als solche erkenntlich gemacht habe.

Christoph Czettl

Leoben, Mai 2007

Acknowledgements

I would like to thank Univ. Prof. DI Dr. Helmut Clemens for his support and comity, for giving me the opportunity to perform this thesis at the Department of Physical Metallurgy and Materials Testing at the University of Leoben.

My sincerest gratitude appertain the head of Thin Film Group, ao. Prof. DI Dr. Christian Mitterer for the faith, shown by admitting me to his group. Furthermore for his kindness, his patience and the interesting discussions. This enlarged my experiences and helped to evaluate results from another point of view.

I am grateful to ao. Univ. Prof. Reinhold Ebner, Managing Director of the Materials Center Leoben (MCL), who assigned me to this project and to all co workers at the Materials Center Leoben.

I would like to express my thanks to DI Dr. Martin Kathrein of Ceratizit Austria in Reutte for the interesting conversations and in particular for possibility to get an insight in the world of hard materials.

I am thankful for the support of DI Dr. Hans-Peter Martinz of Plansee SE for his assistance and promotion. The numerous discussions enriched my understanding of chemical fundamentals and their influence on corrosion protection.

My sincerest appreciation and gratitude is due to my supervisor DI David Hochauer for the backup and assistance during this thesis. Especially for the patience and time which was necessary to evaluate the voluminous analytical results and the long conversations to give each statement the adequate emphasis.

I would also appreciate the aid of Brigitte Nigg for her support and care during the experiments and Karl Gigl for the interesting discussions which brought the experiments close to production process.

Further I want give credit to MSc. Marianne Penoy for performing the GDOES and XRD measurements at Ceratizit Luxembourg and Gerhard Hawranek and Wilhelm Birzer for performing the SEM investigations at Plansee SE Reutte and Department of Physical Metallurgy and Materials Testing in Leoben, respectively.

Finally, I owe special gratefulness to my family and friends for their encouragement and advice. Their subsistence is the most important thing for me.

Table of contents

1 Introduction

The performance of modern materials is not only related to high-tech bulk materials. The surface of these materials has a fundamental influence on properties like corrosion resistance, wear and friction behaviour, electrical and thermal conductivity, photoluminescence, magnetic, dielectric properties and optical properties. These can be beneficially influenced by surface modification or coatings. Many different coating technologies in a wide temperature range have been developed in the last century. Fig. 1.1 gives some examples of possible surface treatments and coatings [1-3].

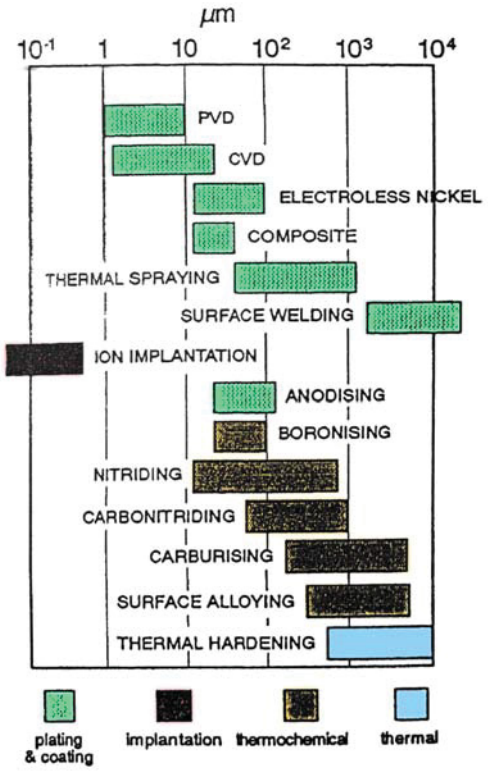

Fig. 1.1: Examples for various coatings and surface treatments and the respective thickness of the effected surface zone [3]

In particular, coatings of borides, carbides, nitrides and oxides are manufactured by deposition processes like physical vapour deposition (PVD) or chemical vapour deposition (CVD). These coatings can be used singularly or in combination as multilayer coatings. The latter can be designed specifically to exhibit best performance in the desired application. Coatings composed of numerous layers are documented in literature [3, 5]. There is a wide range of application, especially in the metal cutting and the metal forming industry, but also for high temperature corrosion protection, which are of main interest for this thesis.

Within the group of deposition techniques, different temperature ranges can be distinguished. Thermal CVD and PVD represent the upper and the lower temperature range, respectively. Deposition temperatures for PVD vary from 300 to 600 °C, unlike CVD processes where temperatures from 600 to 900 °C for moderate temperature CVD (MT-CVD) and 900 to 1100 °C for high temperature CVD (HT-CVD) are applied. Plasma assisted CVD processes (PA-CVD) enable lower deposition temperatures, which are essential for depositing coatings on temperature sensitive substrate materials, for example electronic devices like random access memories, transistors or other semiconductors. Fig. 1.2 illustrates the coherences of main parameters, temperature and pressure, for the above mentioned deposition processes [1, 2, 6].

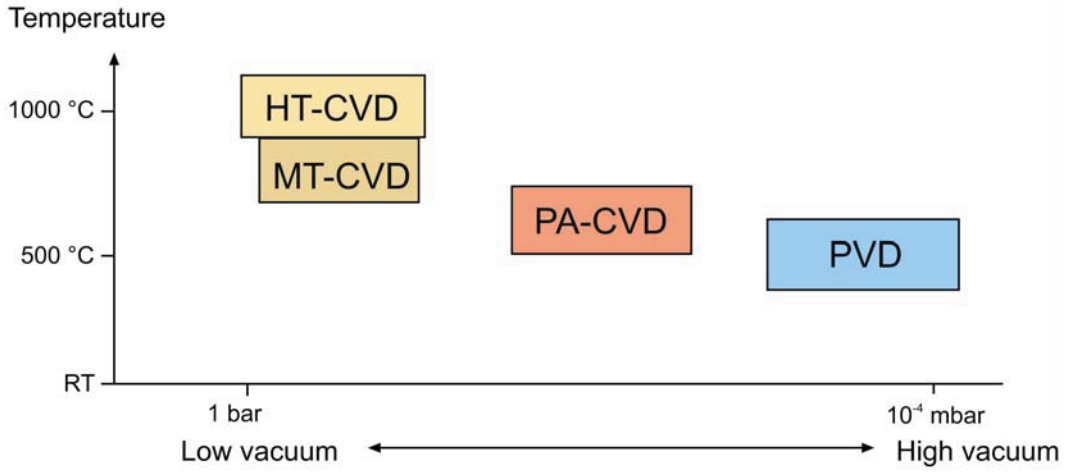

Fig. 1.2: Relationship of hard coating processes and main parameters [6]

Thermal deposition processes like CVD enable growth under thermodynamic equilibrium condition and respectively in commonly stable structures. The residual stress level is low compared to low temperature processes. A laminar gas stream, simple substrate arrangement and big loads as well as reasonable costs are the main advantages. In comparison to CVD, high vacuum is necessary for plasma assisted processes. Additionally, PVD is a line-of-sight-process, therefore sophisticated substrates fixturing and rotation is required. Substrates are exposed to high ion bombardment; thus deposited layers show commonly metastable structures and high compressive residual stress. The flexibility of using a wide range of precursor materials such as halides, hydrides, organometallics in combination with a huge material spectrum, including metals, carbides, nitrides, oxides, sulphides, III-V and II-VI elements, are other reasons for the wide application of CVD. Higher deposition rates can be reached and also thicker coatings can be applied, compared to PVD [2, 7, 8].

Within this thesis, the fundamentals of the CVD process for alumina deposition will be discussed, including thermodynamics, mass transport, kinetics, nucleation, growth and the evolution of structure. Also response will be given to the influence of process parameters like deposition temperature, feed gas composition and to the influence of additional elements on growth of alumina coatings. Starting with downscaled industrial deposition parameters for alumina deposition, used as reference, further elements are inserted in the deposition chamber and the effects of parameter variations are observed. Finally, the coatings are analysed and results brought in relation to process parameters and element contents.

The aim of this thesis is to investigate modifications of an aluminium oxide based layer grown by thermal chemical vapour deposition. Improvements should be caused by additional elements and variation of deposition conditions. Finally, this work should enlarge the understanding of complex CVD procedures and lead to controllable layer deposition and structure evolution.

2 Theoretical fundamentals

2.1 CVD process

Coatings deposited via the CVD process are used for many different applications like wear and corrosion resistant coatings, optical layers, in case of their dielectrical or conducting properties as well as diffusion barriers. Different types of processes have been developed during the last few decades, which can mainly be distinguished by the applied temperature, pressure and kind of precursors. Low pressure regime e. g. applied for random access memories, medium and atmospheric pressure CVD are commonly used. Low pressure – low temperature processes are usually assisted by additional stimulation like plasma or laser. Precursors can be separated in chloride species, metal organic ones and metal vapour phase. For the deposition of wear and corrosion resistant coatings on cemented carbide or refractory materials, commonly the high temperature atmospheric pressure CVD process is applied (cf. Fig. 2.1) [7, 8].

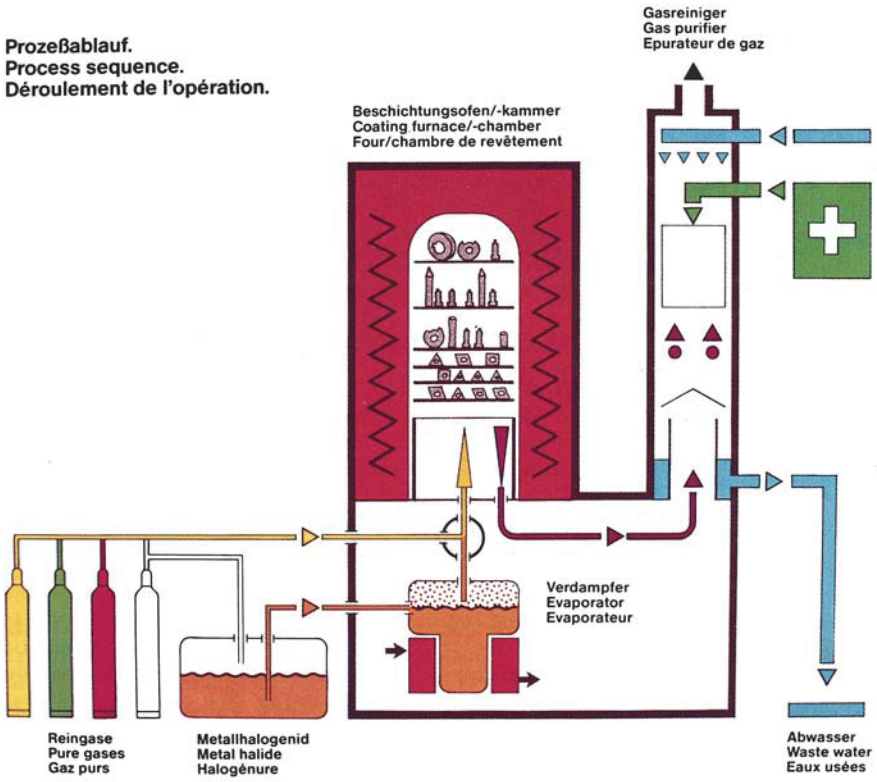

Fig. 2.1: Production high temperature atmospheric pressure CVD reactor for the coating of cutting tools [9]

2.1.1 Thermodynamics

The workflow of the CVD process can be sectioned into various parallel and serial reactions. Which ones of them take place, and which ones are significant for the process can be estimated using thermodynamic calculations. Each chemical system is anxious to minimize its total energy. A thermodynamic potential called Gibbs free energy G is used to calculate the potential energy of species depending on pressure p and temperature T. This potential can be derived from the first and second law of thermodynamics. The first one, as written in Eq. 2.1, specifies the interistic energy U as a combination of system-performed work W and latent heat Q. Eq. 2.2 shows the entropy S in dependency of temperature and latent heat, which is the second law. Eq. 2.3 is necessary for relating pressure and volume change dV to the reversible work W_{rev} of the volume. Combinations of these equations lead to the change of intrinsic energy U, which is a thermodynamic potential and entropy S and temperature (Eq. 2.4) [7, 10].

$$dU = \delta W + \delta Q \tag{2.1}$$

$$dS \geq \delta Q / T \,,\, dS = \delta Q_{rev} / T \tag{2.2}$$

$$dW_{rev} = -p\, dV \tag{2.3}$$

$$dU\,(S,V) = T\,(S,V)\, dS - p\,(S,V)\, dV \tag{2.4}$$

The couples of variables entropy-temperature and pressure-volume are conjugated variables. Hence, the change of intrinsic energy can be transformed into two further potentials, describing the same energy state. This can be done by the addition of $(pV)'$ which results in the potential H, shown in Eq. 2.5. Further addition of $(-TS)'$ yields the Gibbs free energy, mentioned above (Eq. 2.6) [7, 10].

$$dH\,(S,p) = T\,(S,p)\, dS + V\,(S,p)\, dp \tag{2.5}$$

$$dG\,(p,T) = -S\,(T,p)\, dT + V\,(T,p)\, dp \tag{2.6}$$

The last conversion step can also be written as Eq. 2.7. Based on standard data of enthalpy and entropy at defined temperature and pressure, the Gibbs energy of species in relation to applied pressure and temperature can be calculated.

$$G = H - TS \tag{2.7}$$

Subtracting the Gibbs energy of educts E_{ed} from the Gibbs energy of products E_{pr} gives the free energy change ΔG, shown in Eq. 2.8. This value is zero at equilibrium, while a negative value indicates a feasible reaction. Computer programs like HSC-Chemistry [11] use the minimisation of Gibbs free energy for calculating the composition of species and phase equilibrium. By dint of this, we can expect which reactions will take place, if mass transport and kinetics allow this [7, 10].

$$\Delta G = G_{pr} - G_{ed} \tag{2.8}$$

2.1.2 Mass transport and kinetics

Species used for a CVD process must be brought to the substrate surface, where they adsorb and form the desired deposit. Introduced educts are transported due to complicated fluid dynamics, caused by the inlet pressure of gases and reactor geometry. The transportation can be divided in the following intermediate steps:

- diffusion of educts through the boundary layer
- adsorption of reactants on the surface
- chemical reactions
- desorption of gaseous by-products
- diffusion of gaseous by-products through the boundary layer

Also gas phase reactions take place resulting in intermediate species which diffuse to the surface. Furthermore, these reactions can cause homogenous nucleation and the formation of powder, which is undesired in the case of depositing coatings. For layer production, nucleation and growth is mainly influenced by the composition of feed gas and deposition temperature. The above mentioned processes are illustrated schematically in Fig. 2.2. The rate-limiting step is determined either by surface reaction kinetics or mass transport limitations [7, 12].

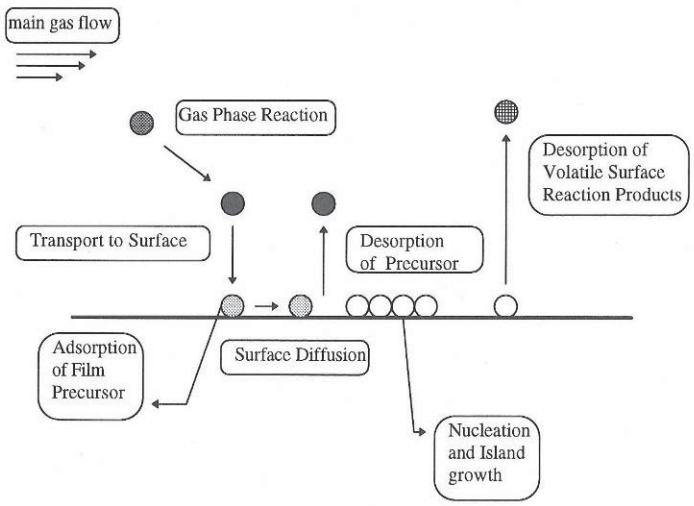

Fig. 2.2: Transport and reaction processes in CVD [12]

Deposition pressure and temperature determine which of the above mentioned mechanisms is the bottleneck of the reaction chain. Boundary layer thickness Δ is a demonstrative parameter, which can be calculated using the distance from the inlet x in flow direction and the Reynolds' number Re (cf. Eq. 2.9). This term depends on mass density ρ, flow density u_x and viscosity μ, according to Eq. 2.10.

$$\Delta = \sqrt{\frac{x}{\mathrm{Re}}} \qquad 2.9$$

$$\mathrm{Re} = \frac{\rho u_x}{\mu} \qquad 2.10$$

Describing the transport and reaction process, two extreme cases can be distinguished. At constant mass flow rate, low pressure causes high gas velocity which results in a thin boundary layer. Therefore, reactants could migrate quickly through it, and a surplus of species is adsorbed at the substrate surface. The limiting step is the low surface reaction additionally favoured by low temperature. This case is illustrated in Fig. 2.3 a.

If higher pressure is applied, the gas velocity is comparatively lower and the boundary layer thickness increases. Hence, less precursor is transported through the boundary layer. In case of high temperature, the surface reaction takes place immediately, so there is no surplus of adsorbed species, as shown schematically in Fig. 2.3 b [7, 8].

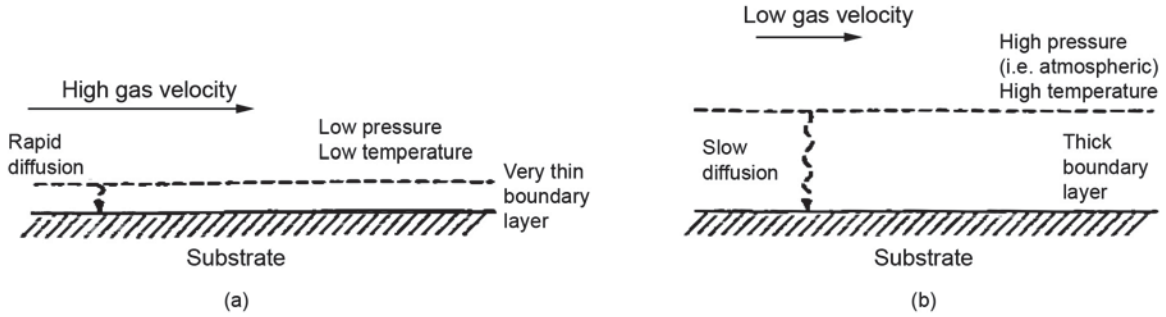

Fig. 2.3: Examples for mass surface kinetic limited process (a) and transport limited process (b) [7]

Carlsson et al. [13] illustrated these limitations by an Arrhenius plot of logarithmic deposition rate versus inverse temperature, using different pressures. There the coherences are linear, with different slopes for mass transport and surface reaction limited regime, as can be seen in Fig. 2.4.

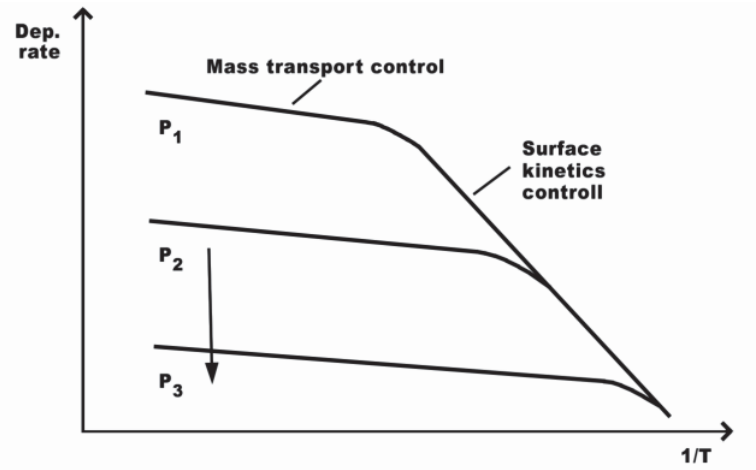

Fig. 2.4: Regions of mass transport limitation (high p and T) and surface kinetics control (low p and T) at different total pressures ($P_1<P_2<P_3$) [13]

2.1.3 Free radical chain mechanism

Coatings which were deposited within this thesis consist mainly of aluminium oxide. Because of the quantity of possible precursors and gas phase reactions, useable for the CVD process, only transport and deposition of the predominant aluminium species will be discussed in detail. The behaviour of this species is comparable to other elements, as documented for tantalum [14] and for the example of yttrium [15].

Reaction paths described by a free-radical chain mechanism lead to a better appreciation of operation during gas decomposition and deposition. The over all reactions can be summarised as shown in Eq. 2.11 and Eq. 2.12 [16, 17].

2.1.3.1 Decomposition of $AlCl_3$

For the generation of water gas, different reaction paths are possible. Because of its long reaction time, the classical water gas reaction according to Eq. 2.11 is obviously not responsible for the formation of main water gas amounts in the CVD process. Investigations and modelling of the $AlCl_3$ decomposition showed a very complex network of radical species reactions. The amount of H_2O reacting along the classical way (red lines), illustrated in Fig. 2.5, is relatively small. The predominant portion is produced according to Eq. 2.13, Eq. 2.14 and Eq. 2.15 (orange lines). Also the classical surface reaction (Eq. 2.12) can be divided into radical reaction paths as mentioned in section 2.1.3.2 [16, 18].

Gas reaction

$$H_2(g)+CO_2(g)\leftrightarrow H_2O(g)+CO(g) \qquad 2.11$$

Surface reaction

$$2\,AlCl_3+3\,H_2O\leftrightarrow Al_2O_3+6\,HCl \qquad 2.12$$

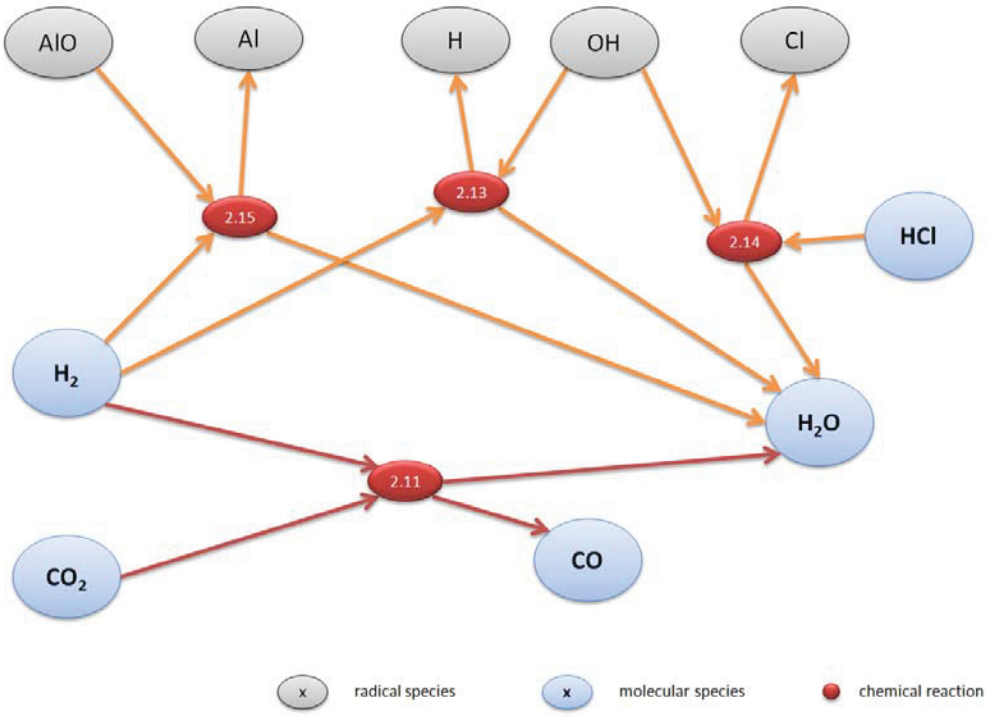

Fig. 2.5: Reaction paths according to free radical theory

$$H_2 + OH \leftrightarrow H_2O + H \quad 2.13$$

$$HCl + OH \leftrightarrow H_2O + Cl \quad 2.14$$

$$AlO + H_2 \leftrightarrow Al + H_2O \quad 2.15$$

It can be shown that AlClO is the major intermediate species which is produced by $AlCl_3$ decomposition corresponding to Eq. 2.16. Sotirchos et al. [18] and Catoire et al. [16] documented a more complex reaction path for generating radical species caused by $AlCl_3$ decomposition. Fig. 2.6 shows only one chain of this network, where AlClO and water gas as well as radical species were generated starting from $AlCl_3$.

$$AlCl_3 + CO_2 + H_2 \leftrightarrow AlClO + CO + 2\,HCl \quad 2.16$$

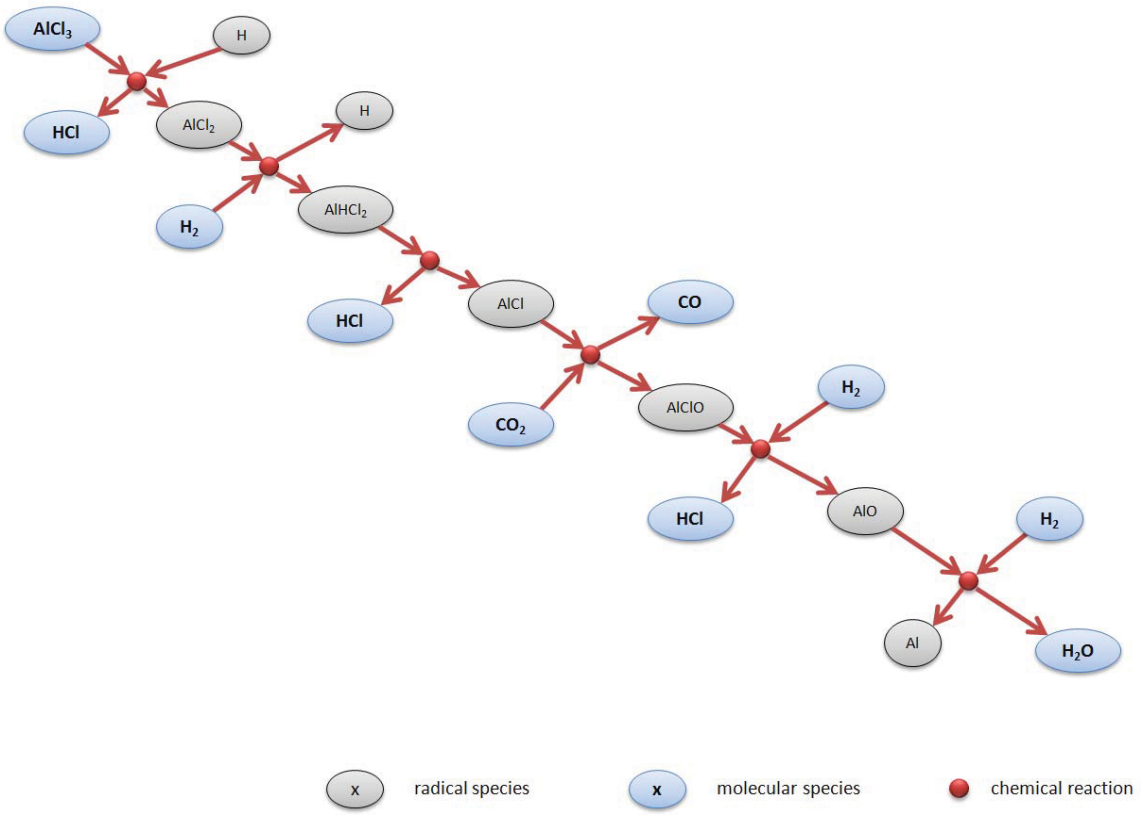

Fig. 2.6: Generation of AlClO and water gas

The $AlCl_3$ decomposition is strongly influenced by the hydrogen content in the feed gas. Increased amounts lead to higher decomposition rates, as shown in the calculated profiles (cf. Fig. 2.7).

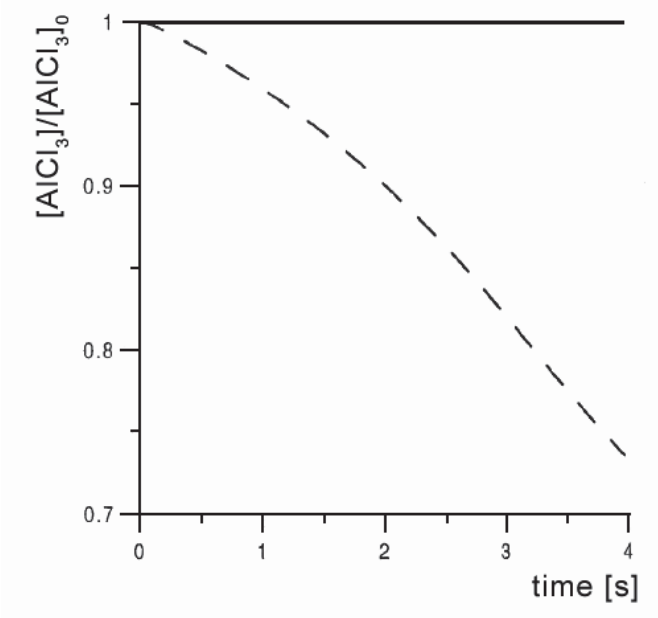

Fig. 2.7: Calculated $AlCl_3$ decomposition for the mixture 2 mol % $AlCl_3$ + 2 mol % CO_2 in Ar (full line) and for the mixture 2 mol % $AlCl_3$ + 2 mol % CO_2 in H_2 (dashed line). Total pressure in both mixtures 100 mbar at 1323 K [16]

The influence of HCl in feed gas is complex and does not cause big changes up to 10 % total amount. HCl addition of more than 4 % influences the equilibrium of $AlCl_3$ decomposition negatively. Coherences are illustrated in Fig. 2.8 [16, 17, 19].

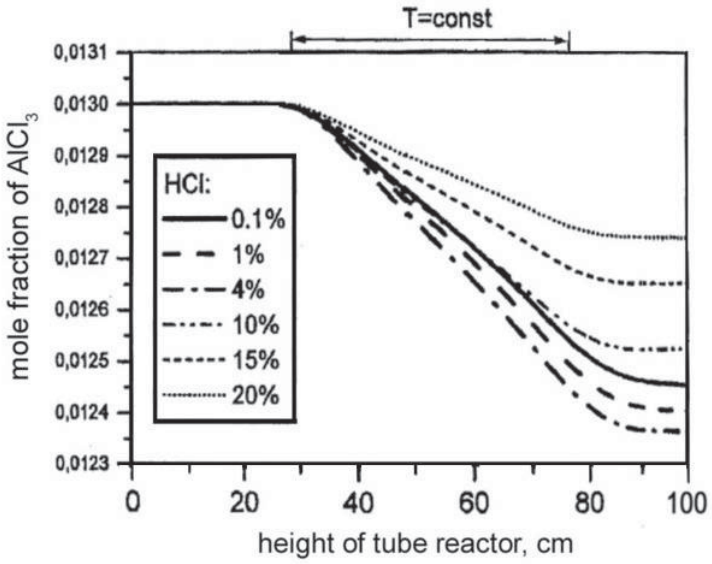

Fig. 2.8: $AlCl_3$ profiles; feed gas (mol %): 4 CO_2; 60 H_2; variable HCl; flow rate 20 slh [17]

2.1.3.2 Deposition of Al_2O_3

For formation of oxidic surface layers out of gaseous or adsorbed species, a reaction of aluminium and oxygen containing species must take place. The oxygen which is necessary for the formation of aluminium oxide on the substrate surface is supplied by water gas and OH-radicals. The previously shown overall surface reaction Eq. 2.12 can be fragmented as illustrated in Fig. 2.9. One essential step in this model is the generation of aluminium oxide from adsorbed surface species following Eq. 2.17. Free active surface sites, necessary for adsorption of species are neglected in this scheme [18].

$$[AlClO]_S + [AlHO_2]_S \rightarrow Al_2O_3 + HCl \qquad 2.17$$

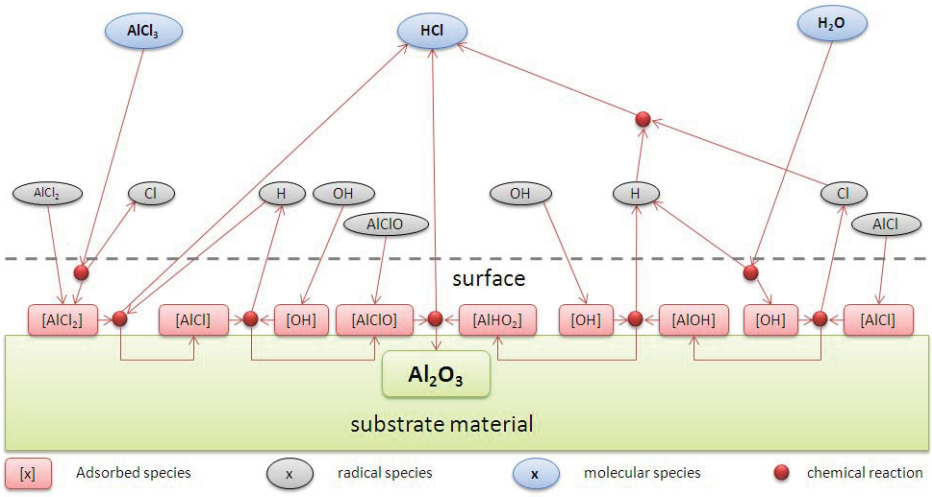

Fig. 2.9: Deposition of Al_2O_3 on the substrate surface out of gaseous and adsorbed species

2.1.4 Evolution of structure

In which shape and size grains are arranged on the surface is essential for properties of the coating as well as adherence. Fig. 2.10 gives an overview of grain structure evolution during deposition of polycrystalline thin films, and illustrates the main steps of layer growth. Those are nucleation and growth, coalescence, formation of a surface covering layer and increase of layer thickness.

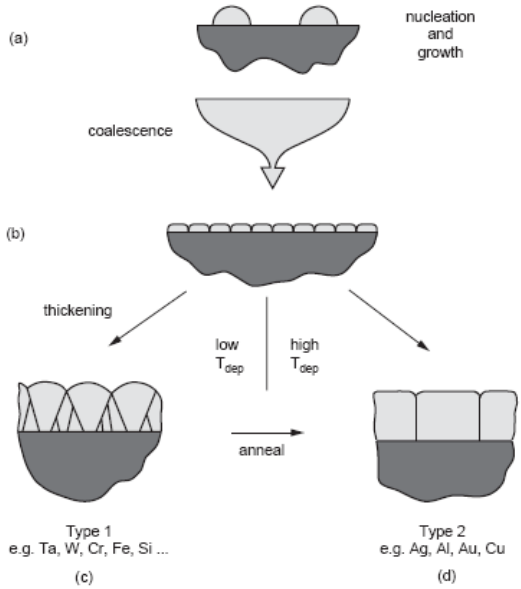

Fig. 2.10: Overview of grain structure evolution during deposition of polycrystalline thin films; coalescence (a), thickening (b), structure type 1 (c) and structure type 2 (d) [20]

The first step in evolution of structure is the transport and adsorption or condensation on surface sites. This depends strongly on kinetics and mass transport, influenced by process temperature and pressure as discussed above. A sufficient agglomeration of species is necessary to form nuclei of critical size, whose growth is energetically favourable. If the critical radius is exceeded, the free energy profit by formation of volume is higher than the energy needed for forming the surface. The coherences for homogeneous nucleation out of the gas phase are shown principally in Fig. 2.11 [20].

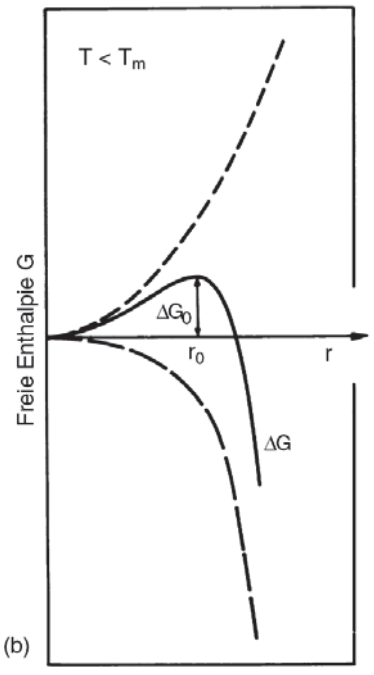

Fig. 2.11: Critical nuclei ratio [21]

In case of heterogeneous nucleation, desired for the CVD process, the necessary energy is partly generated by substrate surface according to Eq. 2.18, where ΔG stands for the Gibbs free energy, ΔG_V for the free energy change per unit volume, γ for the interface tensions, indexed by f for film, s for substrate and v for vapour. r specifies the nuclei radius, and a_1, a_2, a_3 are geometric constants depending on the contact angle Θ, as can be seen in Fig. 2.12.

$$\Delta G = a_3 r^3 \Delta G_V + a_1 r^2 \gamma_{vf} + a_2 r^2 \gamma_{fs} - a_2 r^2 \gamma_{sv} \qquad 2.18$$

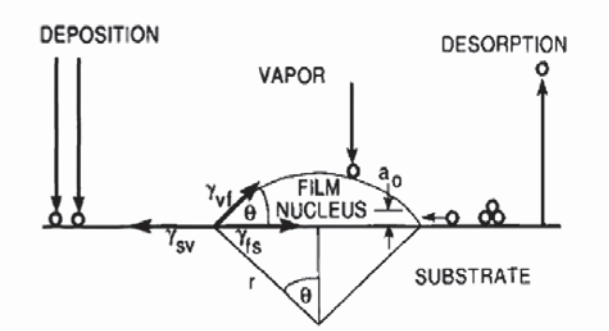

Fig. 2.12: Schematic of basic atomistic process on the substrate surface during vapour deposition [8]

The stable nuclei grow until they make contact, and finally cover the whole substrate surface. This process is driven by the lowering of surface energy as a consequence of grain boundary formation. Therefore, no mass transport between nuclei is necessary, only elastic distortion. Furthermore, the number of islands decreases caused by coalescence and Ostwald-ripening. For this step, diffusion processes through grain boundaries are responsible and tend towards lower energy levels. Within this process, small islands can shrink and finally disappear, in aid of bigger ones. The steps of coarsening resulting from coalescence are shown in Fig. 2.13 [8, 20].

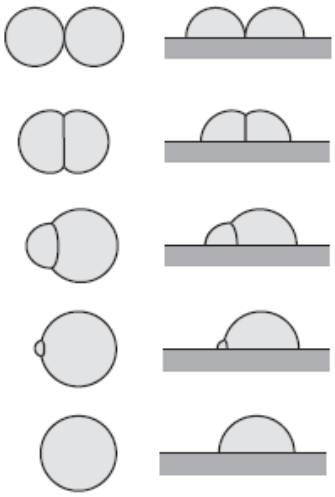

Fig. 2.13: Coarsening resulting from the coalescence of two islands [20]

Three main types of growth modes can be distinguished:

- Island growth (Volmer-Weber)
- Layer growth (Frank-van der Merwe)
- Mixed layer- island growth (Stranski-Krastanov)

Island growth is a three dimensional growth mode, which occurs when the attraction between the adsorbed atoms is higher than that to the substrate surface. Layer growth occurs when the affinity of adsorbed species to the substrate surface is higher than to each other. This leads to epitaxial growth, layer by layer. Mixed layer-island growth arises when layer growth becomes unfavourable [8, 20].

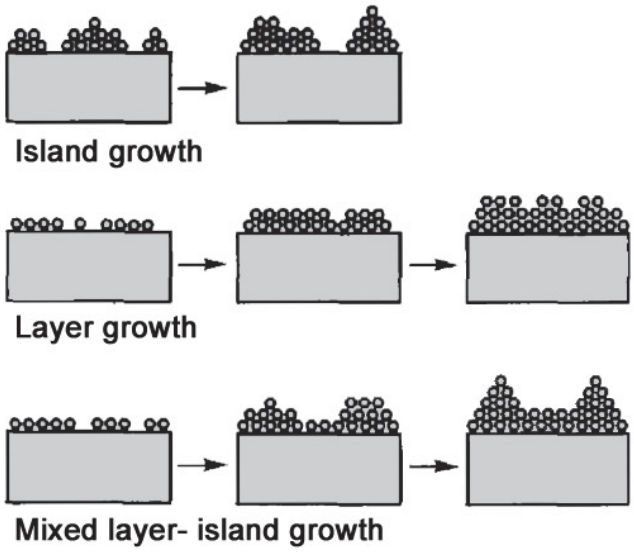

Fig. 2.14: Basic modes of thin film growth [8]

Studies of deposition parameters and film structures lead to the development of structure zone models. The evolution of structure can be correlated with the homologous temperature T_s/T_m where T_s stands for the substrate temperature and T_m for the melting point of the deposited material. A superposition of surface diffusion processes and bulk diffusion processes under consideration of homologous temperature is responsible for structure evolution, shown basically in Fig. 2.15. Zone I and Zone T possess structures produced by continuous nucleation processes and continuous grain growth. The grain size is smaller than the layer thickness. Preferred growth of energetically favourable oriented grains at medium temperatures occurs; the outcome of this is a V-shaped structure of the transition zone, common for high temperature CVD. By enhanced surface diffusion at elevated temperatures, a recrystallised structure (Zone II) with a decrease in porosity and large grains appears [8, 22, 23].

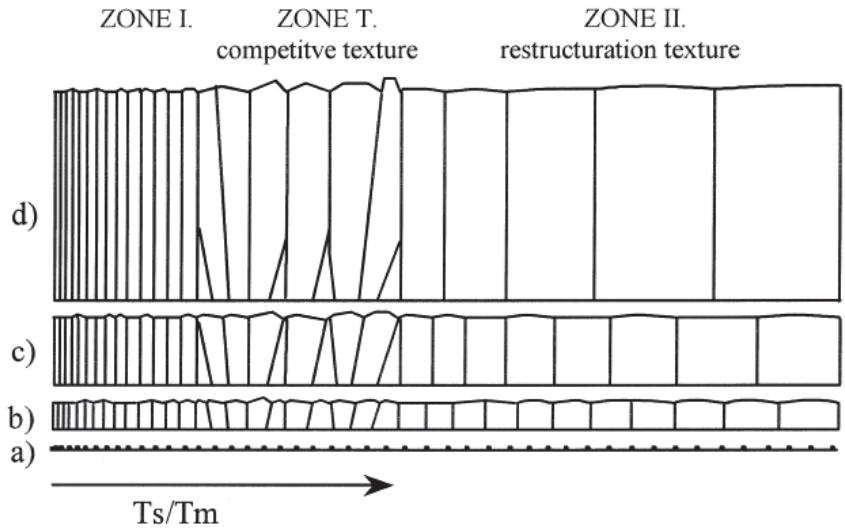

Fig. 2.15: Basic structure zone models at various film thicknesses [23]

The common structures of CVD coatings are shown in Fig. 2.16, where three main types can be distinguished. Type (a) is a columnar structure with dome-like caps, caused by low supersaturation and high surface diffusion. With rising supersaturation type (b) occurs, which is characterised by faceted columnar grains. The fine equiaxed grains of type (c) can be produced using higher supersaturation in combination with lower diffusion rates [7].

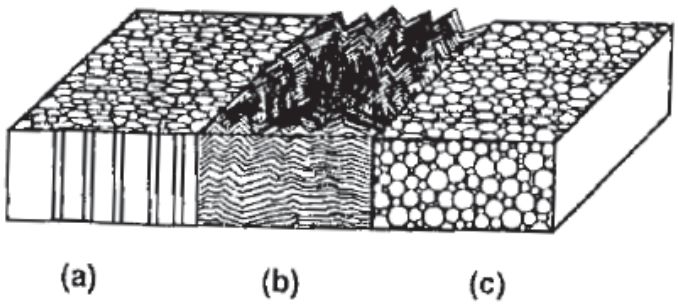

Fig. 2.16: Schematic of structures obtained by CVD: (a) columnar grains with domed tops, (b) faceted columnar grains, (c) equiaxed fine grains [7]

Common homologous substrate temperature are approximately 0.45 < T_s/T_m < 0.55 for the deposition of aluminium oxide via high temperature atmospheric pressure CVD process, as applied for optical thin films and wear resistant hard coatings. Consequently, the formation of V-shaped columnar structures, depending on deposition temperature and surface energy conditions influenced by impurities, is commonly observed (Type 1, Fig. 2.10) [7].

2.2 Aluminium oxide

Al_2O_3 exists in many polymorphs, exhibiting different structures and properties. The equilibrium phase is α-Al_2O_3, named corundum. This structure can be expected in the CVD process, at high temperatures without dopands. The first commercial use of a CVD- Al_2O_3 coated tool was documented during the 1970's. In the last few decades, enhanced technologies like addition of H_2S or boron doping allowed also the controlled deposition of metastable polymorphs. In particular, layers of κ-Al_2O_3 and γ-Al_2O_3, but also multilayer coatings [1] composed of these phases were developed. The properties of polymorphs which can be deposited in a controlled way at industrial scale are given in Tab. 2.1. Besides these, many other polymorphs such as δ, θ, σ and χ exist. Which one of the aluminium oxide modifications will be deposited depends on the process parameters like gas composition, pressure and temperature, but also on the catalytic effects of doping elements [24, 25]

Tab. 2.1: Properties of stable and metastable CVD Al_2O_3 polymorphs [1]

	α-Al_2O_3	κ-Al_2O_3	γ-Al_2O_3
Stability	Stable	Metastable	Metastable
Crystal system	Trigonal	Orthorhombic	Cubic
Space group	$D_3^6d = R\bar{3}c$	$Pna2_1$	Fd3m
Lattice parameters (Å)	Hexagonal (h): $a = 4.7587$, $c = 12.9929$, $n = 6$ Rhombohedral (R): $A = 5.12$, $\alpha = 55.17°$, $n = 2$	$a = 4.8351$ $b = 8.3109$ $c = 8.9363$	$a = 7.92$
Al atoms in unit cell	12(h)/4(R)	16	63/3
O atoms in unit cell	18(h)/6(R)	24	32

Data for α-Al_2O_3 cell is given in both hexagonal (h) and rhombohedral (R) systems.

α-Al_2O_3 exhibits a trigonal structure with ABAB stacking, which consists of almost close-packed oxygen ions along the c axis. Six layers of oxygen atoms are included per unit cell and the Al atoms occupy $^2/_3$ of the octahedral interstitial positions in the oxygen sublattice. σ-Al_2O_3 is very similar to the stable modification and differs only through the vacancy arrangement.

The κ-Al_2O_3 structure is a primitive orthorhombic, having an ABAC stacking of almost close-packed oxygen ion layers. Both, octahedral and tetrahedral positions are occupied by oxygen, in a ratio of 1:3. Exhibited advantages compared to the stable α-Al_2O_3 are probably higher hardness and smaller grain size. Also a lower thermal conductivity has been reported by Cahil and Lee [26], under consideration of the transformation behaviour of κ-Al_2O_3, as shown in Fig. 2.17 [1].

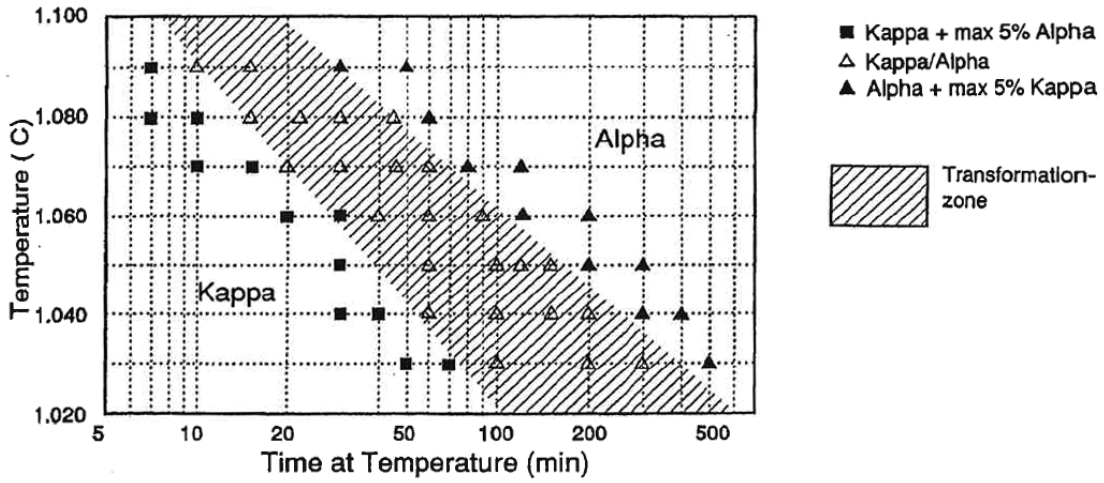

Fig. 2.17: Time-temperature-transition diagram of κ- and α-Al_2O_3 [27]

γ-Al_2O_3 is cubic and based on a face centred cubic ABCABC stacking of oxygen. It can also be described as a defect cubic spinell structure with partly placed vacancies on kation positions. Aluminium ions occupy octahedral as well as tetrahedral positions. The wear properties can be compared with α-Al_2O_3 and κ-Al_2O_3 [1].

Other mentioned aluminium oxide modifications can be divided into the γ-Al_2O_3-group, including η, χ modifications and the δ-Al_2O_3-group covering δ, θ and κ forms. Both groups exhibit contorted spinell structure distinguished by aluminium and oxygen ion location. Metastable phases are synthesised commonly through heat treatment of metastable species based on dehydration and the calcination process. The progress of phase transformation depends on the raw material, as illustrated in Fig. 2.18. These metastable phases differ from other aluminium oxide modifications in stacking sequence or vacancy arrangement. However, they can be stabilised by inserting different ions [28].

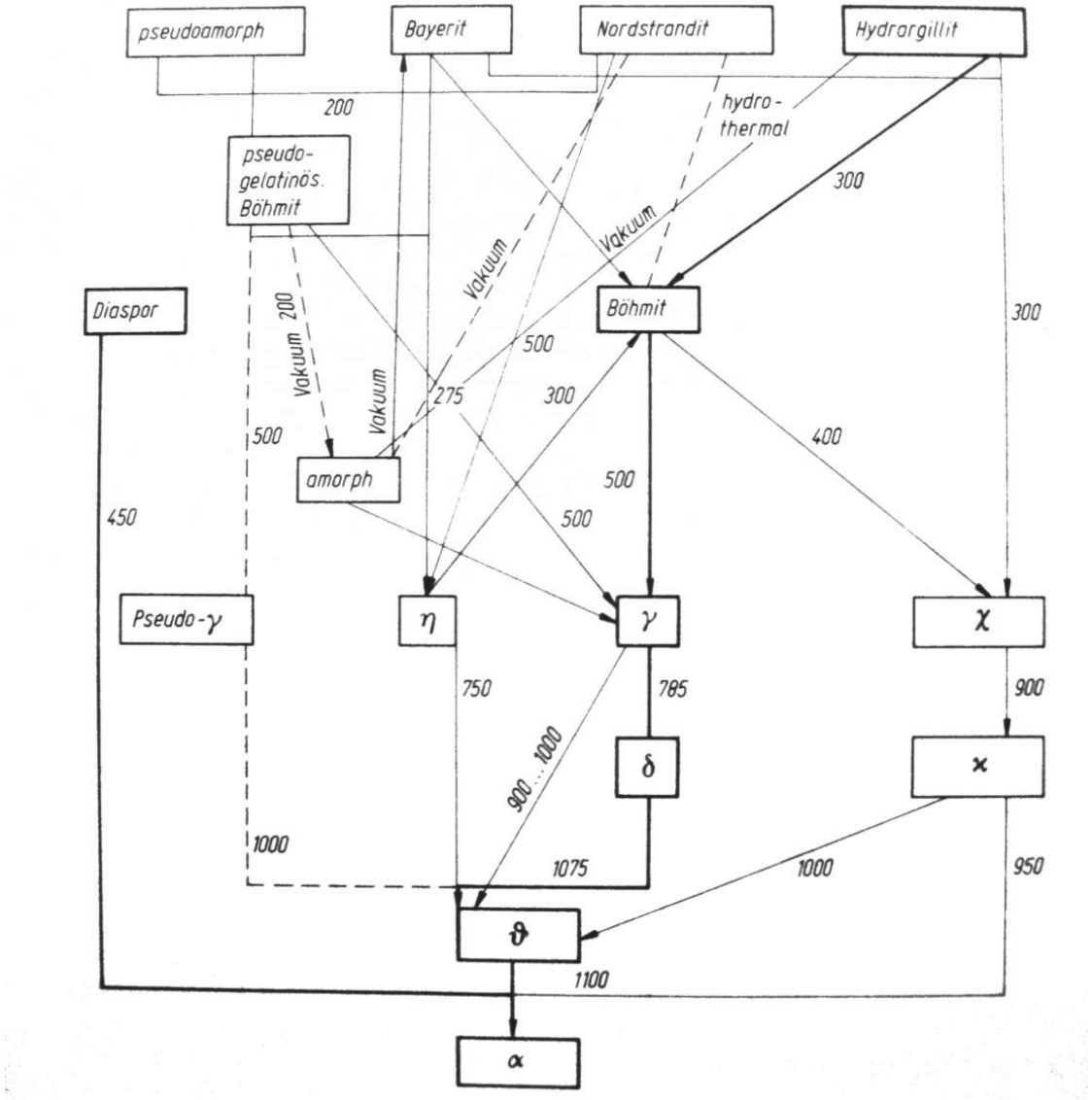

Fig. 2.18: Progress of aluminium oxide phase transformations
out of mineralogical phases [28]

2.3 Doping of aluminium oxide

Barna et al. [23] modified the previously discussed structure zone models and discussed the influence of impurities on structure formation. The so-called real structure zone models at various impurity levels are shown in Fig. 2.19. In this investigation oxygen level was varied as impurity in a metallic aluminium layer. Depending on impurity type, either segregation at surface regions and grain boundaries and/or solution in the grains can occur. Decisive, which mechanisms take place is the reduction of specific grain boundary energy caused by the segregated impurities [29].

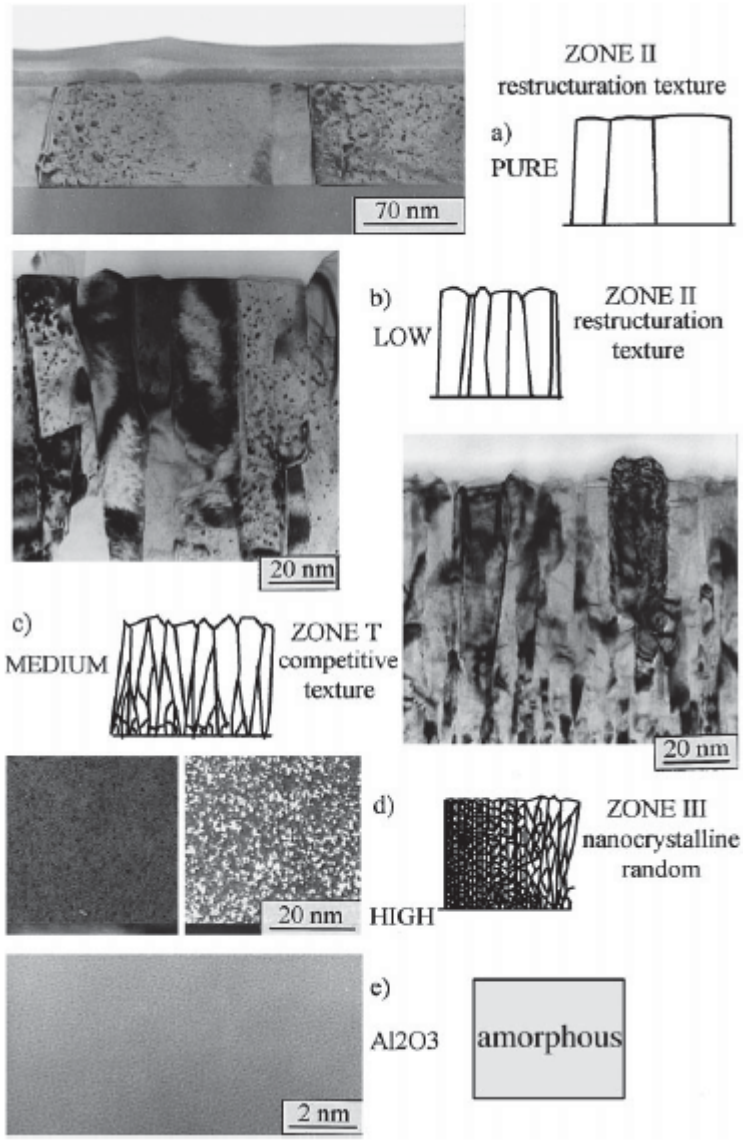

Fig. 2.19: Structural characteristics of Al thin films deposited by thermal evapouration at room temperature at normal high vacuum condition a), at low b), medium c), high d) and very high e) level of oxygen contamination [23]

Active foreign components may have two oppositional effects in thin film growth, they are either promoters, which lead to a significant increase in grain size, or they tend to be inhibitors which cause a decrease in grain size. A composite structure arises, which can be split into in three main categories, depending on the additive level, as shown in Fig. 2.20. In case a), a low concentration of a second element acting as pinning sites is illustrated. By increasing the amount of the second element, grains of predominant species will be muffled (case b) and finally the second species is available in excess (case c) [23, 30].

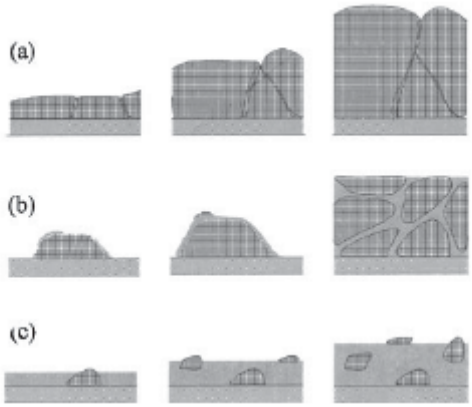

Fig. 2.20: Schematic figures of composite structure for different film thickness in the case of (a) low and (b) high concentration of the minority additive component, as well as in the case of additives giving the majority component (c) [30]

At low dopant concentration, two cases of layer growth can be distinguished. Condensation of the minority species on the growth surface of the majority component leads to the formation of a pure second phase or a compound solid phase. Grain boundary migration is inhibited as well as grain growth if the phases act as pinning sites for the grain boundary. Another consequence of this segregation at low dopant concentrations is an increase of thermal stability, which can be related to the lowered grain boundary energy [30]. The structure and contamination of grain boundaries also influences the distribution and concentration of adatoms which also determines the surface topography. Hills along grain boundaries or coarse grooves, decorated by small particles are the two different types of crystal growth documented by Barna et al. [31], illustrated in Fig. 2.21.

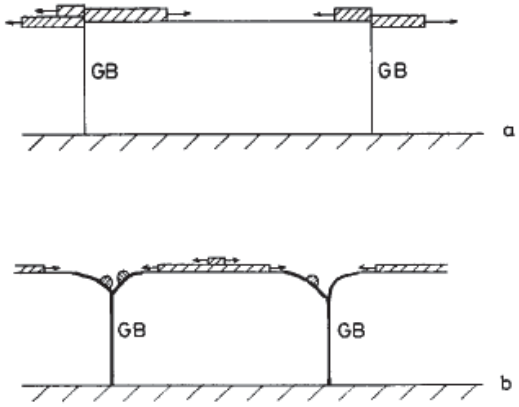

Fig. 2.21: Expected monolayer growth of crystals in continuous Al films. (a) NaCl substrate, low oxygen contamination. Pure grain boundaries (GBs) are active in the monolayer nucleation. (b) Glass substrate, high oxygen contamination. GBs contaminated by an oxide phase are inactive in the monolayer nucleation. The growth steps proceed towards the GBs and accumulate oxygen at GBs. [31]

2.3.1 Supposable elements

For the experiments, performed within this thesis, the thirteen elements given in Tab. 2.2 were taken into account. They can be categorized into three main groups:

- Melting point of the respective chloride lower than metallic aluminium
- Melting point of the respective chloride higher than metallic aluminium
- Gaseous precursor species

To reach an adequate number of experiments within this thesis, four elements were chosen, considering the availability of the precursor, handling, safety regulations and the proposed influence on aluminium oxide. The last block containing phosphorus and sulphur was excluded from the experiments, phosphorus because of safety reasons, especially due to the high reactivity. The influence of sulphur as an additive in form of H_2S is state of the art and well documented in literature [1, 24, 32].

Tab. 2.2: Supposable elements, separated into groups depending on chloride melting point and precursor state. green: melting point of chloride lower than 660 °C; orange: melting point of chloride higher 660 °C; yellow: gaseous precursor

	$T_{m,\ element}$ °C	Chloride	$T_{m,\ chloride}$ °C	$T_{b,\ chloride}$ °C	Oxide	$T_{m,\ oxide}$ °C
Ge	938	$GeCl_4$	-50	87	GeO_2	1116
Nb	2477	$NbCl_5$	205	247, 254	NbO	1937
					NbO_2	1900
					Nb_2O_5	1460, 1512
Ta	3017	$TaCl_5$	210	233	Ta_2O_5	1880
Bi	271	$BiCl_3$	234	441	Bi_2O_3	817
In	157	InCl	211, 216	608	In_2O_3	1913
Sn	232	$SnCl_2$	247	623	SnO	1080
		$SnCl_4$	-33	114	SnO_2	1927, 1630
Al	660	$AlCl_3$	193	180	Al_2O_3	2054
Y	1526	YCl_3	710	1510	Y_2O_3	2690
Cr	1857	$CrCl_2$	815	1120	Cr_2O_3	2450, 2330
Sr	777	$SrCl_2$	874	1250	SrO	2530, 2665
Mg	650	$MgCl_2$	714	1412	MgO	2830
					MgO_2	100
Ca	842	$CaCl_2$	782, 775	> 1600	CaO	2900
P		PCl_3	-112	76	P_4O_6	24
		PCl_5	167	160	P_4O_{10}	422, 562
		P_2Cl_4	-28	180		
S		SCl_2	-122	60		
		ClSSCl	-76	138		
		S_3Cl_2	-46	31		

From the first block niobium and tin, and from the second block chromium and strontium were selected. Some physical properties of these supposed species are summarized in Tab. 2.3. These elements fulfil the afore mentioned criteria, and will be discussed below in detail.

Tab. 2.3: Some physical properties of supposed species [33]

Species	Lattice	Parameter (a/b/c)	Space group
α-Al_2O_3	Rhombohedral	a=4.758/c=12.991	R-3c (167)
α'-Al_2O_3	Monoclinic	9.566/5.124/9.156 (β=91.76)	P2 (3)
γ-Al_2O_3	Face-centred cubic	a=7.900	Fd3m (227)
δ-Al_2O_3	Tetragonal	a=7.943/c=23.500	P43212 (96)
δ-Al_2O_3	Tetragonal	a=5.599/c=23.657	P-4m2 (115)
κ-Al_2O_3	Orthorhombic	4.839/8.318/8.944	Pna21 (33)
κ'-Al_2O_3	Hexagonal	a=5.544/c=9.024	P63mc (186)
σ-Al_2O_3	Face-centred cubic	a=7.945	Fd-3m (227)
θ-Al_2O_3	Base-centred monoclinic	5.620/2.906/11.790 (β=103.79)	A2/m (12)
χ-Al_2O_3	Hexagonal	a=5.57/c=8.640	P (0)
χ-Al_2O_3	Cubic	a=7.950	P (0)
Cr_2O_3	Rhombohedral	a=4.962/c=13.597	R-3c (167)
NbO	Cubic	a=4.210	Pm-3m (221)
NbO_2	Body-centred tetragonal	a=13.710/c=5.985	I41/a (88)
Nb_2O_5	n. A.		(0)
$AlNbO_4$	Base-centred monolithic	12.157/3.736/6.490 (β=107.62)	C2/m (12)
SnO_2	Tetragonal	a=4.703/c=3.173	P42/mnm (136)
Sn_3O_4	Triclinic	5.88/8.20/4.86 (α=93.35/β=91/γ=93)	P-1 (2)
SrO	Face-centred cubic	a=5.160	Fm-3m (225)
SrO_2	Body-centred tetragonal	a=3.569/c=6.590	I/4mmm (139)
$SrAl_2O_4$	Monoclinic	8.447/8.816/5.163 (β=93.42)	P21 (4)

2.3.2 Chromium oxide

Cr_2O_3 is the only appearing intermediate species in the chromium-oxygen system in thermodynamic equilibrium as can be seen in Fig. 2.22. The species can be found up to 60 at.-% oxygen and up to 1660 °C.

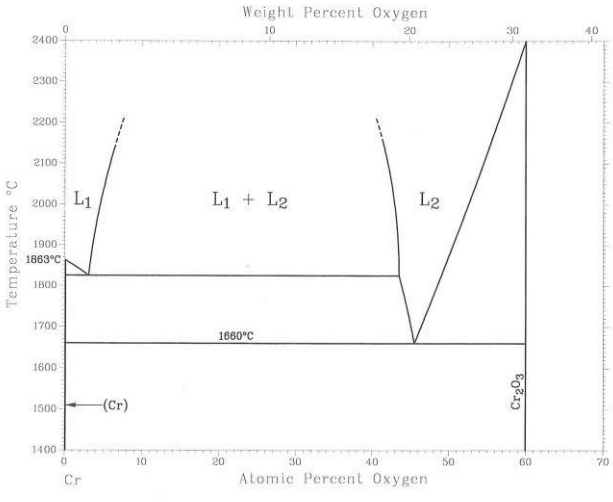

Fig. 2.22: Chromium oxygen system [34]

The binary phase diagram of the Al_2O_3-Cr_2O_3 system, illustrated in Fig. 2.23 shows an entire solubility over the whole composition range. That can be explained by the small lattice mismatch of the components, which mainly causes elastic strains.

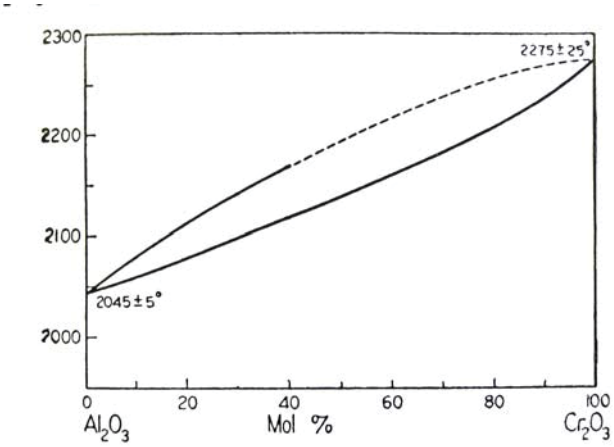

Fig. 2.23: Al_2O_3-Cr_2O_3 phase diagram [35]

Colombier et al. [36] documented a grain refining effect of $CrCl_2$, by promoting secondary nucleation. The layer morphology showed a very fine grain size over the whole surface of the specimen. Danzinger et al. [37] found a negative influence on growth rate and also a loss of epitaxial growth and cauliflower-like, fine structures.

2.3.3 Niobium oxide

Three intermediate species NbO, NbO_2 and Nb_2O_5 can be seen in Fig. 2.24. NbO occurs up to 66 at.-% oxygen and melts incongruently at 1945 °C, which indicates the high thermal stability of niobium oxide species.

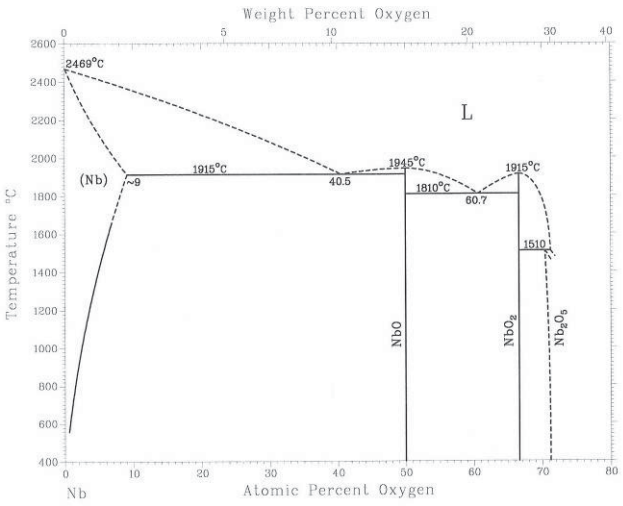

Fig. 2.24: Niobium oxygen system [34]

Considering the binary phase diagram of Al_2O_3-Nb_2O_5 displayed in Fig. 2.25, two main intermediate species can be seen. The orthorhombic $AlNbO_4$ phase is stable over a wide range of compositions and forms together with Al_2O_3 a two phase field at low niobium oxide content. A positive influence of this structure as a bonding interlayer between TiC and Al_2O_3 was documented by Lee et al. [35], which can be explained by the relatively small lattice mismatch similar to $AlTaO_4$. Niobium containing layers produced via the CVD process find application as optical layers and sensors, but most of these processes deal with metal organic precursors [7].

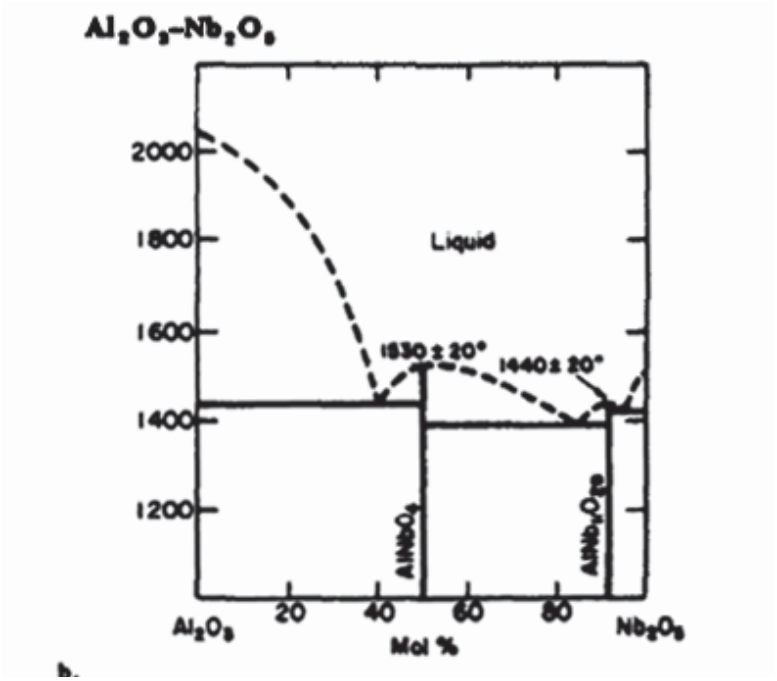

Fig. 2.25: Al_2O_3-Nb_2O_5 phase diagram [35]

2.3.4 Tin oxide

The binary phase diagram of Sn-O is shown in Fig. 2.26 and exhibits two intermediate phases, Sn_3O_4 and SnO_2. The first one possesses two phase transformations in the area of interest, one at 232 °C and the second one at 1040 °C.

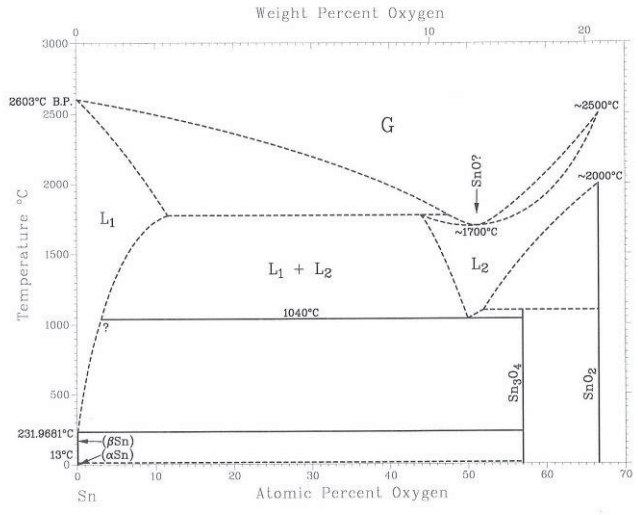

Fig. 2.26: Tin oxygen system [34]

Tin oxide was taken into consideration because of its assumed lubricating properties for wear applications and good corrosion resistance against lead-glass melts [40, 41]. In literature, various deposition temperatures between 450 °C and 1300 °C are documented as well as the simple experimental set-up [38].

2.3.5 Strontium oxide

Despite extensive search, no information about the Sr-O system could be found.

Douy et al. [39] mentioned that many uncertainties still remain in the system of $SrO\text{-}Al_2O_3$, especially concerning the melting points and behaviours of many components. $SrO{\cdot}Al_2O_3$ is known as a stable phase in the aluminium rich area of the system, which can be seen in Fig. 2.27. Investigations of the crystallisation behaviour in this system showed a stabilizing effect of $\gamma\text{-}Al_2O_3$, caused by the relatively big Sr^{2+} ions. The crystallisation point of monoclinic $SrO{\cdot}Al_2O_3$ out of the amorphous phase was ascertained at 917 °C. A transformation of the monoclinic low temperature configuration into the hexagonal structure at about 650 °C is known. The hexagonal polymorph can be easily stabilized at room temperature using cations like calcium, silicon or aluminium. At temperatures above 1100 °C, the compound $4\ SrO{\cdot}7Al_2O_3$ is formed by an exothermic reaction. $SrO{\cdot}2Al_2O_3$ species could only be

obtained by the solidification of the melt. This species is also known as a stable compound, however it is characterised by a slow kinetics of formation [39].

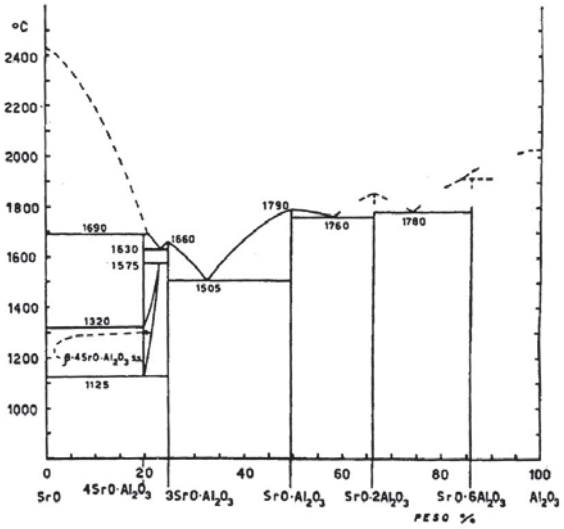

Fig. 2.27: $SrO\text{-}Al_2O_3$ phase diagram, after Massazza [42]

Yoshida et al. [43] documented the influence of dopants on the grain boundary diffusivity of Al_2O_3. A lowering effect has been confirmed, caused by strontium oxide as can be seen in Fig. 2.28. This decreased mobility of atoms could interfere effects like Ostwald ripening and coalescence, which were mentioned above. That may have a positive influence on grain size in the CVD process, on the condition that sufficient strontium species can be built into the layer.

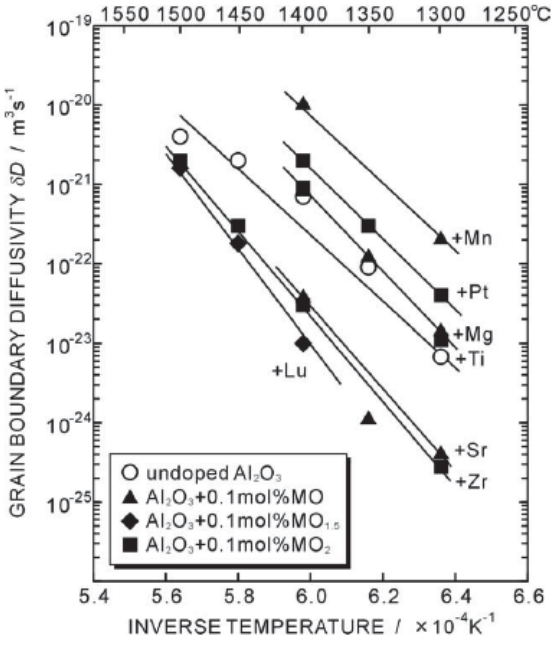

Fig. 2.28: An Arrhenius plot of the grain boundary diffusivity against inverse temperature in undoped Al_2O_3 and 0.1 mol-% cation-doped Al_2O_3 [43]

3 Experimental

3.1 CVD equipment

3.1.1 Substrate and precursor materials

In this thesis, two different substrate materials were coated. The major parts of experiments were performed on cemented carbide cutting inserts of Ceratizit grade S40T. These substrates display SNUN geometry according to ISO 1832. The polished inserts were precoated with a TiC/TiCN/TiN layer. For further experiments, ground molybdenum substrates of the same dimensions were used.

Aluminium chloride is generated by passing hydrochloride acid gas over aluminium granules, at temperatures above the sublimation temperature of aluminium chloride. Additional elements were inserted in the form of aluminium alloys, metals or salts. Species used are listed in Tab. 3.1.

Tab. 3.1: Precursor materials

Element	Purity	Shape
Aluminium	Al (> 99.9 %)	granules
Chromium	Al-Cr alloy (20 wt.-% Cr, PM)	cube 5x5x5 mm
Niobium	Niobium (> 99%)	cuboid 5x5x8 mm
Tin	Aluminium tin alloy (20 wt.-% Sn)	granules
	$SnCl_2$ (> 97 %)	salt
Strontium	$SrCl_2$ (> 99.9 %)	salt

3.1.2 Experimental set-up

The experiments were carried out in a horizontal hot wall reactor (cf. Fig. 3.1) with three separate controllable heating zones, each 200 mm long. Molybdenum heaters and an argon flushed shell allow heating rates of around 15 $Kmin^{-1}$. The inner diameter of the working tube was 51 mm and its total length was 1200 mm. Alumina was used as the refractory material and also for the specimen carriers. Three of these carriers, tube sections of 41 mm inner diameter and 80 mm length, were arranged without gaps in the third heating zone and parts of second heating zone. Three specimens were placed on each of them, i.e. nine samples numbered from 2 to 10 were coated in each run. Position 1 was not used in these experiments

because the deposition temperature was too low, as investigated in a preliminary study. A Pt10 thermocouple was located above the specimen in position 4 to determine the substrate temperature as good as possible.

Gas flows were controlled by flow meters according to the rotameter principle [44]. The gas purities used were 4.6 and 5.0. The exhaust gas was routed through a dry trap to collect condensing chlorides and prevent plugging of the facility.

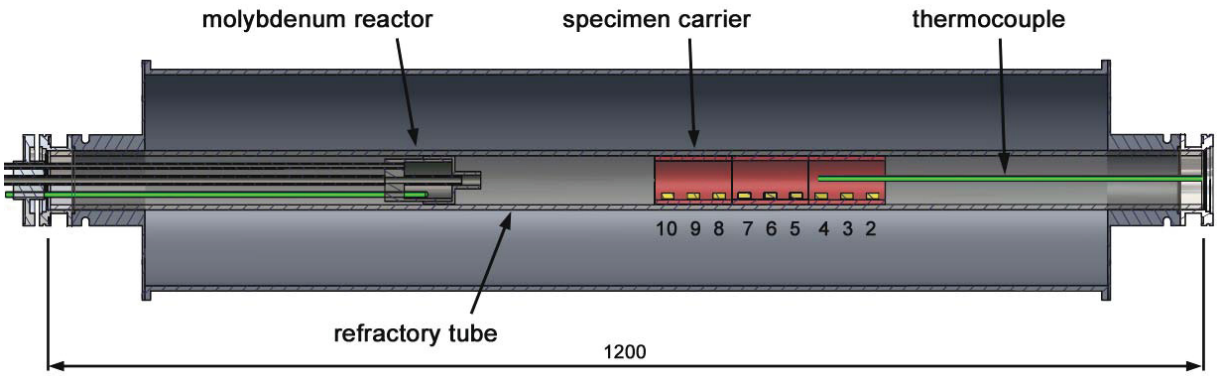

Fig. 3.1: Experimental setup and specimen position

3.1.2.1 Single reactor alignment

For the volatilisation of the precursor, a molybdenum reactor, as illustrated in Fig. 3.2, was placed within the first heating zone. Hydrochloride acid gas and argon as a carrier stream were fed through the eccentric tube which ended in the reaction chamber, where aluminium granules, aluminium alloys or salts were placed.

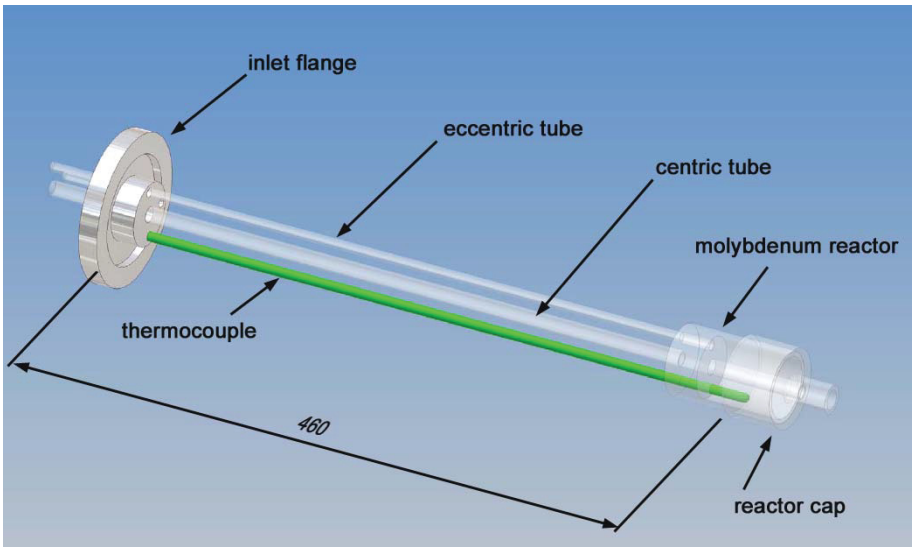

Fig. 3.2: Molybdenum reactor

Oxygen containing species such as carbon dioxide and carbon monoxide were mixed with nitrogen and hydrogen and inserted through the centric tube, which ended near the reactor cap. There the process gases were mixed and flow towards the deposition zone. To prevent backflow, argon was also introduced near the front flange. The temperature inside the reactor was measured by a NiCr/Ni thermocouple placed in the reaction chamber. The whole arrangement can be seen in Fig. 3.3.

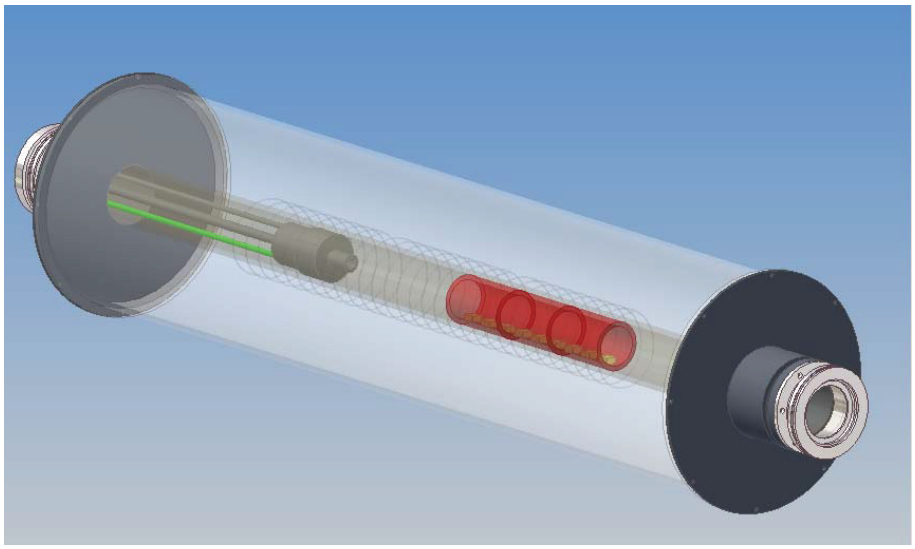

Fig. 3.3: Single reactor alignment

3.1.2.2 Double reactor alignment

For the realization of different volatilisation temperatures, a second reactor, shown in Fig. 3.4, was added to the setup. The second reaction chamber made of corrosion resistant Cr-Ni-steel was heated by a resistance heating element, surrounding the reactor. This vertical reactor was positioned next to the inlet flange of the tube furnace. The connecting feed line was kept as short as possible and heated up to approximately 220 °C, in order to prevent the condensation of the chlorides. The precursor was placed on a steel grid below the outlet vent. The process temperature was controlled by a thermocouple located nearby. Carrier or chloride gas was fed in from underneath.

Two input arrangements of the double reactor alignment must be distinguished. For experiments with a low volatile chloride as precursor ($SnCl_2$), a quartz crucible containing chloride melt was placed in the steel reactor and a gaseous chloride species was transported with an argon carrier gas which flowed through a 3 mm pipe placed in the central pipe. The vapour pressure over the liquid chloride melt was exploited for the transportation of the doping agent. The remaining setup was similar to that of the pure aluminium oxide deposition.

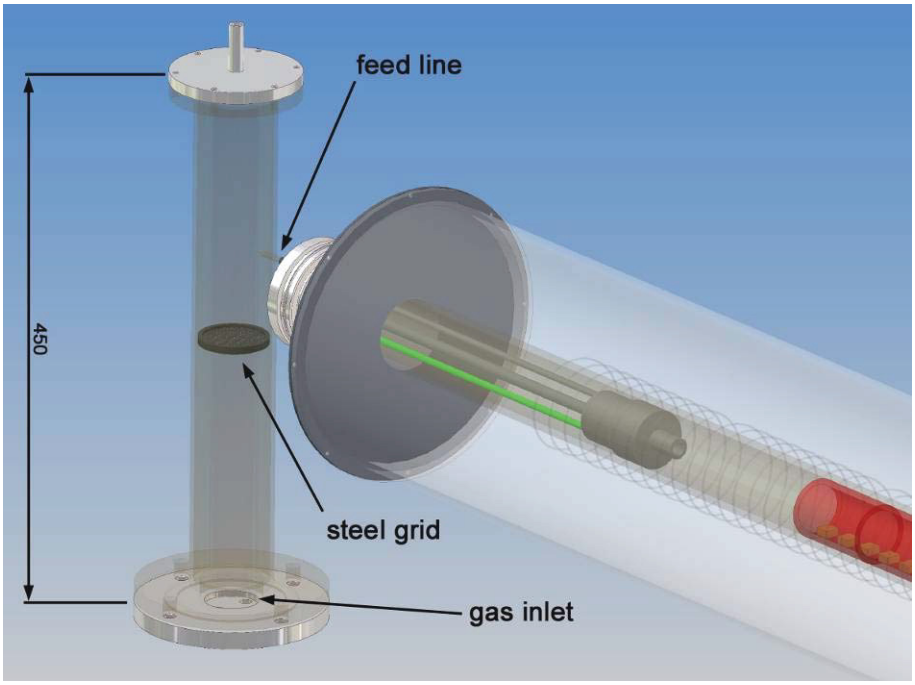

Fig. 3.4: Double reactor alignment

For chlorides with melting points higher than that of aluminium ($SrCl_2$), the aluminium granules were placed in a steel reactor and $AlCl_3$ was generated by passing HCl. As a feed line, the eccentric tube, which ends in the reaction chamber of the molybdenum reactor, was used. At this site, the crucible formed of molybdenum foil containing the chloride melt, was placed. This arrangement, applied in principle by Sipp et al. [15] for YCl_3, enables precursor temperatures up to the deposition temperature.

3.1.3 Temperature gradient

Temperature profiles were measured simultaneously with thermocouples and process temperature control rings with nitrogen gas flow, simulating deposition conditions. The temperature value of each specimen position was calculated through the approximation of measurements with a polynomial regression of fourth order. A profile for the aluminium oxide deposition, in the region where substrates were positioned, is shown in Fig. 3.5.

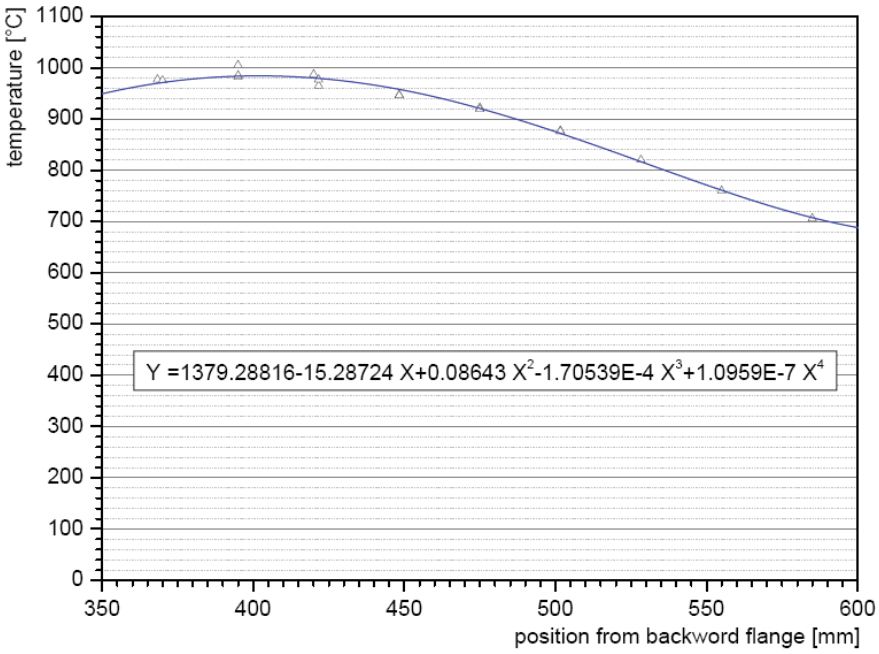

Fig. 3.5: Temperature profile at specimen positions

3.1.4 Test procedure

First, precursors and samples were weighed and attached to the reactor using specimen carriers, which were placed on defined positions. Towards assembling the flanges, the gas supply and the exhaust gas system were connected. Initially, the working tube was evacuated and filled up with argon in order to displace the remaining oxygen. Following, the three zones were heated to the desired temperature with 15 $Kmin^{-1}$ under H_2/Ar atmosphere. After obtaining the target values, a dwell for temperature compensation was adhered.

The deposition process started with inserting hydrochloride acid gas and lasted 90 or 180 minutes, respectively. CO and/or CO_2 containing nitrogen gas mixture was inserted after five minutes and flow rates enhanced stepwise to the target values within five further minutes.

At the end of the deposition process, the HCl and gas mixture feed lines were closed and the facility cooled in Ar/H_2 atmosphere to room temperature. After disassembling, the appearance of specimens, reactor and working tube were documented and the weight changes determined. Following surface and fracture cross-section pictures were taken from selected specimen positions as well as glow discharge optical emission spectroscopy (GDOES) and X-ray diffraction (XRD) measurements were performed. More information about the analysis performed will be given in section 3.2.

3.1.5 Gas composition

The reference gas composition used for the experiments was a downscaling of the production ambient documented in [45]. The composition used enables growth rates of 1 µm/h at investigated temperatures. Compared to other authors, listed in Tab. 3.2, the total gas flow is four times higher. Under consideration of different operating pressures this should lead to comparable results. Schierling et al. [49] documented a very low dependency on total gas flow rates manifested by a surface reaction limited process.

Tab. 3.2: Comparable gas compositions, documented in literature

Author	Temperature / Pressure	Gas Composition
Colmet, 1982 [46]	1050 °C, 18 l/h total gas flow	0.8 % $AlCl_3$ / 49.6 % H_2 / 49.6 % CO_2
Colombier, 1986 [36]	1050 °C, 65 mbar 25 l/h total gas flow	1 mol-% AlX_3 / 3.5 mol-% CO_2 / 95 mol-% H_2
Danzinger, Lux, Haubner, 1990 [37]	1030 °C, 65 mbar 25.5 l/h total gas flow	1 mol-% $AlCl_3$ / 3.5 mol-% CO_2 / 95 mol-% H_2
Halvarsson, 1993 [47]	50 mbar	5-7 % CO_2 / 1 % HCl / 2-3 % $AlCl_3$ / Balance H_2
Fredricsson, 1995 [48]	1000 °C, 67 mbar 24 l/h total gas flow	2.7 % $AlCl_3$ / 90 % H_2 / 6.8 % CO_2
Müller, Neuschütz, 2003 [19]	900-1200 °C, 100 mbar 20 l/h total gas flow	0.25-3.5 % $AlCl_3$ / 0.1-24 % HCl / 1-20 % CO_2 / 1-90 % H_2 / Ar balance
used composition	850 – 1050 °C, ~1013 mbar 50-110 l/h total gas flow	1.5 % $AlCl_3$ / 4.8 % CO_2 / 2.7 % CO / 9 % H_2 / 30 % Ar / 50 % N_2

All investigations listed were performed using a horizontal hot wall reactor at temperatures between 900 and 1200 °C. The documented experiments mentioned above were performed with an $AlCl_3$:CO_2 ratio between 1:2 and 1:3.5. For the gas balance, different gases like hydrogen argon or nitrogen were used by the authors listed. Another difference compared to the gas composition within this thesis is the HCl gas in the feed gas composition. This can have inhibiting an influence for bigger amounts on the deposition as stated earlier.

3.2 Analytics

3.2.1 Gravimetric analysis

Mass changes of specimens and precursors were acquired by a Mettler AT Delta Range 261 precision balance. The accuracy of this instrument is ± 0.1 mg.

3.2.2 Scanning electron microscopy

Surface images were taken on a JEOL JSM-6300 scanning electron microscope (SEM) using a magnification of 500x. Applied acceleration voltages were 15 and 25 kV in combination with a 15 mm working distance. Fracture cross-sections of the deposited layers were recorded by a Zeiss evo50 microscope at the same magnification. The acceleration voltage used was 20 kV and the working distance was between 8 and 10 mm.

3.2.3 Glow discharge optical emission spectroscopy

The content of additional elements in the deposited layer was quantified by glow discharge optical emission spectroscopy (GDOES) via a Jobin-Yvon Horiba JY10000RF facility. This enables the possibility of bulk analysis and depth profiles of elements. The principal setup is illustrated in Fig. 3.6.

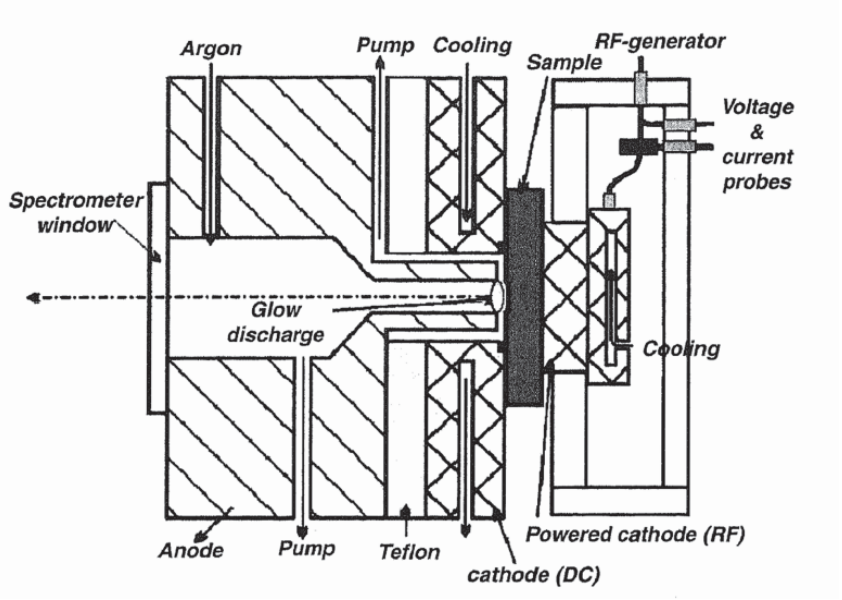

Fig. 3.6: Principle of glow discharge optical emission spectroscopy [50]

The working principle of GDOES is based on unique optical radiation for each element. Therefore, a glow discharge is ignited through a radio frequency applied between the copper anode and the sample. This causes plasma inside the evacuated argon flushed chamber, which ionises the noble gas, and also accelerates the ions towards the sample. The sputtered atoms from the sample were stimulated by plasma, which causes the emission of unique radiation pattern, characteristic for each element. The intensity of the photons is detected using an optical emission spectrometer coupled with a software analysis package. By comparing with reference samples, it is possible to generate quantitative analysis of low concentrations with high accuracy, typically 0.4 % for main elements [50, 51].

3.2.4 X-ray diffraction analysis

X-ray diffraction (XRD) measurements were carried out on a Panalytical X'Pert Pro diffractometer using copper K_α-radiation and a flat graphite monochromator. This analyser quantifies the intensity of reflected X-rays which fulfil Bragg's law, corresponding to Eq. 3.1 where λ symbolizes the wavelength, n the order of diffraction, d_{hkl} the interplanar spacing of the lattice indexed by the Miller indices *h, k, l,* and θ equals the diffraction angle.

$$n\lambda = 2d_{hkl}\sin\theta \qquad 3.1$$

From the diffraction angle and the intensity, properties like lattice parameters, phase composition, textures and lattice distortions could be derived. A pattern of TiCN precoated cemented carbide is shown as an example in Fig. 3.7 [8, 52].

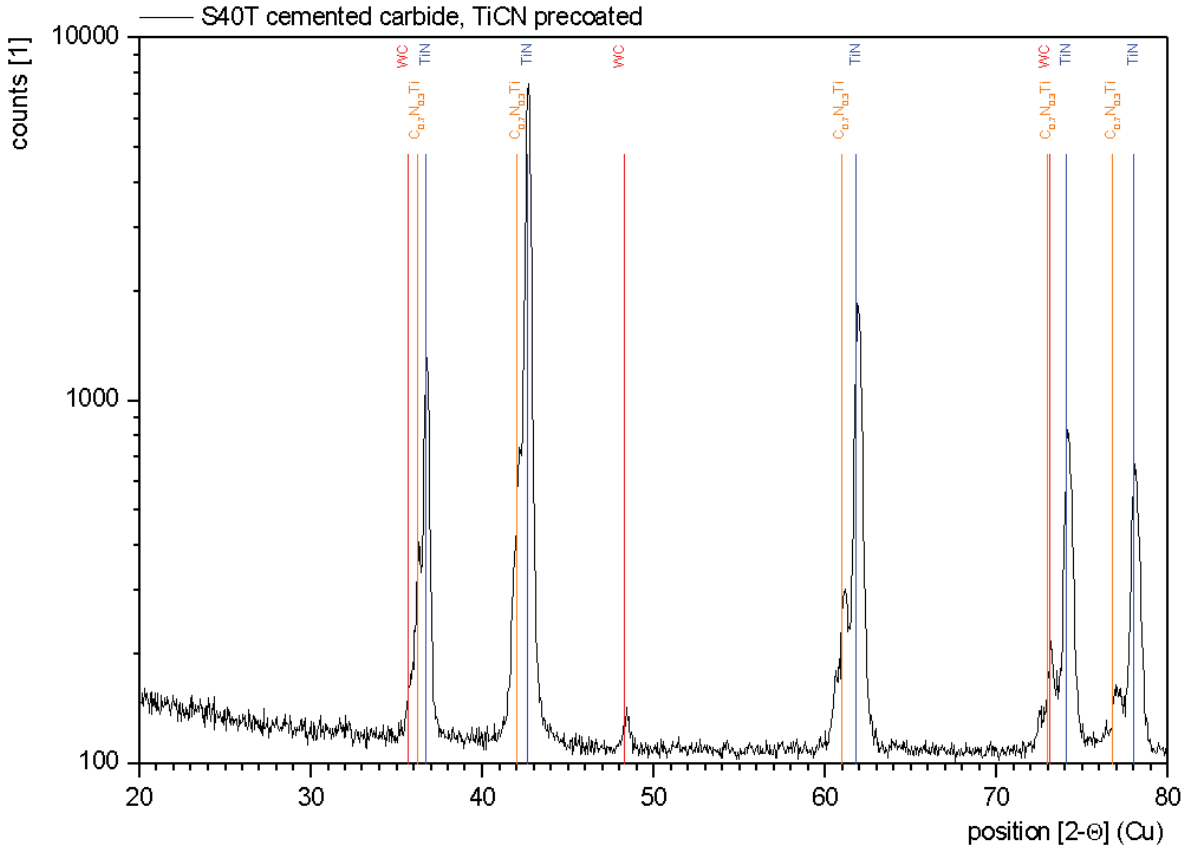

Fig. 3.7: XRD pattern of TiCN precoated cemented carbide

4 Results

The experiments performed within this thesis and the selected parameters as well as their variation are listed in Tab. 4.1. A more detailed overview, including mass change data is given in the appendix.

Tab. 4.1: Overview of experiments and deposition parameters, performed for selected oxide systems. Deposition runs using same doping elements are highlighted by same colour.

Dep. No.	Name	Target temp. [°C]			Duration [min]	varried parameter	Gasflow [l/h]									Alignment
		Z1	Z2	Z3			Total	HCl	N_2	CO_2	CO	H_2	H_2	Ar_{RE}	Ar_2	
I	I/Al	470	660	1050	170		109.0	4.5	60.0	4.8		3.7	6.0	15.0	15.0	single Reactor
II	II/Al	470	660	1050	170	without CO	112.1	4.5	60.0	4.8	-	5.0	7.8	15.0	15.0	
III	III/Al	470	660	1050	170		100.5	4.5	49.8	4.8	2.7	2.7	6.0	15.0	15.0	
IV	IV/AlSn	470	660	1050	170		100.5	4.5	49.8	4.8	2.7	2.7	6.0	15.0	15.0	
V	V/AlSn	470	660	1000	170	temperature	100.5	4.5	49.8	4.8	2.7	2.7	6.0	15.0	15.0	
VI	VI/AlSn	470	660	1050	170	+30%H2	102.5	4.5	49.8	4.8	2.7	2.7	8.0	15.0	15.0	
VII	VII/AlNb	470	660	1050	170		100.5	4.5	49.8	4.8	2.7	2.7	6.0	15.0	15.0	
VIII	VIII/AlNb	470	660	1050	170	Ar distribution	101.0	4.5	49.8	4.8	2.7	2.7	6.0	4.5	26.0	
IX	IX/AlSr	640	820	1035	170		100.5	4.5	49.8	4.8	2.7	2.7	6.0	15.0	15.0	
X	X/AlCr	640	820	1035	170		100.5	4.5	49.8	4.8	2.7	2.7	6.0	15.0	15.0	
XI	XI/AlCr	640	820	1035	170	-30 %N2 mix	80.5	4.5	33.2	3.2	1.8	1.8	6.0	15.0	15.0	
XII	XII/AlCr	640	820	1035	170	+100%CO2	105.3	4.5	49.8	9.6	2.7	2.7	6.0	15.0	15.0	
XIII	XIII/AlCr	640	820	1035	170	+140%CO2	107.5	4.5	49.8	11.8	2.7	2.7	6.0	15.0	15.0	
XIV	XIV/AlCr(Mo)	640	820	1035	170	-50% gas	52.4	2.0	24.9	4.8	1.4	1.4	3.0	7.5	7.5	
XV	XV/AlSn(Mo)	470	690	1050	170	substrate/temperature	105.5	4.5	49.8	9.8	2.7	2.7	6.0	15.0	15.0	double Reactor
XVI	XVI/AlSr	960	980	1015	65	temperature/65'	100.5	4.5	49.8	4.8	2.7	2.7	6.0	15.0	15.0	
XVII	XVII/AlCr	640	820	1035	170	without CO	98.0	4.5	50.0	4.8	-	2.7	6.0	15.0	15.0	
XVIII	XVIII/AlSr	960	980	1015	170		100.5	4.5	49.8	4.8	2.7	2.7	6.0	15.0	15.0	single Reactor
XIX	XIX/AlSr	960	980	1015	80	+100%CO2/80'	105.3	4.5	49.8	9.6	2.7	2.7	6.0	15.0	15.0	double Reactor
XX	XX/AlSr	960	980	1015	80	+100%CO2/80'	102.8	4.5	50.0	9.6	-	2.7	6.0	15.0	15.0	
XXI	XXI/AlSn(Mo)	300	500	700	170	substrate/temperature	100.5	4.5	49.8	4.8	2.7	2.7	6.0	15.0	15.0	
XXII	XXII/AlSn(Mo)	272	501	850	170	substrate/temperature	100.5	4.5	49.8	4.8	2.7	2.7	6.0	15.0	15.0	

In order to allow a fast identification of experiments and samples, the following nomenclature was used. Each deposition is numbered in Roman numbers, followed by an abbreviation of the oxide system and target temperature of heating zone 1 and zone 3. It should be taken into consideration that the substrate temperatures are approximately 50 °C lower than the target temperatures of the controllers. The differences in gas composition are mentioned for each experiment, based on the reference gas composition of deposition III. Detailed information about gas compositions and temperatures are given in the appendix. Each specimen is numbered by a combination of deposition run in Roman numbers and specimen position in Arabic numbers. If the deposition is applied on molybdenum substrates, a remark in round brackets is added after the oxide system abbreviation. For these runs, squares are used as data point symbol in all diagrams within this thesis instead of rhombi. Specimen number 10 is the first and specimen number 2 the last one in gas flow direction (cf. Fig. 3.1). Position 1 was not used in these experiments because preliminary studies showed that the deposition temperature was too low.

4.1 Single reactor alignment

4.1.1 Aluminium oxide

The first three experiments I, II and III, should clarify the repeatability of depositions from a preliminary study. Deposition III was set as reference for doping. Furthermore the influence of 4.5 % CO in the feed gas should be investigated. Three experiments with different gas composition and similar temperature gradient were performed. Results from experiment I were not utilizable by reason of a broken refractory tube. Neither by GDOES measurements, nor SEM images could clarify the influence of CO. Small differences between same specimen position of experiment II and III could only be asserted by XRD measurements.

The addition of CO leads to more uniform mass change over the whole temperature gradient within one experiment. Aluminium oxide was deposited in a temperature range from 830 °C to 1000 °C.

4.1.1.1 Gravimetric analysis

The mass change of experiments II and III are illustrated in Fig. 4.1. It can be seen that the mass change of depositions II and III show a clear dependency on substrate temperature. Specimens III_4 and III_5, which are exposed to highest temperatures, show also the highest mass changes in experiment III. The slightly raised deposition rate in experiment II can be explained by the slightly higher H_2 content.

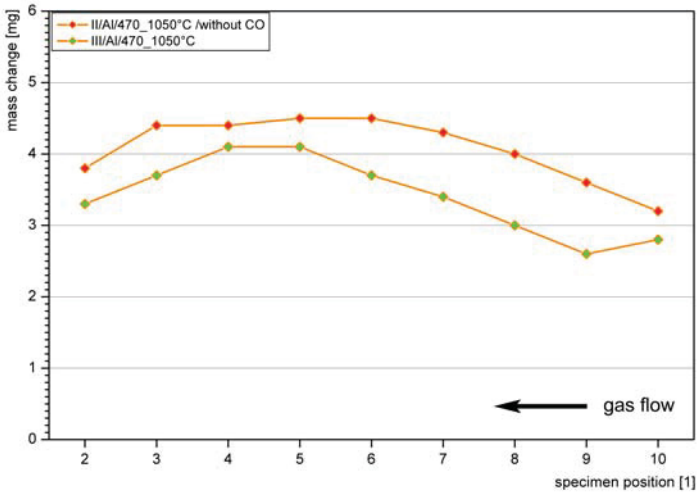

Fig. 4.1: Substrate mass change observed for the undoped aluminium oxide system

By feeding 4.5 l/h HCl gas for $AlCl_3$ generation, 6.96 g Al granules in experiment II and 8.98 g Al granules in deposition II were volatilized, which equal to volatilisation rates of 0.53 g/l_{HCl} and 0.62 g/$l_{HCl.}$

4.1.1.2 Scanning electron microscopy

All specimens showed crystalline structure and grain size < 3 µm. At the high substrate temperatures of specimen position 4, the gas composition without CO (cf. Fig. 4.2 a) shows slightly smaller grains compared to that one deposited using a CO containing gas mixture (cf. Fig. 4.2 b). At the lower deposition temperatures of specimen position 7 the grain size appears comparable. Fig. 4.2 d shows a somewhat more plate like structure, compared to other specimens.

The fracture cross-section images show an oxide layer thickness comparable to the TiCN precoated layer, about 2 µm. Surface roughness varies slightly as can be seen in Fig. 4.3 a to d without significant dependency.

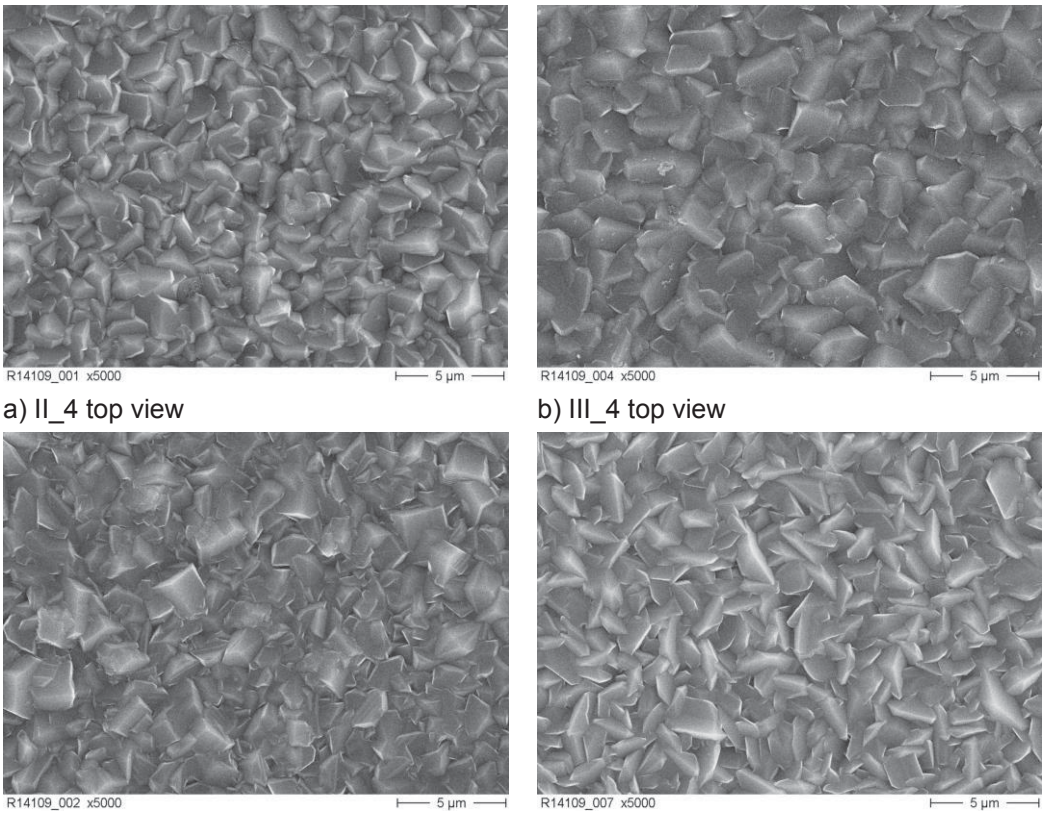

a) II_4 top view b) III_4 top view

c) II_7 top view d) III_7 top view

Fig. 4.2: SEM surface micrographs of depositions II and III

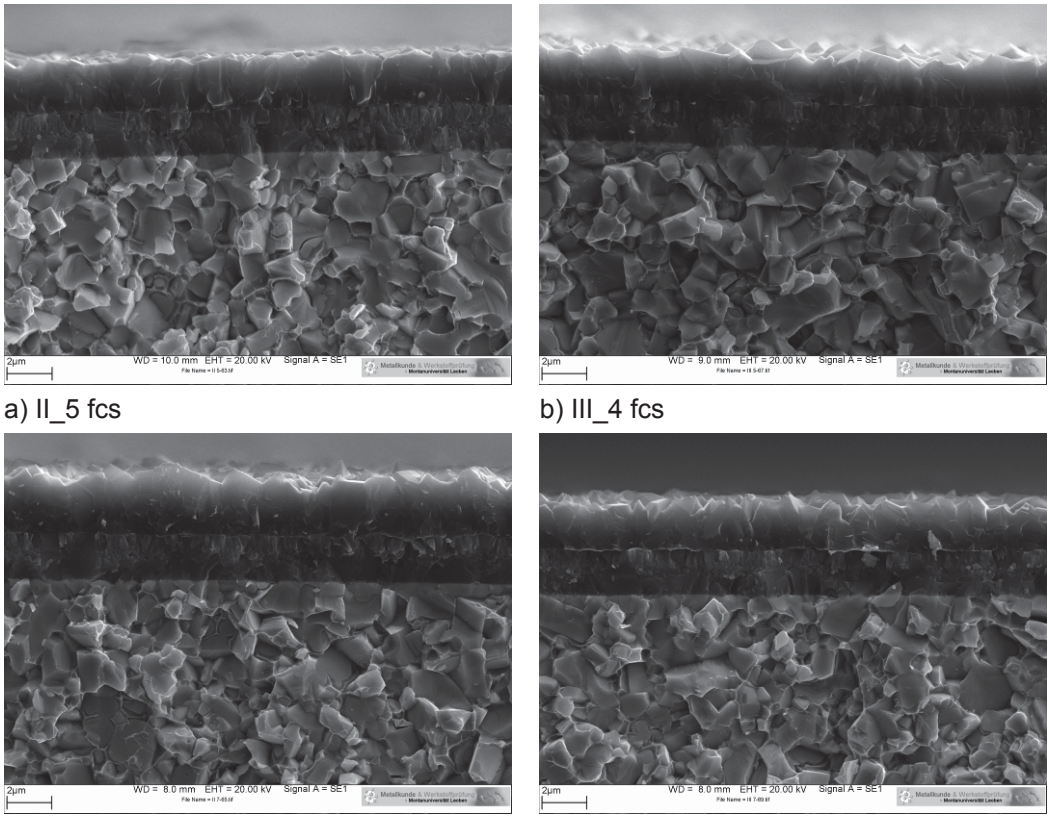

a) II_5 fcs b) III_4 fcs

c) II_7 fcs d) III_7 fcs

Fig. 4.3: Fracture cross-sections (fcs) of deposition II and III

4.1.1.3 Glow discharge optical emission spectroscopy

As expected, quantitative analysis of specimen position 4, 6, and 8 revealed oxygen and aluminium as main components. Contents of nitrogen and carbon were detected in portions < 10 at.-%. Molybdenum fraction supplied by reactor material could be quantified with < 0.01 at.-%.

4.1.1.4 X-ray diffraction analysis

Differences between structures of deposition II and III could only by found in titanium oxide modifications, as shown in Fig. 4.4 and Fig. 4.5. The main peaks of titanium nitride and α-Al_2O_3 are found on similar diffraction angles. No significant dependency of composition on specimen positions could be found. α-Al_2O_3 was the only polymorph which could be detected.

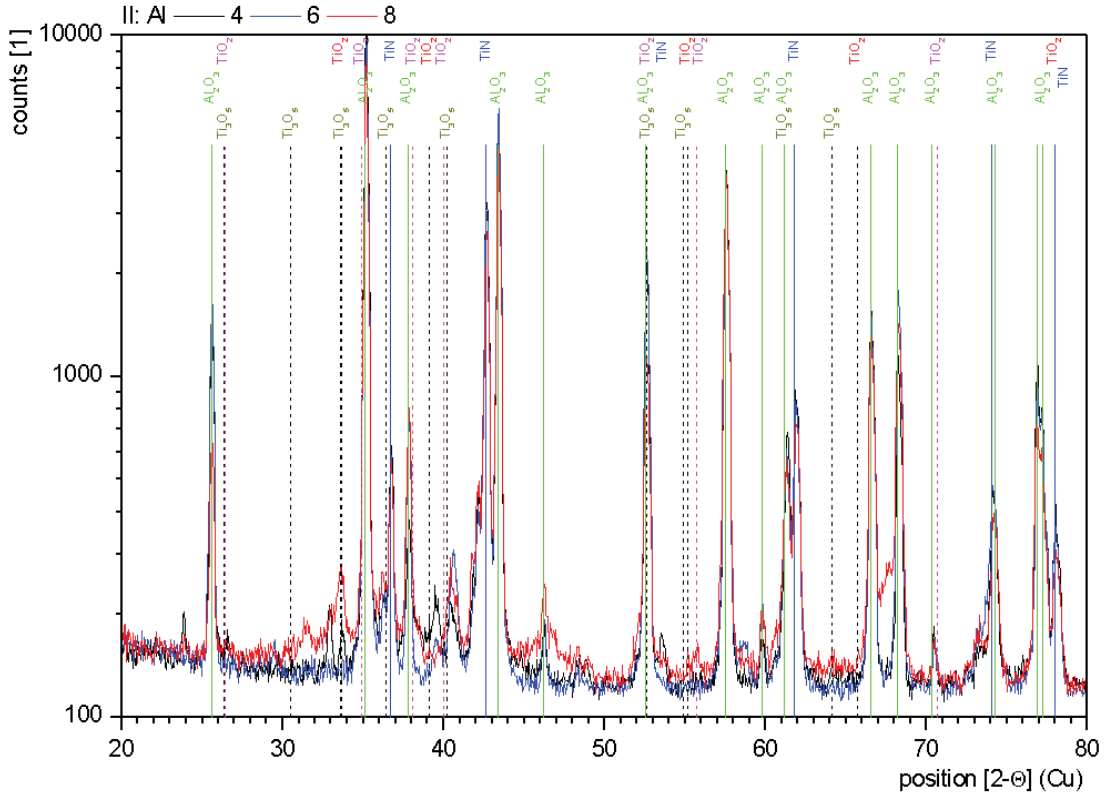

Fig. 4.4: XRD measurements of deposition II for positions 4, 6 and 8

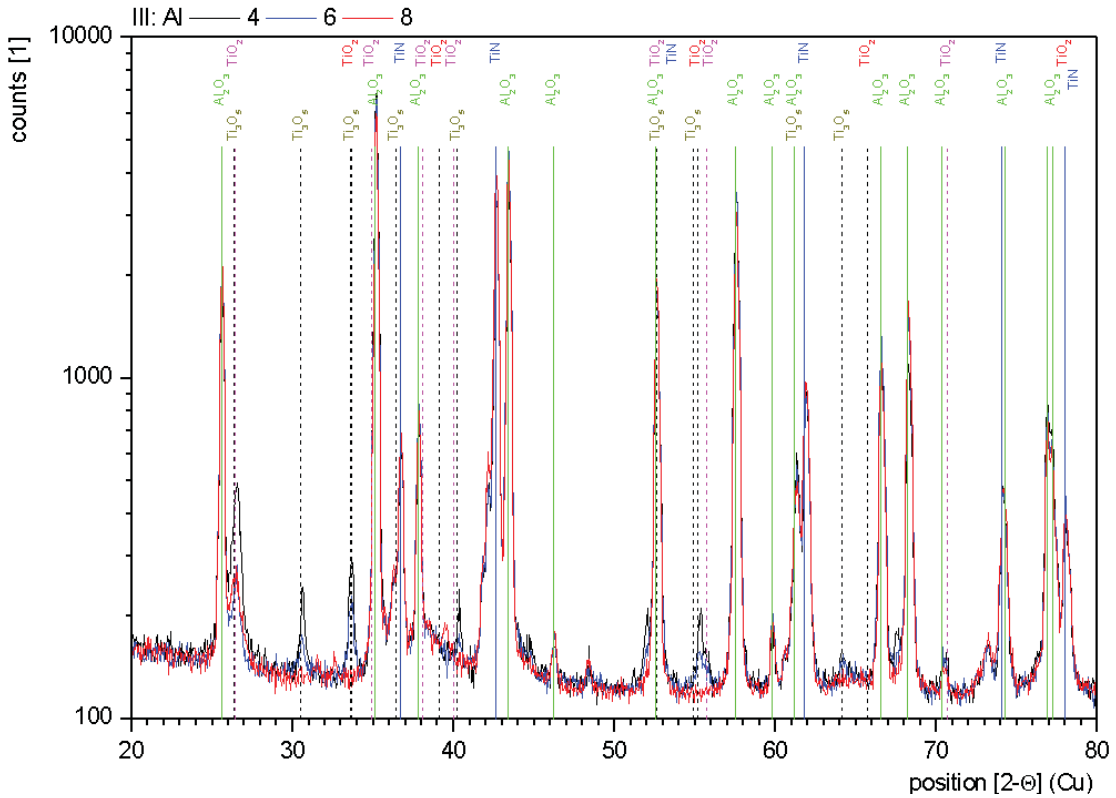

Fig. 4.5: XRD measurements of deposition III for positions 4, 6 and 8

4.1.2 Aluminium chromium oxide system

Six experiments, X to XIV and XVII, were performed within the aluminium chromium oxide system, out of these runs one (XIV) on molybdenum substrate. The latter led to similar mass change and structure as found on precoated cemented carbide. A powder metallurgical alloy containing 20 wt.-% chromium was used as precursor. Deposition of needle like structures of chromium oxide (Fig. 4.6) occurred in experiments X and XIII on the reactor cap, where halide gas and oxygen carrier were mixed.

Fig. 4.6: Needle like Cr_2O_3 on reactor cap

At the furnace tube, between reactor and specimens, voluminous carbon whisker growth was observed. The temperature range of this region was approximately 600 °C to 900 °C. Carbon whiskers were also found on first specimen positions in gas flow direction (X_10), as can bee seen in Fig. 4.7. Also chromium could be detected via EDX measurements.

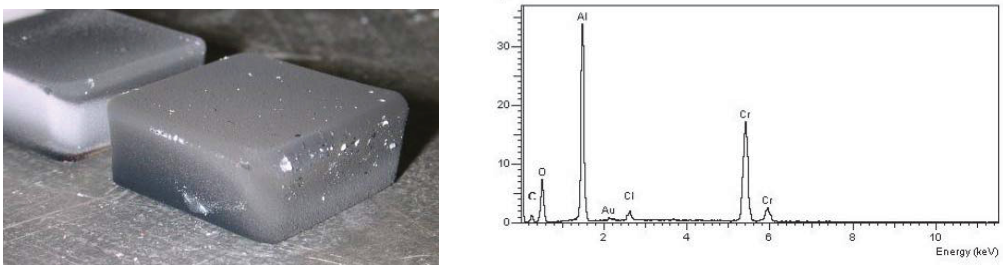

Fig. 4.7: Carbon whisker growth on specimen X_10 and EDX analysis

4.1.2.1 Gravimetric analysis

The high mass changes, at maximum 295 mg in deposition run X, were caused by carbon whisker growth as shown above. By rising the CO_2 content in the feed gas from 4.8 l/h to a maximum of 12.8 l/h, the whisker formation could be shifted to lower temperatures as can be seen in Fig. 4.8.

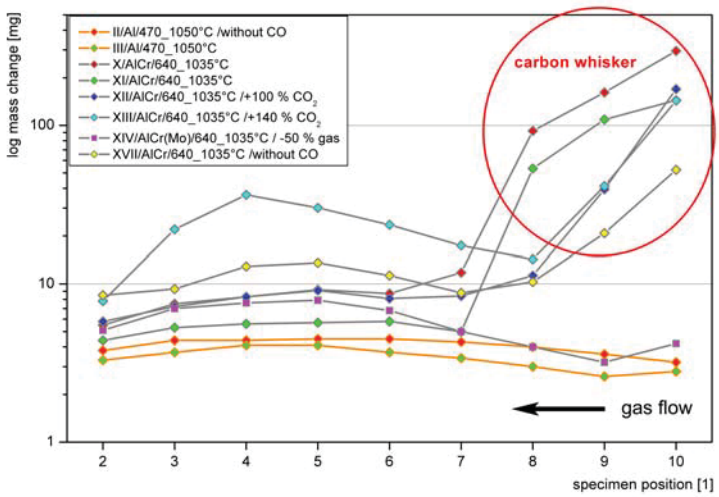

Fig. 4.8: Substrate mass change observed for the aluminium chromium oxide system compared to the reference experiment III and experiment II

All feed gas variations including chromium lead to higher mass changes compared to the reference aluminium oxide deposition. This can possibly be explained by the carbon whisker deposition. As a consequence of this, the equilibrium between CO/CO_2 and H_2/H_2O in the feed gas is influenced. Less carbon containing species are transported towards deposition zone. The oxygen which was formerly bound in the form of CO, which is not involved in the deposition process, is now available for aluminium oxide deposition. Probably, the whisker growth is forced by a catalytic reaction caused by the presence of chromium. The observed mass changes, except carbon whiskers, showed also a clear temperature dependency of the growth rate. Hence, a surface reaction limited process could be assumed. The enhanced mass changes related to the raised CO_2 content in the feed gas were disproportionally high, which could be identified by comparing the results X, XII and XIII in Fig. 4.8.

The volatilization of the AlCr-precursor was comparable to pure aluminium granules, in a range of 5.6 to 6.0 g/l_{HCl} for all depositions on the aluminium chromium oxide system. The volatilization will mainly be influenced by the amount of HCl in feed gas.

4.1.2.2 Scanning electron microscopy

Deposition X with a low CO_2 content of 4.8 l/h specimen exhibits bigger, isolated grains on specimen position no. 6 (Fig. 4.9 b) compared to position no. 4 (Fig. 4.9 a) which itself appears to be coarser than the comparable specimen position of experiment III (cf. Fig. 4.2 b). By raising the CO_2 content to 9.6 l/h (experiment XII), the formation of this coarse structure could be suppressed. Position 4 and 6 showed comparable structure and grain size as can be seen in Fig. 4.9 d and e.

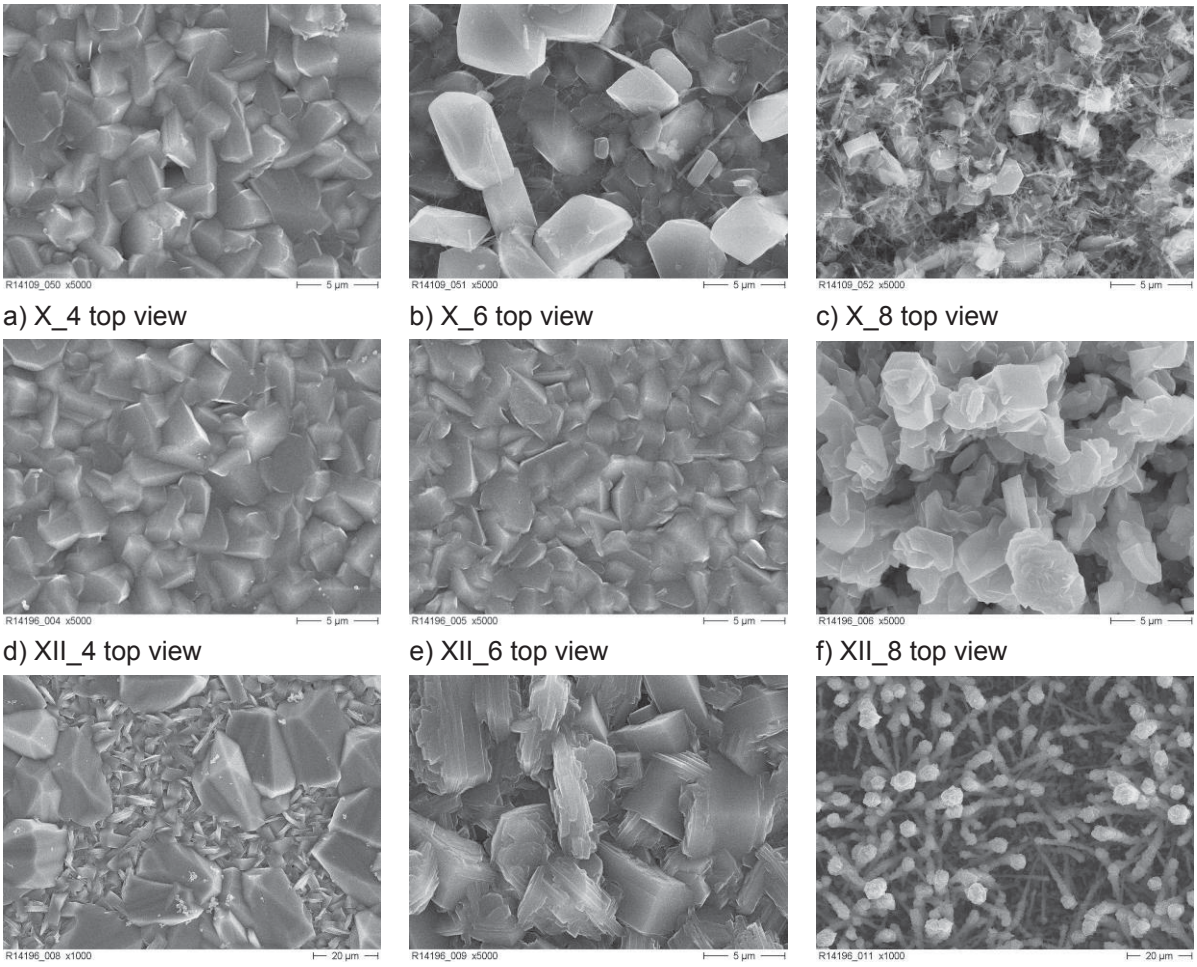

a) X_4 top view b) X_6 top view c) X_8 top view

d) XII_4 top view e) XII_6 top view f) XII_8 top view

g) XIII_4 top view x1000 h) XIII_6 top view i) XIII_8 top view x1000

Fig. 4.9: Surface structure using different CO_2 contents in feed gas

For the maximum CO_2 content of 11.8 l/h in feed gas, two phases are formed and the grain size becomes much bigger. In order to realize an overview of structure, lower magnification was used for Fig. 4.9 g. Fig. 4.10 evidences the higher growth rate of deposition XIII, where layer thickness of 12 µm at maximum could be observed.

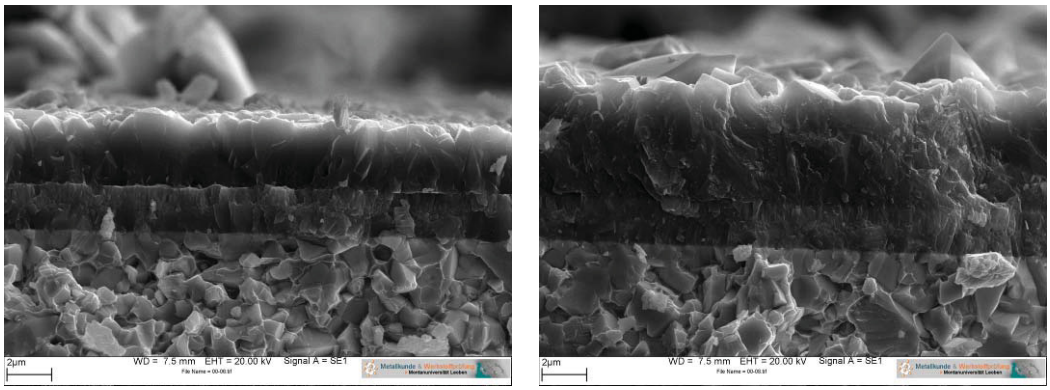

a) XII_7 fcs b) XIII_7 fcs

Fig. 4.10: Fracture cross-sections (fcs) of depositions XII and XIII

Deposition XVII should be used to investigate the influence of CO in the feed gas, which is the only varied parameter compared to experiment X. The growth mechanism indicated by position 4 (cf. Fig. 4.11 a) appears to be completely different and seems to be more one dimensional and perpendicular to the substrate. The coarse structure of specimen X_6 could not be reproduced under this atmosphere. The grain size of sample XVII_6 (cf. Fig. 4.11 b) is bigger, compared to reference experiment III.

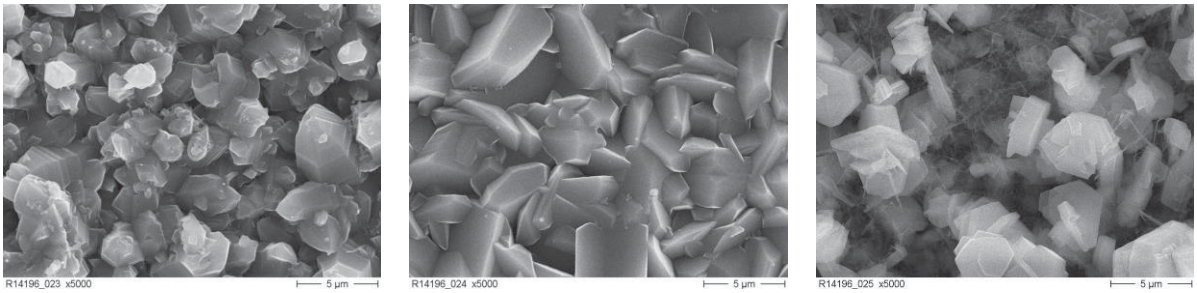

a) XVII_4 top view b) XVII_6 top view c) XVII_8 top view

Fig. 4.11: Surface structure of experiment XVII: Influence of CO in feed gas on aluminium chromium system

For determining the influence of the substrate material, experiment XIV was performed on molybdenum, using a gas composition similar to experiment XII (only the total gas flow was reduced by 50 %). The structure is more comparable to deposition XIII using higher CO_2 contents in the feed gas. In Fig. 4.12 a and b, also big grains of approximately 20 µm size and evidence for a two-phase structure could be found. These bigger grains decrease in amount and size at low temperatures (Fig. 4.12 c).

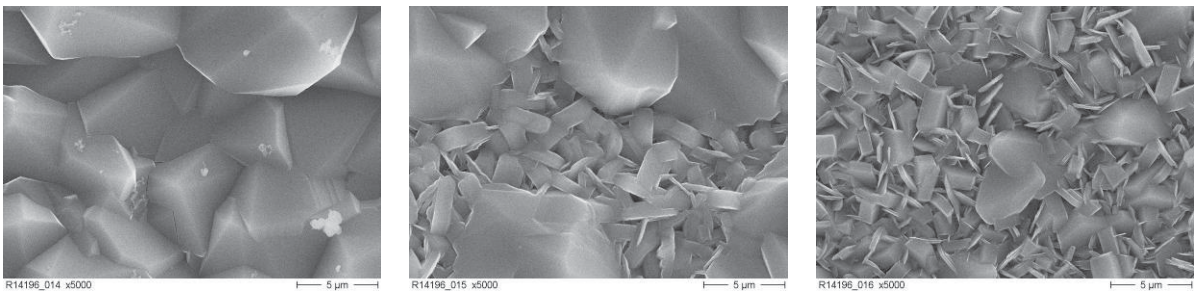

a) XIV_4 top view b) XIV_6 top view c) XIV_8 top view

Fig. 4.12: Influence of substrate material on aluminium chromium system

4.1.2.3 Glow discharge optical emission spectroscopy

The quantitative analysis of the chromium content could not be appointed certainly, because of the overlapping Cr and Ti peaks. Measured values are given in Fig. 4.13, where it can be seen that the maximum values of 11 at.-% and 14 at.-% were reached nearby the reactor, at lower substrate temperatures. No clear dependency of the chromium dispersion could be found. Disregarding the two specimens with the highest chromium content, only a small temperature dependency could be assumed. The maximum values shown in Fig. 4.13 were commonly observed underneath the surface of deposited layer which can be caused by segregation effects.

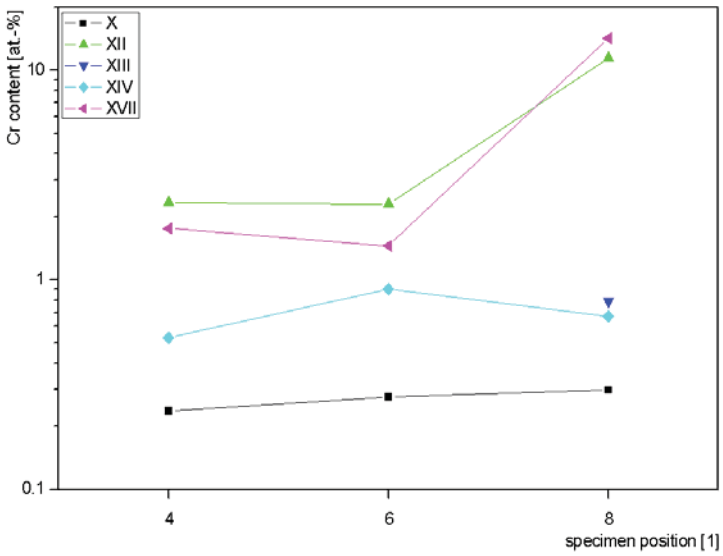

Fig. 4.13: Maximum chromium content of deposited layers

4.1.2.4 X-ray diffraction analysis

Many different modifications of aluminium oxide were detected via X-ray diffraction analysis, which are listed in Tab. 4.2. α-Al_2O_3 occurred in almost all specimens. If only traces of aluminium oxide polymorphs have been found, they were set into round brackets. Chromium containing species could only be detected on four specimens, which are highlighted in yellow in Tab. 4.2:

- XII_8: traces of $Cr_{0.05}Al_{0.95}$, Cr_2Al and C_2Cr_3 could be verified
- XIV_8: small amounts of Cr could be found
- XVII_4: Cr_xC_y was detected in traces
- XVII_8: Cr_2O_3 was found

Tab. 4.2: Aluminium oxide modifications observed in the aluminium chromium oxide system, listed in order of amount; Specimens containing chromium species are marked in yellow

	3	4	6	8
$X_{AlCr/640\_1035°C}$		α (ά)	α (κ)	α, κ, κ'
$XI_{AlCr/640\_1035°C}$	α (κ)	α	α	κ, θ (δ)
$XII_{AlCr/640\_1035°C/9.6\ l/h\ CO2}$		α	α	α (χ, δ)
$XIII_{AlCr//640\_1035°C/12\ l/h\ CO2}$	α (κ)	α, κ (d)	κ, θ, α (χ)	α, κ, θ
$XIV_{AlCr/640\_1035°C/\ -50\%\ tot.\ gas}$		α (χ, ι)	α (κ, θ)	κ, α (θ)
$XVII_{AlCr/640\_1035°C/\ without\ CO}$		α	α	α, κ, θ

4.1.3 Aluminium tin oxide system

The experiments IV, V and VI, were performed within this system, where temperature and hydrogen content were varied for these deposition runs. Because of the low melting point of tin, an aluminium tin alloy containing 20 wt.-% tin was used to realize the precursor temperatures of 600 °C without a liquid phase. Three experiments were performed within this oxide system, varying the deposition temperature and hydrogen content in feed gas. The aluminium-tin alloy containing 20 wt.-% tin was produced pyrometallurgically from aluminium granules and a tin foil. The melt was granulated in water and separated by size.

After each deposition, small metallic spheres with shiny appearance were found at the bottom of the molybdenum reactor, especially nearby the reactor cap. These spheres, marked in Fig. 4.14, consist mainly of tin which was confirmed by thermal analysis. It is assumed that only very small amounts of tin could be transported to the substrates. The reason for this effect could be the high affinity of aluminium to chlorides, which could be estimated using HSC-chemistry [11]. In this case, tin chloride would be reduced to metallic tin in the presence of metallic aluminium, which would react to aluminium chloride.

Fig. 4.14: Metallic tin spheres formed in the molybdenum reactor during deposition VI

4.1.3.1 Gravimetric analysis

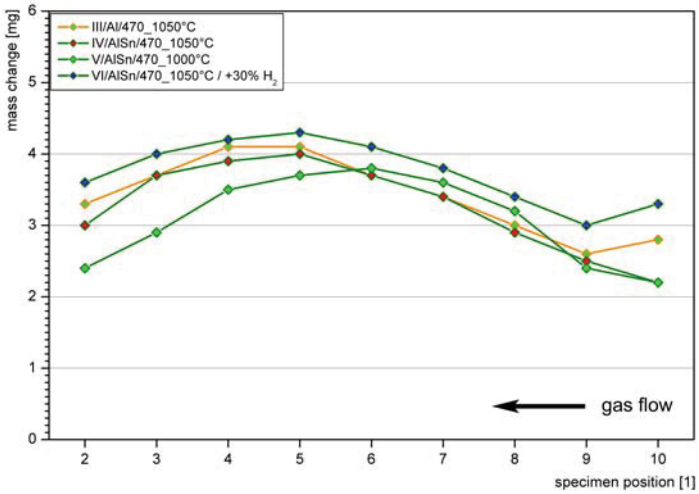

Fig. 4.15: Substrate mass change observed for the aluminium tin oxide system compared to the reference experiment III

Experiment IV agrees well with deposition III, where the same parameters were applied. The measured mass changes are quite similar (cf. Fig. 4.15), respecting the weighting accuracy of ± 0.1 mg. A drop of the deposition temperature in experiment V led to lower deposition rates and a shift of the maximum mass gain against gas flow direction towards higher specimen position numbers. As expected, the raised hydrogen content in experiment VI yields a higher deposition rate. The volatilisation of precursor was comparable to experiments with aluminium granules, between 0.61 g/l_{HCl} and 0.65 g/l_{HCl}. So it can be concluded that aluminium is the mainly vaporised species.

4.1.3.2 Scanning electron microscopy

The surface images of the deposited layers showed an analogous structure and grain size for all specimens. An influence of temperature on the grains size can be found by comparing specimen positions 4, 6 and 8 (cf. Fig. 4.16). With decreasing substrate temperature the structure becomes finer, but this effect is probably caused by a decreased layer thickness. Only one phase is evidenced from the surface images, with the exception of some particles on specimen IV_8.

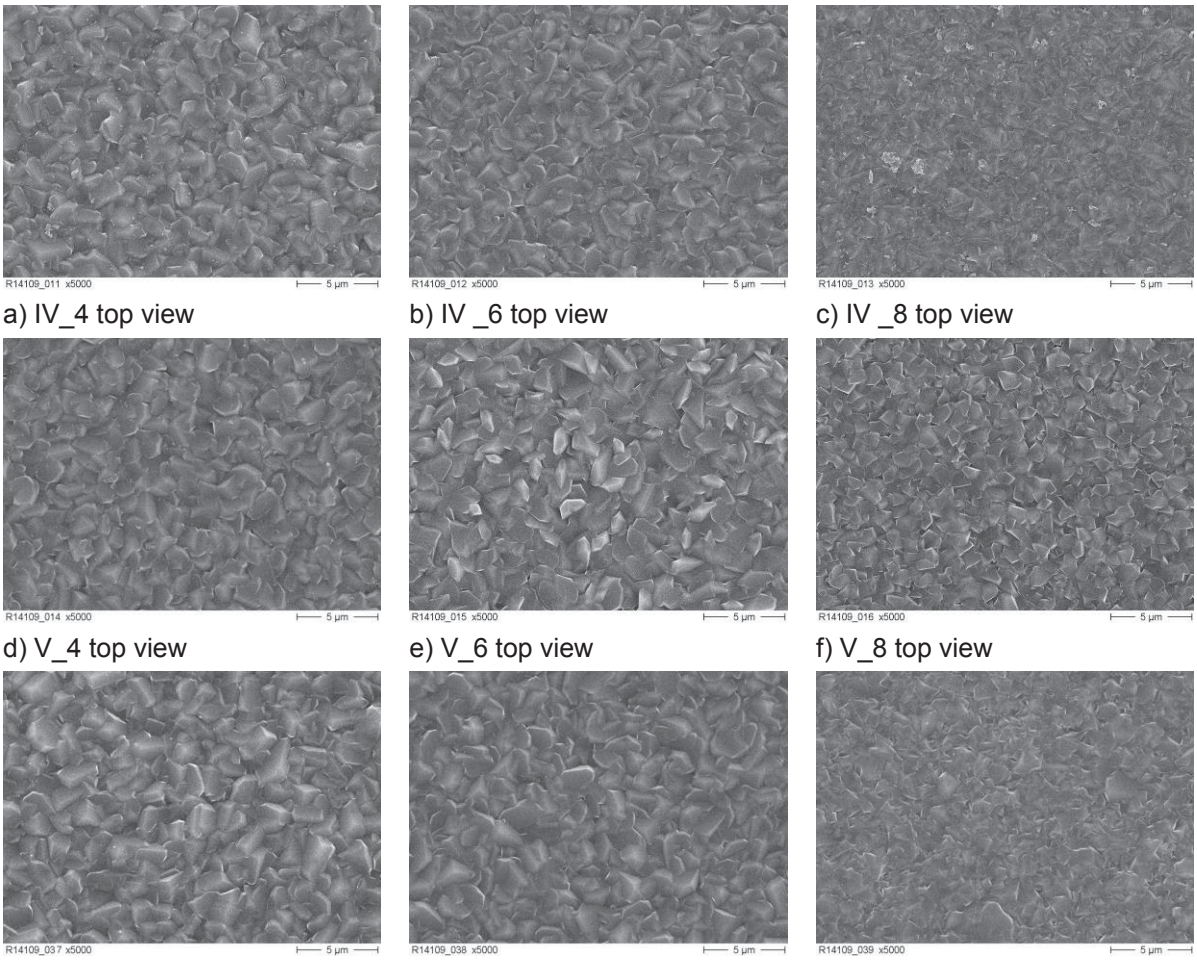

a) IV_4 top view b) IV _6 top view c) IV _8 top view

d) V_4 top view e) V_6 top view f) V_8 top view

g) VI_4 top view h) VI_6 top view i) VI_8 top view

Fig. 4.16: Surface structure of coatings within the aluminium tin oxide system varying substrate temperature and hydrogen content

The achieved layer thickness was about 2 µm on the investigated specimen positions 5 and 7 (cf. Fig. 4.17). Surface roughness and appearance of structure are comparable to reference deposition III.

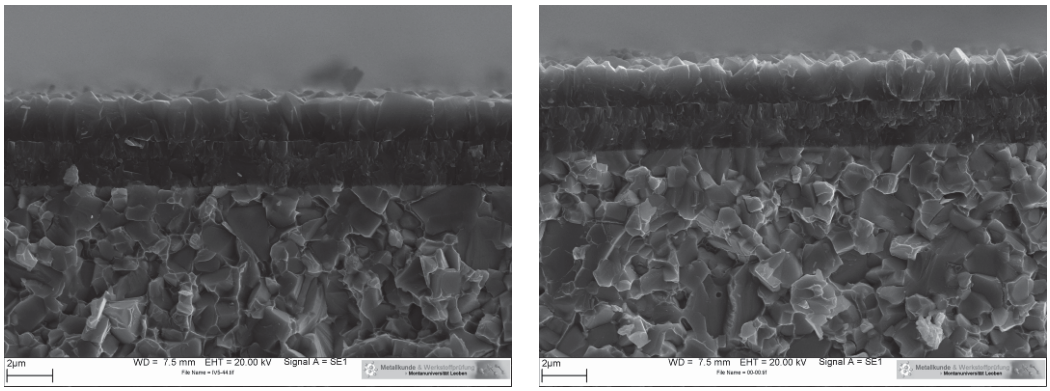

a) IV_5 fcs b) IV_7 fcs

Fig. 4.17: Fracture cross-sections (fcs) of deposition IV

4.1.3.3 Glow discharge optical emission spectroscopy

Using GDOES analysis, tin amounts < 0.1 at.-% could be detected. All results were nearly in the same magnitude, so no dependency on the deposition parameters can be worked out. Values related to specimen position and deposition condition can be seen in Fig. 4.18.

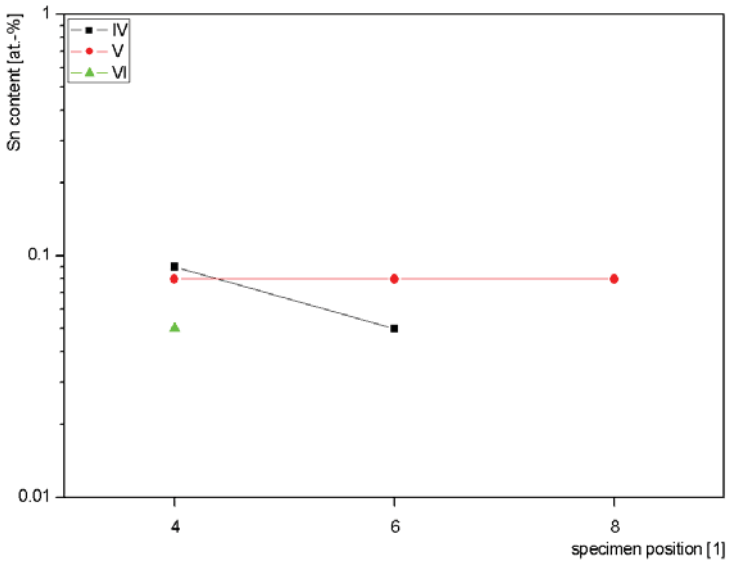

Fig. 4.18: Maximum tin content of deposited layers

Considering the GDOES profiles it can be seen, that the main amounts of tin were located nearby the surface, which may be caused by segregation effects. Fig. 4.19 shows that the curves of aluminium and oxygen exhibit a shift relative to each other.

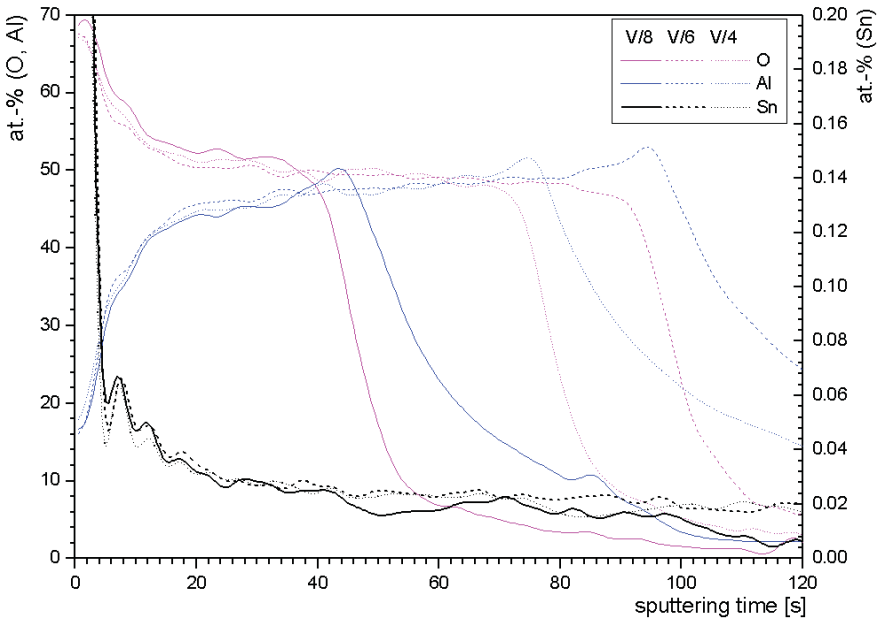

Fig. 4.19: Quantitative GDOES analysis of deposition V

4.1.3.4 X-ray diffraction analysis

The predominant aluminium oxide modification was α-Al_2O_3. Traces of σ-Al_2O_3 could only be found on specimen IV_8. This modification can be distinguished from α-Al_2O_3 by a specific vacancy arrangement [55]. Insignificant amounts of SnO_2 could be verified by XRD measurements on five samples, which are shaded in yellow in Tab. 4.3. In deposition VI also SnO could be detected beside SnO_2.

Tab. 4.3: Aluminium oxide modifications within the aluminium tin oxide system; Specimens containing tin species are shaded in yellow

	4	6	8
$IV_{AlSn/470\_1050°C}$	α	α	α (σ)
$V_{AlSn/470\_1000°C}$	α	α	α
$VI_{AlSn/470\_1050°C/+30\ \%\ H2}$	α	α	α

4.1.4 Aluminium niobium oxide system

Placing metallic niobium and aluminium granules in a proportion of 20 wt.-% niobium in the reaction chamber should lead to a niobium oxide doping of aluminium oxide. Two experiments with similar gas composition were performed. The difference was the distribution of argon which was usually 50 % through the central tube and the other 50 % were inserted at the inlet flange (deposition VII). In experiment VIII the main amount of 80 % was fed via the inlet flange.

4.1.4.1 Gravimetric analysis

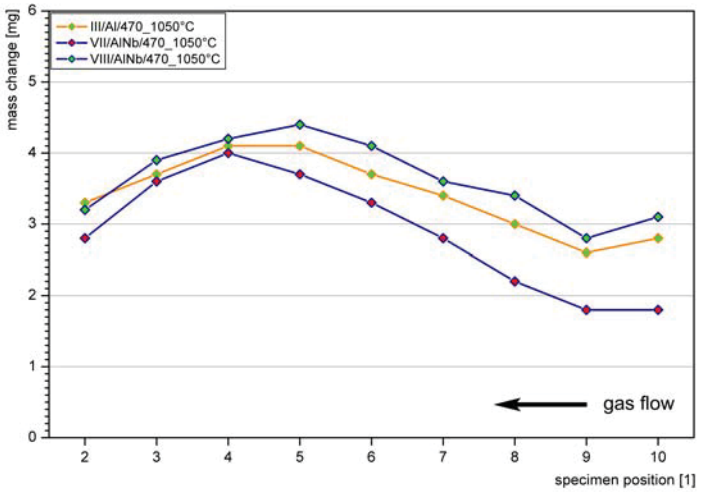

Fig. 4.20: Substrate mass change observed for the aluminium niobium oxide system compared to the reference experiment III

The deposition VII showed similar results compared to the reference experiment III, while for deposition VIII lower mass changes were determined (Fig. 4.20). Aluminium granules and metallic niobium were weighted separately, but no significant mass change of the niobium precursor could be measured. The volatilisation rate of aluminium was 0.57 g/l_{HCl} and 0.62 $g/l_{HCl.}$

4.1.4.2 Scanning electron microscopy

The coating surface and the structure appear more fine grained compared to reference deposition III, especially at the low temperature of specimen position 8. The grain size is comparable to the layers deposited within the aluminium tin oxide system. This is also valid for the correlation of grain size and substrate temperature. One difference which could be found were the bigger particles consisting mainly of Al_2O_3 on the specimen surface, as shown in Fig. 4.21 b, c and e.

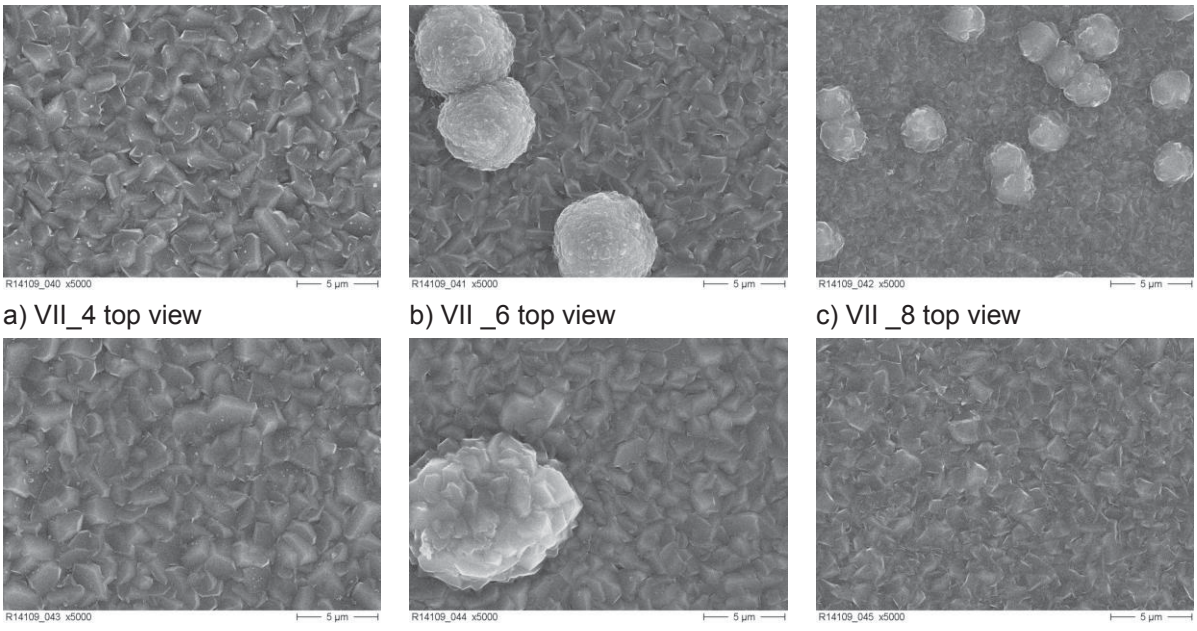

a) VII_4 top view b) VII _6 top view c) VII _8 top view

d) VIII_4 top view e) VIII_6 top view f) VIII_8 top view

Fig. 4.21: Surface structure observed within the aluminium niobium oxide system with varying gas feeding

The shape of these structures can be identified better using fracture cross-section images, as illustrated in Fig. 4.22. They have the shape of hemispheres and look like water droplets on a surface. Thus, a homogenous nucleation seems to be unlikely [7]. With increasing temperature the number of particles decreases, while their size increases. This effect maybe caused by a diffusion controlled process, which is temperature dependent [8]. The achieved layer thickness was less than 2 µm, which is lower than that one obtained in reference deposition III.

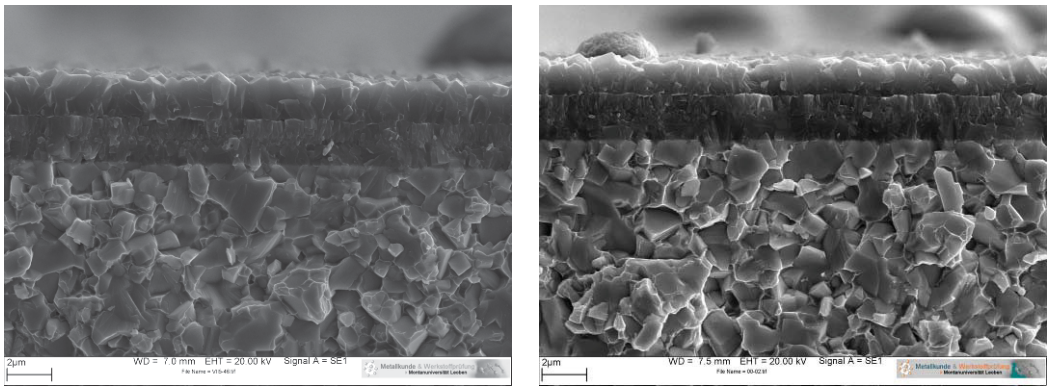

a) VII_5 fcs b) VII_7 fcs

Fig. 4.22: Fracture cross-sections (fcs) of deposition VII

4.1.4.3 Glow discharge optical emission spectroscopy

Niobium could only be found in amounts < 0.02 at.-%. The fraction of detected molybdenum was for all six specimens 0.04 at.-%, so the influence of niobium species on coating morphology might be decisive.

4.1.4.4 X-ray diffraction analysis

Only the α-Al_2O_3 modification could be detected on the investigated samples. For specimen VIII_4, traces of $TiNbO_4$ and NbN were found. Also in sample VIII_6, the niobium containing species NbO_2 and $TiNbO_4$ could be determined in small amounts. These samples are shaded in yellow in Tab. 4.4.

Tab. 4.4: Aluminium oxide modifications within the aluminium niobium oxide system; Specimens containing niobium species are marked in yellow

	4	6	8
$VII_{AlNb/470\_1050°C}$	α	α	α
$VIII_{AlNb/470\_1050°C}$	α	α	α

4.1.5 Aluminium strontium oxide system

In the single reactor alignment, only one experiment (#IX) was performed using aluminium granules and solid salt $SrCl_2 \cdot 6H_2O$ inside the molybdenum reactor. While heating to the deposition temperature, condensed water was observed in the exhaust gas system, which is assumed to originate from chemically bonded water. For further experiments in the double reactor alignment the salt was dried to prevent condensation.

4.1.5.1 Gravimetric analysis

The mass change observed for deposition IX was lower than for the comparable reference deposition III. Specimen IX_2 could not be evaluated, because of coating delamination. These delaminated fragments, analysed by XRD, mainly consist of titanium oxide. The temperature dependency of the mass change is similar to deposition III, as can be seen in Fig. 4.23. The shift of the maximum mass change can be explained by slightly different temperature fields, caused by the higher temperature in heating zone 1.

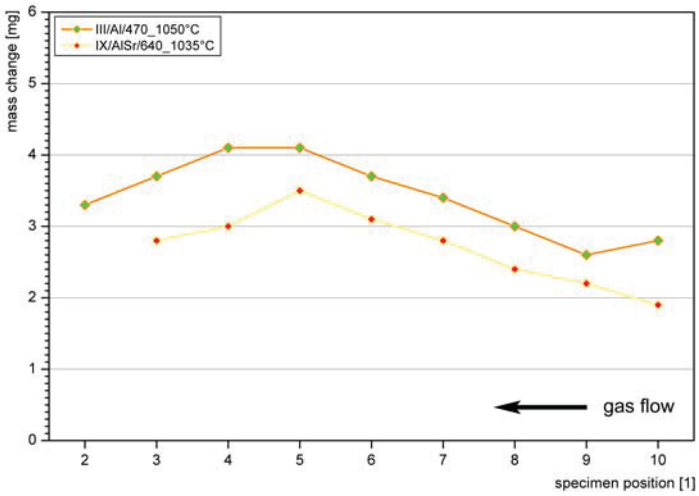

Fig. 4.23: Mass change observed in the aluminium strontium oxide system compared to the reference experiment III

The volatilisation rate of the precursor was relatively high. Within experiment IX, 0.91 g/l_{HCl} were vaporised, which can be explained by dehydration of the salt used. Drying the strontium chloride at 150 °C/168 h led to a separation of the chemically bonded water. The resulting mass loss agreed well with the mass of bonded water. For further experiments, this dried salt was used as precursor.

4.1.5.2 Scanning electron microscopy

The surface structure appears to be single-phase, except particles on specimen IX_4. A coarsening of the grains with increasing substrate temperature can also be observed (cf. Fig. 4.24). Fracture cross-sections, illustrated in Fig. 4.25, show comparable structure and layer thickness in the range of 1 to 2 µm.

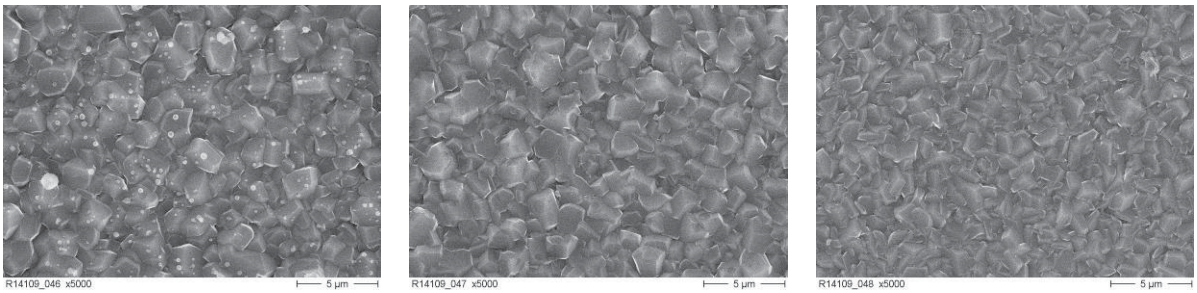

a) IX_4 top view b) IX_6 top view c) IX_8 top view

Fig. 4.24: Surface structure observed for the aluminium strontium oxide system, showing coarser grains with increasing deposition temperature from sample 8 (c) to 6 (b) and 4 (a)

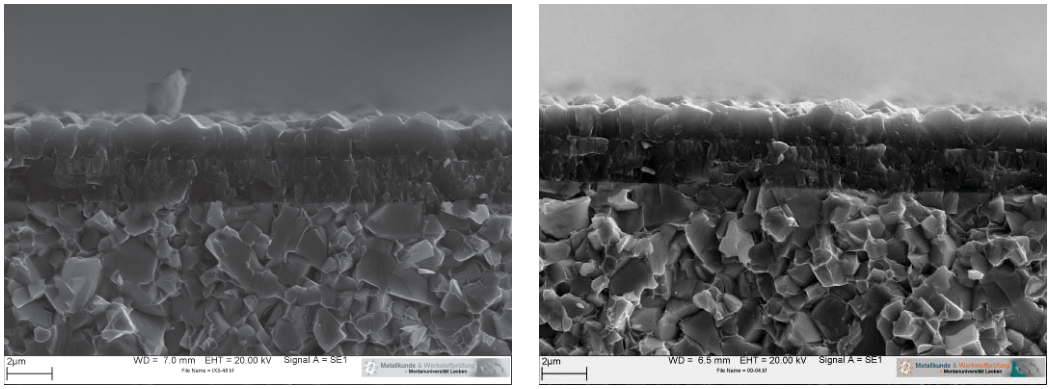

a) IX_5 fcs b) IX_7 fcs

Fig. 4.25: Fracture cross-sections (fcs) of deposition IX

4.1.5.3 Glow discharge optical emission spectroscopy

The elemental distribution determined via GDOES measurements showed an accumulation of strontium close to the coating surface. Maximum peak values were found for a depth corresponding to the surface roughness. The highest total amount was obtained for the highest substrate temperature of specimen 4, followed by specimen 8 as can be seen in Fig. 4.26. Sample XI_6 only contained up to 0.012 at.-% Sr. A slight accumulation of strontium can also be found close to the interface to the TiCN under-layer.

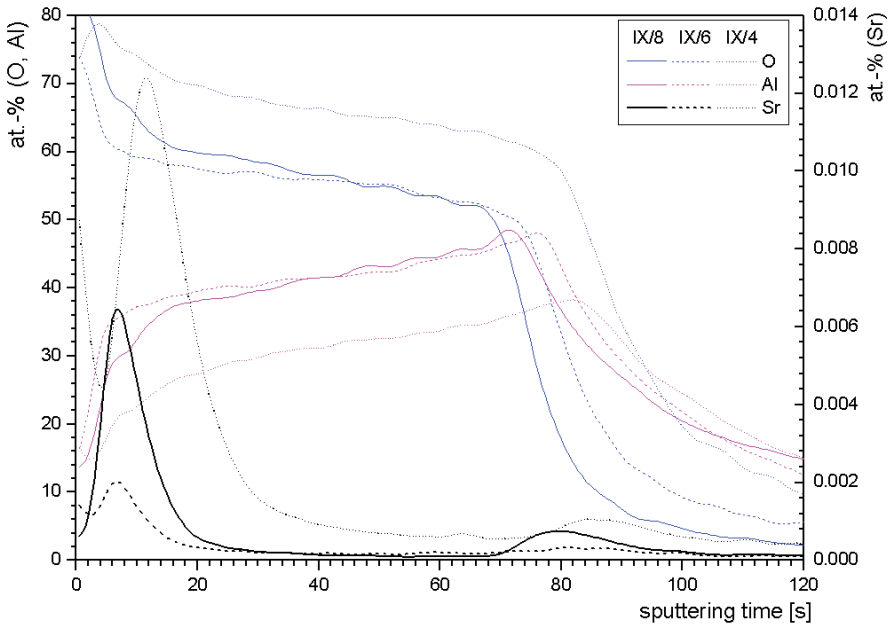

Fig. 4.26: Quantitative GDOES analysis for deposition IX

4.1.5.4 X-ray diffraction analysis

Mainly α-Al_2O_3 could be detected on the specimens of deposition run IX, as shown in Tab. 4.5. The only exception was sample IX_6, where also traces of κ-Al_2O_3 could be determined. No strontium containing species could be detected by XRD analysis.

Tab. 4.5: Aluminium oxide modifications on aluminium strontium oxide system

	4	6	8
$IX_{AlSr/640\_1035°C}$	α	α (κ)	α

4.2 Double reactor alignment

4.2.1 Aluminium tin oxide system

The experimental setup was adapted, as described in chapter 3.1.2. Using this arrangement deposition runs XV, XXI and XXII were performed. Experiment XV was done with reference parameters, only the CO_2 content was increased from 4.8 l/h to 9.8 l/h. Tin oxide was formed at the end of the inner feed tube as can be seen in Fig. 4.27. Thus the deposition temperature was lowered in the following experiments.

Fig. 4.27: Tin oxide formed on the reactor cap

Depositions XXI and XXII were performed on molybdenum substrates using very low volatilisation temperatures. For run XXI, the reactor temperature was set to 300 °C for $AlCl_3$ generation and a maximum substrate temperature of 665 °C was applied. The increase of the temperature gradient targeted for deposition run XXII could not be achieved. The main reason for the limitation of the temperature gradient is the heat conduction of the refractory tube, which is too high for the realisation of a low reactor temperature. During the experiment, the reactor temperature raised from 270 to 320 °C and no stable deposition conditions could be reached.

4.2.1.1 Gravimetric analysis

Deposition XV shows unusual high mass changes on positions 4, 6 and 7 (cf. Fig. 4.28). No clear explanation could be found. The mass change related to the specimen positions of experiment XXI is different to those of deposition III. The observed maximum shifted to lower temperatures, which indicates that the mass change is not related to diffusion phenomena. Results from experiment XXII could not be evaluated, only mass loss could be found.

Despite the low reactor temperatures, the volatilisation rate of aluminium was 0.61 g/l_{HCl} and 0.69 g/l_{HCl} in experiments XXI and XXII, respectively. It can be assumed that the volatilisation of aluminium only depends on the amount of HCl gas, within the applied temperatures.

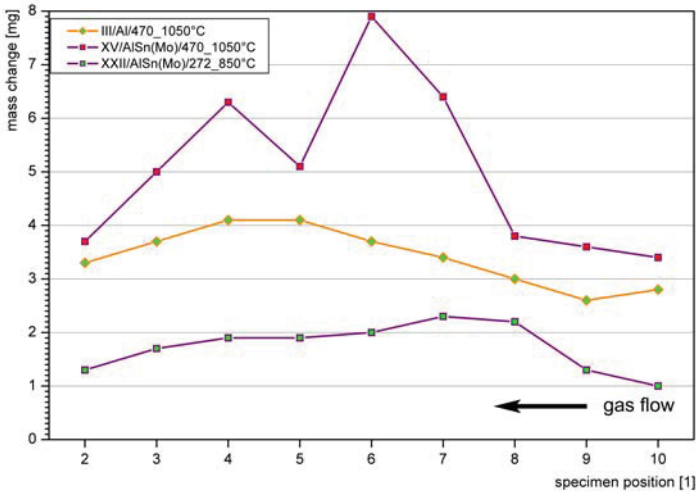

Fig. 4.28: Substrate mass change observed within the aluminium tin oxide system in the double reactor alignment compared to the reference experiment III

4.2.1.2 Scanning electron microscopy

The structure and morphology of all experiments and specimen positions are completely different. Specimens XXI_4, XXI_6, XXI_8 and XXII_8 (Fig. 4.29 d – f and j) exhibit a spherically shaped structure compared to other positions where sharp features can be seen on the coating surface. The surface and structure of specimens XV_6, XV_8 and XXII_6 appeared to be open and loose. Plate like grains could only be found on specimen XXII_4.

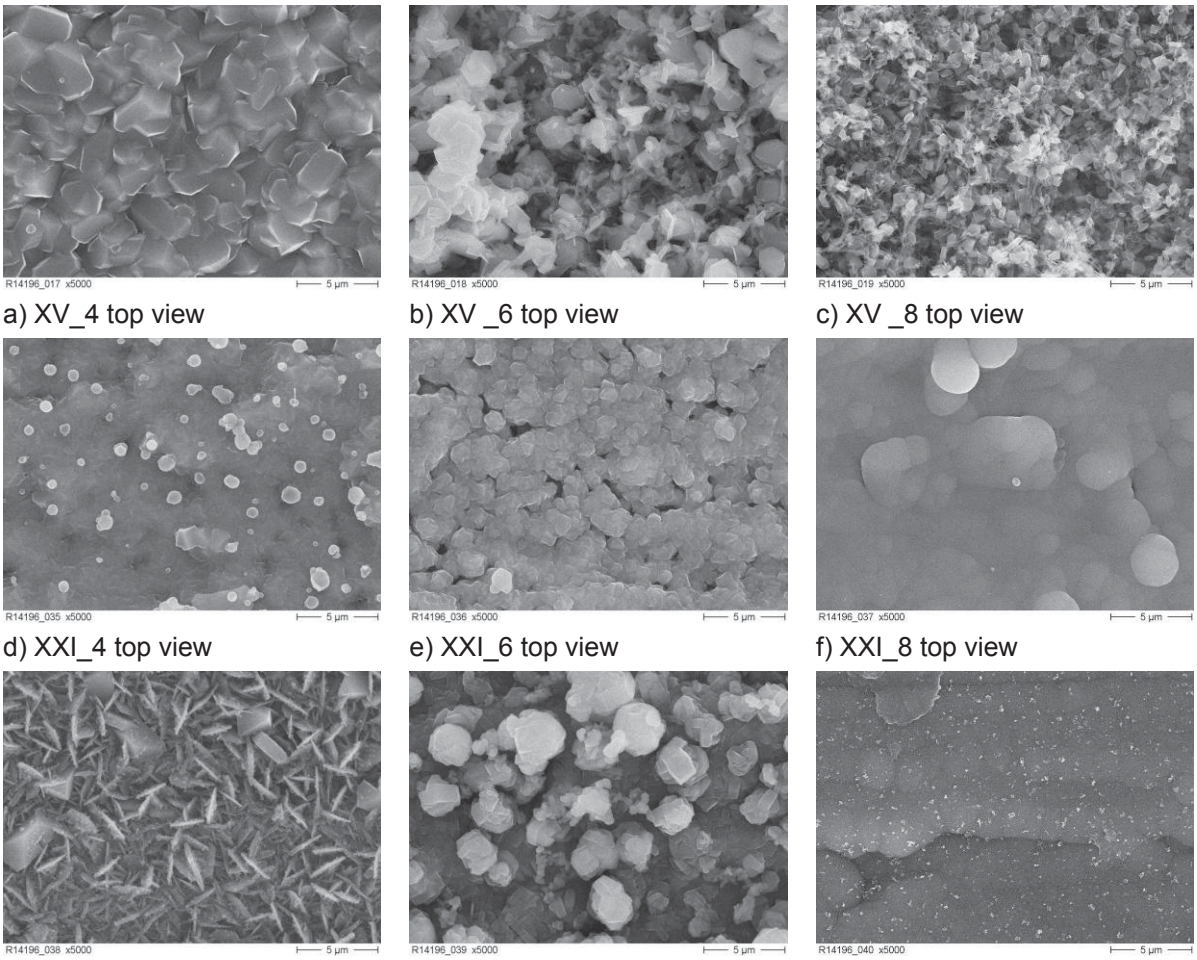

a) XV_4 top view b) XV _6 top view c) XV _8 top view

d) XXI_4 top view e) XXI_6 top view f) XXI_8 top view

g) XXII_4 top view h) XXII_6 top view i) XXII_8 top view

Fig. 4.29: Surface structure observed for the aluminium tin oxide system, with varying substrate temperature

4.2.1.3 Glow discharge optical emission spectroscopy

GDOES measurements of experiments XV and XXI could not be evaluated, because of strontium which was detected in all samples of experiment XXII. This may be caused by contamination of the refractory tube during a previous deposition run.

4.2.1.4 X-ray diffraction analysis

Many different aluminium oxide modifications were detected on the investigated specimens, which are listed in Tab. 4.6. Beside aluminium oxide, MoO_2 was detected on specimens of deposition XXI, which is marked in green. For the deposition run XXII also Mo_2C (XXII_4), $Mo(CO)_6$ (XXII_6) and traces of metallic strontium (XXII_8) could be detected. Because of these strontium contaminations, this deposition must be excluded from the further discussion.

Tab. 4.6: Aluminium oxide modifications observed within the aluminium tin oxide system; Specimens containing molybdenum oxide are highlighted in green

	4	6	8
$XV_{AlSn(Mo)/470\_1050°C}$	α (κ, θ)	κ, α, θ	α (κ, θ)
$XXI_{AlSn(Mo)/300\_700°C}$	α	α	-
$XXII_{AlSn(Mo)/272\_850°C}$	α (γ, θ)	γ, α	α

4.2.2 Aluminium strontium oxide system

Three deposition runs (XVI, XIX and XX) were performed to investigate this oxide system in the double reactor alignment. Experiments XIX and XX were performed to compare the volatilisation of solid and liquid strontium chloride. Differences between both experiments were the CO content in the feed gas of deposition XIX. In case of the higher reactor temperature, only a slight temperature gradient of less than 30 °C over specimen positions could be realized. The deposition time was reduced to 50 %, compared to reference deposition III. The thinner layer should lower the risk of spalling. Experiment XVI was stopped after 65 minutes because of a plugged feed gas system.

4.2.2.1 Gravimetric analysis

Mass changes observed for specimens 5 to 10 are nearly identical within the same experiment (cf. Fig. 4.30). The lower mass change of samples 2, 3 and 4 can be explained by the lower substrate temperature at the end of heating zone 3.

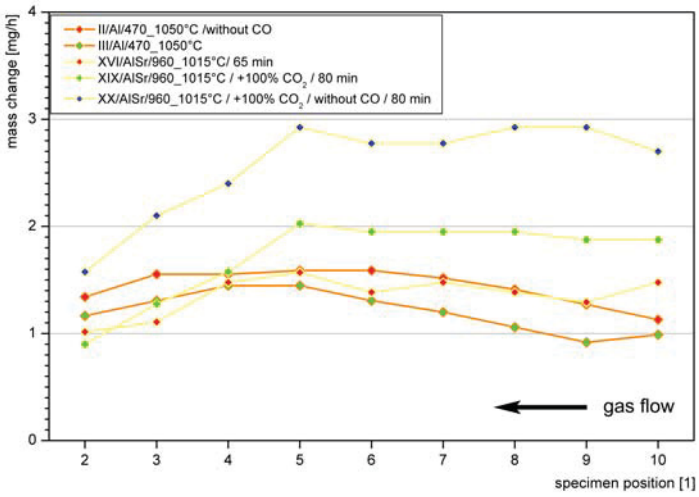

Fig. 4.30: Substrate mass change observed for the aluminium strontium oxide system in the double reactor alignment compared to the reference experiment III and experiment II

The mass changes of experiments XIX and XX are higher than those observed for the reference deposition III and also deposition II. This can be explained by higher CO_2 content in the feed gas.

4.2.2.2 Scanning electron microscopy

The structure of the coatings derived from experiments XVI, XIX and XX, shown in Fig. 4.31, appears more cubic like compared to the reference experiment III. Without CO (experiment XX) a serrated surface could be found on the specimens close to the reactor. A rough, shark fin like structure was found for the samples 6 to 9 (cf. Fig. 4.32 h and i), which are the first ones in gas stream direction. Grain sizes are similar, within the three experiments and over all investigated specimen positions. This can be attributed to similar substrate temperatures, caused by the low temperature gradient. Experiment XIX (cf. Fig. 4.32 d – f) containing CO in the feed gas yielded a relatively smooth surface and a layer thickness of approximately 1 µm (cf. Fig. 4.32 a and b), compared to experiment XX.

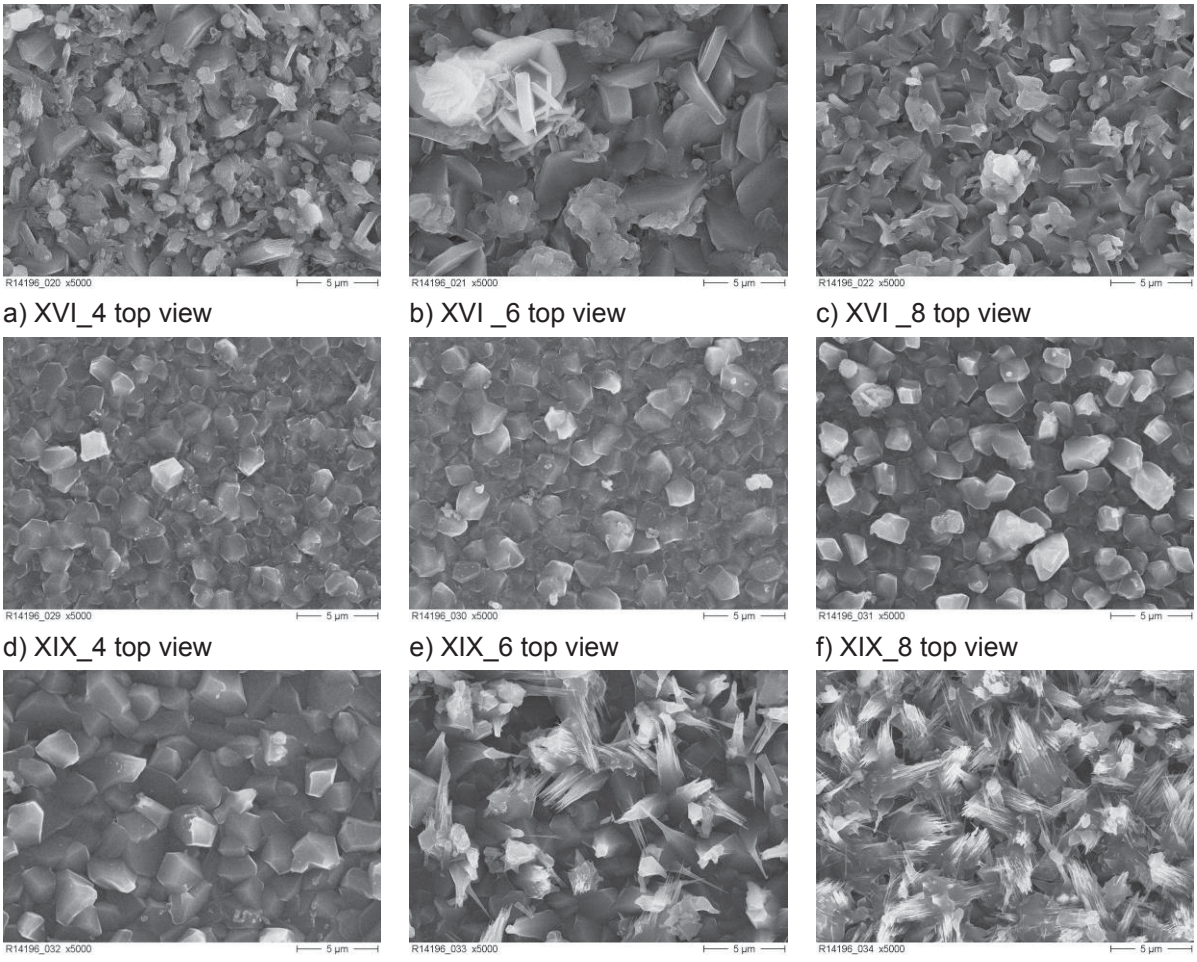

a) XVI_4 top view b) XVI _6 top view c) XVI _8 top view

d) XIX_4 top view e) XIX_6 top view f) XIX_8 top view

g) XX_4 top view h) XX_6 top view i) XX_8 top view

Fig. 4.31: Surface structure obtained within the aluminium strontium oxide system for varying CO and CO_2 contents

It must be noted, that the layer thickness of experiment XVI was less than 1 µm, because of the stopped experiment after 65 min. Clear differences in surface roughness can be seen in the fracture cross-section images (cf. Fig. 4.32 a – d).

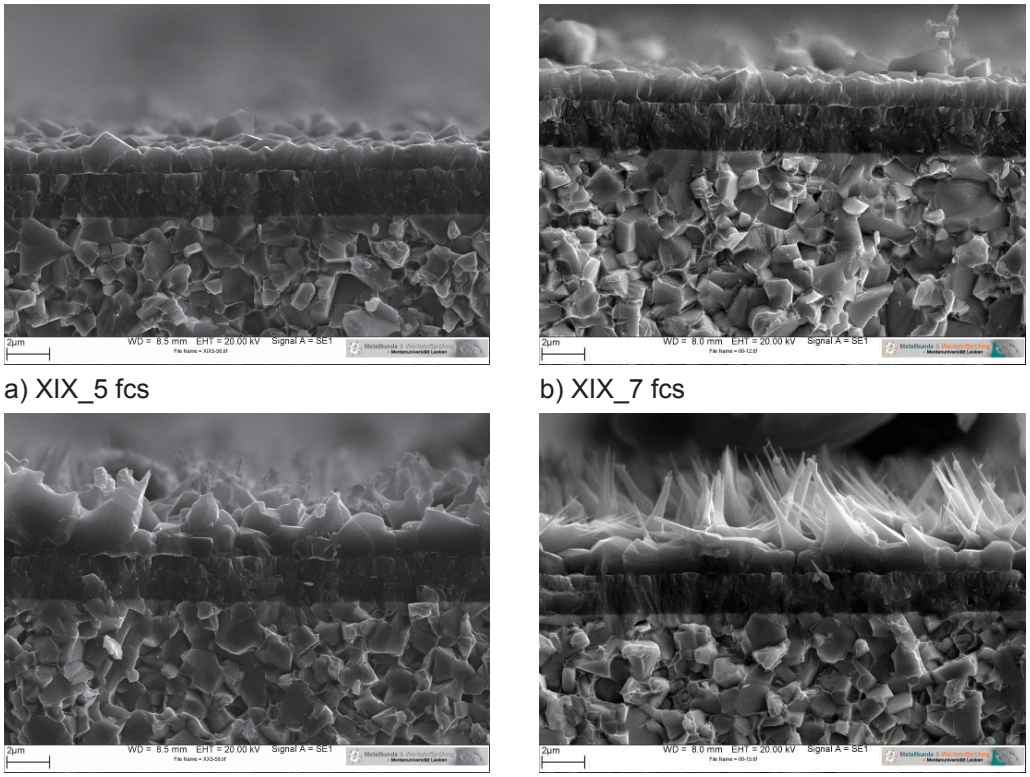

a) XIX_5 fcs b) XIX_7 fcs

c) XX_5 fcs d) XX_7 fcs

Fig. 4.32: Fracture cross-sections (fcs) of deposition XIX and XX

4.2.2.3 Glow discharge optical emission spectroscopy

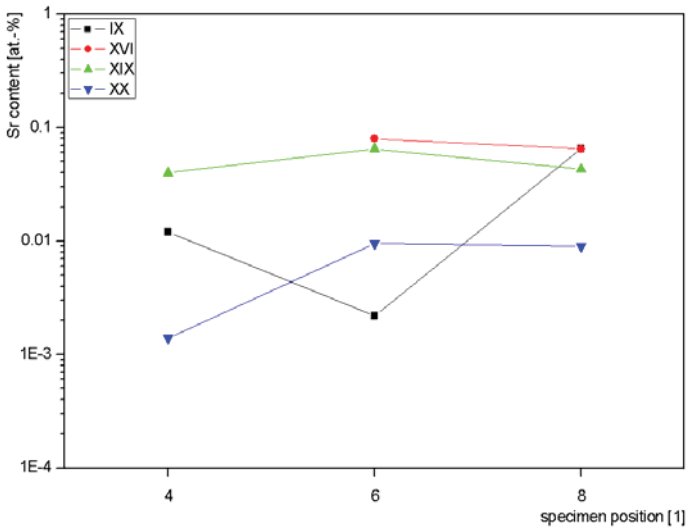

Fig. 4.33: Maximum strontium content of layers deposited using the double reactor alignment compared to the single reactor experiment IX

The maximum strontium contents in the double reactor alignment were quite different. Using a feed gas composition without CO, as applied in experiment XX, generally lower strontium values could be found. Results from the double reactor alignment are within the same order of magnitude compared to the coatings deposited with the single reactor configuration (cf. Fig. 4.33).

The quantitative GDOES analysis of experiment XIX showed strontium accumulation underneath the coating, similar to experiment XI (cf. Fig. 4.26). Much more strontium could be determined at the interface of the TiCN layer as can be seen in Fig. 4.34. It must be conducted that the volatilisation of strontium could not be initiated as efficient as for one of aluminium. Therefore, strontium chloride may be transported to the substrates during the dwell for temperature compensation, before the deposition process was started.

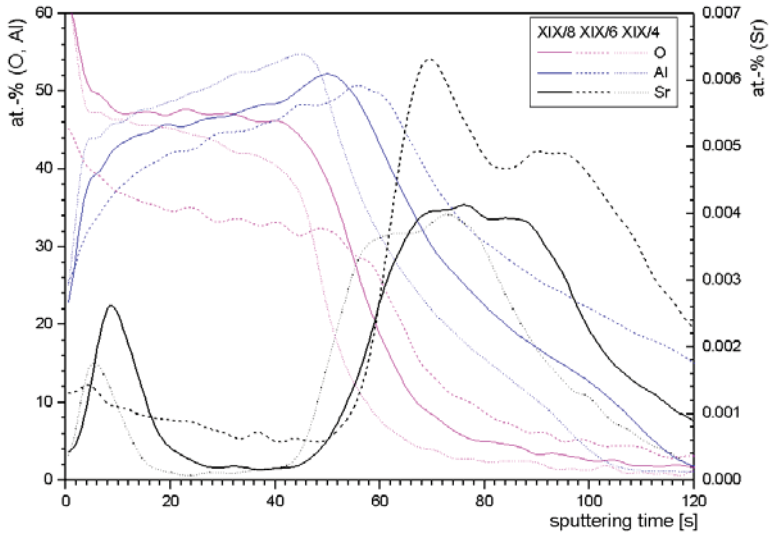

Fig. 4.34: Quantitative GDOES analysis of deposition XIX

4.2.2.4 X-ray diffraction analysis

Except specimen XVI_8 where traces of κ'-Al_2O_3 could be detected, only the α-Al_2O_3 modification was found by XRD analysis. No strontium containing species could be found. A significant amount of $Al_2Ti_7O_{15}$ was determined for specimens XVI_4 and XVI_6, which are marked in green in Tab. 4.7.

Tab. 4.7: Aluminium oxide modifications in the aluminium strontium oxide system, $Al_2Ti_7O_{15}$ was found in the samples shaded in green

	4	6	8
$XVI_{AlSr/960\_1015°C / 65 min}$	α	α	α (κ')
$XIX_{AlSr/960\_1015°C / +100 \%CO2 / 80 min}$	α	α	α
$XX_{AlSr/960\_1015°C / +100 \% CO2 / 80 min}$	α	α	α

5 Discussion and summary

The aim of this thesis was to select and evaluate additional elements for doping of aluminium oxide which may have a positive effect on coating structure and, consequently, on wear and corrosion behaviour. There, chromium, niobium, strontium and tin appeared suitable. The goal was to vaporise, transport and deposit them parallel to aluminium oxide using a laboratory scale horizontal hot-wall reactor with three separate assessable heating zones. Three of the four selected elements (Cr, Sn, Sr) could be transported and incorporated in the layer with a significant amount. The varied parameters within this thesis were the feed gas composition, precursor material and temperature of volatilization and deposition. Applied deposition temperatures were between 700 and 1000 °C. A temperature gradient was applied to the tube furnace, which made it possible to volatilize the precursor at the low temperatures of the first heating zone using a built in molybdenum reactor. The deposition took place in the second and third heating zone, where the substrate material was positioned. For a couple of experiments, this setup was supplemented by a second reactor vessel which was connected to the tube furnace. This one was made of corrosion resistant steel and allowed volatilisation temperatures up to 700 °C. The two different setups are named single- and double reactor alignment, respectively.

Undoped aluminium oxygen system

The undoped aluminium oxide system was used as reference. The applied substrate temperatures were in a magnitude between 830 and 1000 °C. The only quantifiable difference of these experiments was found in titanium oxide modifications within the interface to the precoated TiCN layer, caused by the variation of CO content in feed gas. Also the influence of hydrogen content in feed gas, which led to higher deposition rates, was identical. Deposition rates in a range of 1 µm/h could be achieved.

Aluminium niobium oxide system

Experiments within the aluminium niobium system were performed in single reactor alignment with metallic precursors, mixed in the reaction chamber of the molybdenum reactor. The amount of incorporated niobium was less than 0.02 at.-%. A co-vaporisation of metallic aluminium and metallic niobium was apparently not possible. This may be explained by the high affinity of aluminium to chlorine and the high corrosion resistance of metallic niobium. Nevertheless, the grain size of the coatings decreased only marginal. Bigger particles were found on the surface of specimens, positioned in the lower temperature region of the tube furnace, which

consisted mainly of aluminium oxide. For further investigations within this system, two separate reactors with separate flow meters or niobium salt as precursor material should be used.

Aluminium chromium oxide system

A powder metallurgical alloy containing 20 wt.-% Cr and 80 wt.-% Al was used as precursor material for the aluminium chromium system. Within these experiments which were performed in the single reactor alignment, carbon whisker growth occurred on specimens close to the reactor. It is assumed that the whisker deposition is catalytically promoted by chromium species. Its appearance could be reduced by an increase of CO_2. The addition of CO seemed to be deteriorating, because less carbon whisker growth was observed without CO. The CO_2 content was increased up to 240 % of reference condition, which led to an overproportional layer growth. Growth rates raised up to 4 µm/h. Because of carbon whisker growth, the remaining process gas depleted on carbon containing species and the CO/CO_2-H_2/H_2O equilibrium was shifted towards water gas, which was now available for aluminium oxide deposition. This is a possible explanation for the raised deposition rate. The analysed layers showed partly two different phases. The structure was mainly α-Al_2O_3 and κ-Al_2O_3, but also a number of metastable modifications were found. Chromium could be detected via GDOES in amounts of about 10 at.-% and chromium containing species via XRD analysis.

Aluminium tin oxide system

Experiments dealing with tin were performed in the single and double reactor set-up. For depositions using the single reactor alignment, an aluminium tin alloy containing 20 wt.-% tin was used. Tin oxide formation occurred on the reactor cap where halide gas and oxygen carrier were mixed. Nevertheless, tin was detected by GDOES measurements up to 0.1 at.-%. Compared to the undoped aluminium oxide, a somewhat finer grain size could be observed, similar to niobium doping.

Further experiments were performed in the double reactor alignment using molybdenum substrates and tin chloride as precursor material. The substrate temperature was lowered significantly; hence metastable aluminium oxide species were deposited. Deposition temperatures were varied between 450 °C and 850 °C. Small amounts of tin oxide could be determined via XRD analysis.

Aluminium strontium oxide system

Depositions within the aluminium strontium oxide system were performed in the single and double reactor alignment. Both setups used strontium chloride as precursor. For the single reactor experiment, the strontium chloride was placed

beside the aluminium precursor inside the molybdenum reactor and volatilized below the melting point of the strontium chloride. Traces of strontium could be detected via GDOES. The shape of grains seems to be more cubic like compared to the reference.

Within the double reactor alignment the strontium chloride was heated above the melting point. In contrast to the assumption that higher temperature and liquid state of the precursor should lead to increasing strontium volatilisation, the incorporated strontium amount was unaffected. The resulting structure was comparable to that deposited in the single reactor alignment. Without CO, the surface structure became rough and shark fin like, but the reason for this effect could not be clarified.

Influence of carbon monoxide

Generally the influence of CO in the feed gas could not be quantified clearly within this thesis. In case of aluminium oxide and aluminium strontium oxide deposition, a positive influence by addition of CO was observed. The surface appearance was more uniform within the temperature gradient and the surface was smoother, especially in case of the experiments dealing with the aluminium strontium oxide system. No interfering influence on deposition rate could be observed. A disadvantageous influence of CO could only be found within the aluminium chromium oxide system: The addition of this component forced carbon whisker growth.

Substrate material

Alteration of substrate material led to comparable results. Coatings deposited on cemented carbide as well as molybdenum showed quite similar structures, investigated for depositions within the aluminium chromium oxide system. Molybdenum as substrate material has the advantage that the origin of determined species could be ascertained easier, because there is no precoated layer.

Outlook

For further investigations, the experiences attained within this thesis should be utilised to improve deposition conditions. It is apparently necessary to optimize the feed gas composition depending on the additional element. Especially for the aluminium chromium oxide system this is essential.

The next step for depositing a doped aluminium oxide is to influence the dopant proportion in a controlled way. This can be realised for example by using the double reactor alignment and a transportation of the halide gas species in an inert carrier gas stream. Also a double reactor alignment using two HCl flow meters and two metallic precursors is possible.

The tube furnace offers the opportunity to conduct depositions in vertical alignment, which is similar to production facilities and could further enhance the comparability of experiments. Due to the high density of gaseous metal chloride species, this alignment could also reduce decomposition effects.

The obtained experiences for volatilisation of chromium, niobium, strontium and tin should be useful for volatilisation of elements exhibiting comparable chloride melting points like yttrium and tantalum. An up scaling of the performed aluminium oxide doping approaches, especially on aluminium strontium oxide system, appears to be promising.

6 Literature

1 Ruppi S.: Advances in Chemically Vapour Deposited Wear Resistant Coatings; Journal de Physique IV France 11 (2001); p. Pr3-847-Pr3-859

2 Choy K. L.: Chemical Vapour Deposition of Coatings; Progress in Materials Science 48 (2003); p. 57-170

3 Subramanian C., K. N. Strafford, T. P. Wilks and L. P. Ward: On the Design of Coating Systems: Metallurgical and other Considerations; Journal of Materials Processing Technology 56 (1996); p. 385-397

4 Bobzin K., E. Lugscheider, C. Piñero: New PVD-Coating Concepts for Highly Stressed Tools for Environmentally Compatible Manufacturing Process; Materialwissenschaft und Werkstofftechnik 35 No. 10/11 (2004); p. 851-857

5 Ruppi S.: Deposition, Microstructure and Properties of Texture-Controlled CVD α-Al_2O_3 Coatings; International Journal Refractory Metals & Hard Materials 23 (2005); p. 306-316

6 Prengel H. G., W. R. Pfouts, A. T. Santhanam: State of the Art in Hard Coatings for Carbide cutting tools; Surface and Coatings Technology 102 (1998); p. 183-190

7 Pierson H. O.: Handbook of CVD; 2nd edition Noyes Publications / William Andrew Publishing, LLC, Norwich / New York (1999); p. 36-64

8 Ohring M.: The Material Science of Thin Films; United Kingdom edition, Academic Press, London (1992); p. 22-247

9 Schedler W.: Hartmetall für den Praktiker; VDI Verlag, Düsseldorf (1988); p. 213

10 Atkins P. W.: Physikalische Chemie; 3. Auflage Wiley-VCH Verlagsgesellschaft Weinheim (2002)

11 HSC-Chemistry 5.11; Outokumpu Research, Pori, Finland

12 Jones A. C., P. O'Brien: CVD of Compound Semiconductors; VCH Verlagsgesellschaft (1997); p. 31

13 Carlsson J.-O.: Processes in Interfacial Zones During Chemical Vapour Deposition: Aspects of Kinetics, Mechanisms, Adhesion and Substrate Atom Transport; Thin Solid Films 130 (1985); p. 261-282

14 Sidómiak M.: Theoretical Study of Chemical Vapour Deposition of Transition Metal Compounds; Dissertation Philipps-University Marburg/Lahn (2001); p. 25-48

15 Sipp E., F. Langlais and R. Nasalin: CVD of Y_2O_3 from YCL_3-CO_2-H_2-Ar Gas Mixtures; Journal of Alloys and Compounds, 186 (1992); p. 77-87

16 Catoire L., M. T. Swihart: High-Temperature Kinetics of $AlCl_3$ Decomposition in the Presence of Additives for Chemical Vapour Deposition; Journal of The Electrochemical Society, 149 (5) (2002); p. C261-C267

17 Tan P., J. Müller and D. Neuschütz: Gas-Phase Modeling of the $AlCl_3$ Decomposition in the $AlCl_3$-CO_2-H_2-HCl System for a Hot-Wall CVD Reactor; Journal of The Electrochemical Society 152 (5) (2005); p. C288-C293

18 Sotirchos S. V. and Nitodas S. F.: Development and Valididation of a Mathematical Model for the Chemical Vapour Deposition of Al_2O_3 from Mixtures of $AlCl_3$, CO_2 and H_2; Final Report Grant No.: DE-FG22-96PC96208 (2001);

19 Müller J., D. Neuschütz: Local Deposition Rates of α-Al_2O_3 from $AlCl_3$-CO_2-H_2-HCl Derived with PHOENICS-CVD from Thermogravimetric Measurements in a Hot-Wall Reactor with Long Isothermal Zone; Electrochemical Society Proceedings Volume 2003-08 (2003); p. 186-193

20 Thompson C. V.: Structure Evolution During Processing of Polycrystalline Films; Annual Review of Material Science Vol. 30 (2000); p. 159-190

21 Gottstein G.: Physikalische Grundlagen der Materialkunde; Springer Verlag Berlin-Heidelberg-New York (2001); p. 362-365

22 Petrov I., P. B. Barna, L. Hultman and J. E. Greene : Microstructural Evolution during Film Growth; Journal of Vacuum Science and Technology A21/5 (2003): p. 117-128

23 Barna P. B., M. Adamik: Fundamental Structure Forming Phenomena of Polycrystalline Films and the Structure Zone Models; Thin Solid Films 317 (1998); p. 27-33

24 Oshika T., M. Sato and Nishiyama: Unveiling the Magic of H_2S on the CVD-Al_2O_3 Coating; Journal de Physique IV France 12 (2002); p. 113-120

25 Ruppi S., A. Larsson: Microstructure and Deposition Characteristics of κ-Al_2O_3; Journal de Physique IV France 9 (1999); p. Pr8-349-Pr8-355

26 Cahill D. G. and s.-M. Lee: Thermal Conductivity of κ-Al_2O_3 and α-Al_2O_3 Wear-Resistant coatings; Journal of Applied Physics, 83 (1998); p. 5783-5786

27 Vuorinen S., Karlsson L.: Phase Transformation in Chemically Vapour-Deposited κ-Alumina; Thin Solid Films 214 (1992); p. 132-143

28 Petzold A.: Aluminiumoxid: Rohstoff, Werkstoff, Werkstoffkomponente; 1. Aufllage, Deutscher Verlag für Grundstoffindustrie, Leipzig (1991), p. 45

29 Adamik M., P.B. Barna, I. Tomov: Columnar Structures in Polycrystalline Thin Films Developed by Competitive Growth; Thin Solid Films 317 (1998); p. 64–68

30 Barna P. B., M. Adamik, J. Lábár, L. Kövér, J. Tóth, A. Dévényi, R. Manaila: Formation of Polycrystalline and Microcrystalline Composite Thin Films by Codeposition and Surface Chemical Reaction; Surface and Coatings Technology 125 (2000); p. 147-150

31 Barna P. B., G. Radnóczi and F. M. Reicha: Surface Growth Topography of Grain Boundaries in Al Thin Films; Vacuum 38 (1988); p. 527-532

32 Kathrein M., W. Schintlmeister, W. Wallgram, U. Schleinkofer: Doped CVD Al_2O_3 Coatings for High Performance Cutting Tools; Surface and Coatings Technology 163-164 (2003); p. 181-188

33 JCPDS, Diffraction files database (2006)

34 ASM International: Binary Alloy Phase Diagrams; 2nd edition (1996)

35 M. Lee, E. F. Koch, T. E. Hale: A Study of the Coating-Substrate Interface Layer of an Al_2O_3-Coated Cemented Carbide Cutting Tool; International Journal of Refractory Metals and Hard Materials 14 (1996); p. 335-343

36 Colombier C., J. Peng, H. Altena, B. Lux: Influence of Trace impurities on the α-Al_2O_3 CVD in the $AlX_3/CO_2/H_2$-Systems (X = Cl, Br, I); ; International Journal of Refractory Metals and Hard Materials (1986), p. 82-87

37 Danzinger M., R. Haubner, B. Lux: Influence of Metallic (Cr, W) and Nonmetallic (P, Se, Te) Impurities an Al_2O_3 Deposition by CVD; Surface Modification Technologies III, The Minerals, Metals & Materials Society, Warrendale (1990), p. 829-834

38 Nagano M.: Chemical Vapour Deposition of SnO_2 Thin Films on Rutile Single Crystals; Journal of Crystal Growth 67 (1984); p. 839-644

39 Douy A., M. I. Capron: Crystallisation of Spray-Dried Amorphous Precursors in the SrO–Al_2O_3 System: a DSC study; Journal of the European Ceramic Society 23 (2003); p. 2075–2081

40 Staněk J.: Electric Melting of Glass; Glass Science and Technology, 1; Elsevier Amsterdam-Oxford-New York (1977); p. 213 ff.

41 Kirsch R.: Metals in Glassmaking; Elsevier Amsterdam-London-Tokyo (1993); p. 436 ff.

42 Massazza F.: Il Sistema SrO-AL_2O_3; La Chimica e l'industria XLI-2 (1959), p. 108-115

43 Yoshida H. S. Hashimoto, T Yamamoto: Dopant Effect on Grain Boundary Diffusivity in Polycrystalline Alumina: Acta Materialia 53 (2005); p. 433–440

44 Czirchos H., M. Hennecke: Hütte – Das Ingenieurwesen; 32. Auflage, Springer-Verlag Berlin Heidelberg New York (2004); p. H33

45 Schintlmeister W., W. Wallgram: Wearing Part; EP 0083043 (1981)

46 Colmet R., R. Naslain: Chemical Vapour Deposition of Alumina on Cutting Tool Inserts from $AlCl_3$-H_2-CO_2 Mixtures; Wear, 80 (1982); p. 221-231

47 Halvarsson M.: Microstructural Investigation of CVD α-Al_2O_3/κ-Al_2O_3 Multilayer Coatings; Surface and Coatings Technology, 61 (1993); p. 177-181

48 Fredricsson E.: Chemical Vapour Deposition of Al_2O_3 on TiO; Thin Solid Films 263 (1995); p. 28-36

49 Schierling M., E. Zimmermann and D. Neuschütz: Deposition Kinetics of Al_2O_3 from $AlCl_3$-CO_2-H_2-HCl Gas Mixtures by Thermal CVD in a Hot-Wall Reactor; Journal de Physique France IV 9 (1999), p. Pr8-85-Pr8-91

50 Winchester M. R.: Radio-Frequency Glow Discharge Spectroscopy – A Critical Review; Spectrochimica Acta, B 59 (2004); p. 607-666

51 Horiba Jobin Yvon – Ultra Fast Elemental Depth Profiling – RF Glow Discharge Optical Emmission Spectrometers; http://www.jobinyvon.com/usadivisions/Emission/product/gdprofiler2.pdf; 19th march 2007

52 Bargel H.-J., G. Schulze: Werkstoffkunde; 7. Auflage, Springer Berlin, Heidelberg, New York (2000); p. 133-134

53 Yasuda M., N. Akao, N. Hara and K. Sugimoto: Self-healing Corrosion Protection Ability of Composition-Gradient Al_2O_3-Nb Nanocomposite Thin Films; Journal of The Electrochemical Society, 150 (10) (2003); p. B481-B487

54 Thornton, J. A.: High Rate Thick Film Growth; Ann. Rev. Mat. Sci.(1977); p. 239-260

55 Guse W., H. Saalfeld: Neues Jahrbuch für Mineralogie Monatshefte (1990); p. 217

7 Symbols and abbreviations

a_i	Geometric constant
D	Outer ball diameter
d	Inner ball diameter
d_{hkl}	Interplanar spacing indexed by the Miller indices
E_{ed}	Gibbs free Energy of educts
E_{pr}	Gibbs free Energy of products
F	Applied load
G	Gibbs free Energy
H	Enthalpy
n	Order of diffraction
p	Pressure
Q	Latent heat
R	Ball diameter
r	Track radius
Re	Reynolds' number
S	Entropy
s	Layer thickness
T	Temperature
T_b	Boiling point
T_m	Melting point
T_s	Substrate temperature
U	Intrinsic energy
u_x	Flow density
V	Volume
w	Rotation speed
W	System-performed work
W_{rev}	Reversible work
x	Distance from the inlet
γ_f	Interface tension of film
γ_s	Interface tension of substrate
γ_v	Interface tension of vapour
Δ	Layer thickness
ΔG_V	Free energy change per unit volume
Θ	Contact or diffraction angle
λ	Wavelength
μ	Viscosity
ρ	Mass density

ASTM	American Society for Testing and Materials
CVD	Chemical vapour deposition
DIN	German institute for Standardisation
fcs	Fracture cross-section
GB	Grain boundary
GDOES	Glow discharge optical emission spectroscopy
ISO	International Standardizing Organisation
MCL	Materials Center Leoben
PVD	Physical vapour deposition
S40T	Ceratizit cemented carbide grade
SEM	Scanning electron microscopy
SNUN	Cutting insert geometry according to ISO 1832
TiCN	Titanium carbonitride
XRD	X-ray diffraction

8 Index of tables and figures

9 Appendix

Run	Abreviation	Temperature [°C] Z1	Z2	Z3	RE	TE	Dur. (HCl+CO$_2$) [min]		Gasflow [l/h] Sum	HCl	N_2	N_2 mix CO_2	CO	H_2	H_2	Ar_{RE}	Ar_2		Specimen number 10	9	8	7	6	5	4	3	2	Pre-cursor (in/out/loss)
I	I/Al/470_1050°C	470	660	1050	436	990	170	[l/h]	109.0	4.5	60.0	4.8		3.7	6.0	15.0	15.0	m_v [g]	10.2257	10.1604	10.2263	10.2279	10.2138	10.2294	10.1707	10.2159	10.2296	50.7429
																		m_n [g]	10.2289	10.1635	10.2291	10.2315	10.2171	10.2337	10.1754	10.2200	10.2330	43.9663
																		d_m [mg]	3.2	3.1	2.8	3.6	3.6	4.3	4.7	4.1	3.4	-6.7766
								[%$_v$]	100.0	4.1	55.0	4.4		3.4	5.5	13.8	13.8	T [°C]	777.4	833.1	888.4	936.3	973.9	959.7	1000.0	985.8	953.6	
								[g]	146.2	7.3	75.1	9.4		0.3	0.5	26.8	26.8											[g]/[l$_{HCl}$]
								[%$_{out}$]	100.0	5.0	51.3	6.5		0.2	0.4	18.3	18.3											0.5163
II	II/Al/470_1050°C	470	660	1050	440	1000	170	[l/h]	112.1	4.5	60.0	4.8		**5.0**	**7.8**	15.0	15.0	m_v [g]	10.2289	10.2374	10.2389	10.2205	10.2276	10.2281	10.1097	10.2115	10.1921	50.0612
																		m_n [g]	10.2321	10.2410	10.2429	10.2248	10.2321	10.2326	10.1141	10.2159	10.1959	43.1015
																		d_m [mg]	3.2	3.6	4.0	4.3	4.5	4.5	4.4	4.4	3.8	-6.9597
								[%$_v$]	100.0	4.0	53.5	4.3		4.5	7.0	13.4	13.4	T [°C]	777.4	833.1	888.4	936.3	973.9	959.7	1000.0	985.8	953.6	
								[g]	146.5	7.3	75.1	9.4		0.5	0.7	26.8	26.8	s [µm]				2.4		2.3				[g]/[l$_{HCl}$]
								[%$_{out}$]	100.0	5.0	51.2	6.4		0.3	0.5	18.3	18.3											0.5303
III	III/Al/470_1050°C	470	660	1050	437	1000	170	[l/h]	100.5	4.5	49.8	4.8	2.7	2.7	6.0	15.0	15.0	m_v [g]	10.2141	10.2246	10.2299	10.2121	10.2321	10.2422	10.2210	10.2156	10.2313	50.0483
																		m_n [g]	10.2169	10.2272	10.2329	10.2155	10.2358	10.2463	10.2251	10.2193	10.2346	41.9685
																		d_m [mg]	2.8	2.6	3.0	3.4	3.7	4.1	4.1	3.7	3.3	-8.0798
								[%$_v$]	100.0	4.5	49.6	4.8	2.7	2.7	6.0	14.9	14.9	T [°C]	777.4	833.1	888.4	936.3	973.9	959.7	1000.0	985.8	953.6	
								[g]	136.7	7.3	62.3	9.4	3.4	0.2	0.5	26.8	26.8					2.0		2.0				[g]/[l$_{HCl}$]
								[%$_{out}$]	100.0	5.4	45.6	6.9	2.5	0.2	0.4	19.6	19.6											0.6156
IV	IV/AlSn/470_1050°C	470	660	1050	442	1001	170	[l/h]	100.5	4.5	49.8	4.8	2.7	2.7	6.0	15.0	15.0	m_v [g]	10.2161	10.2237	10.1484	10.2364	10.1793	10.2355	10.2160	10.2042	10.2067	50.7665
																		m_n [g]	10.2183	10.2262	10.1513	10.2398	10.1830	10.2395	10.2199	10.2079	10.2097	42.7900
																		d_m [mg]	2.2	2.5	2.9	3.4	3.7	4.0	3.9	3.7	3.0	-7.9765
								[%$_v$]	100.0	4.5	49.6	4.8	2.7	2.7	6.0	14.9	14.9	T [°C]	777.40	833.10	888.40	936.30	973.90	959.70	1000.00	985.80	953.60	
								[g]	136.7	7.3	62.3	9.4	3.4	0.2	0.5	26.8	26.8					1.8		1.8				[g]/[l$_{HCl}$]
								[%$_{out}$]	100.0	5.4	45.6	6.9	2.5	0.2	0.4	19.6	19.6											0.6077
V	V/AlSn/470_1000°C	470	660	1000	445	954	170	[l/h]	100.5	4.5	49.8	4.8	2.7	2.7	6.0	15.0	15.0	m_v [g]	10.2306	10.2247	10.1064	10.1494	10.1433	10.1958	10.1536	10.2247	10.2114	49.9064
																		m_n [g]	10.2328	10.2271	10.1096	10.1530	10.1471	10.1995	10.1571	10.2276	10.2138	41.3359
																		d_m [mg]	2.2	2.4	3.2	3.6	3.8	3.7	3.5	2.9	2.4	-8.5705
								[%$_v$]	100.0	4.5	49.6	4.8	2.7	2.7	6.0	14.9	14.9	T [°C]	730.40	786.10	841.40	889.90	926.90	948.70	953.00	938.80	906.60	
								[g]	136.7	7.3	62.3	9.4	3.4	0.2	0.5	26.8	26.8											[g]/[l$_{HCl}$]
								[%$_{out}$]	100.0	5.4	45.6	6.9	2.5	0.2	0.4	19.6	19.6											0.6530
VI	VI/AlSn/470_1050°C / +30% H2	470	660	1050	441	1000	170	[l/h]	102.5	4.5	49.8	4.8	2.7	2.7	**8.0**	15.0	15.0	m_v [g]	10.2175	10.1507	10.1812	10.1163	10.1431	10.1086	10.1364	10.2046	10.2278	45.7161
																		m_n [g]	10.2208	10.1537	10.1846	10.1201	10.1472	10.1129	10.1406	10.2086	10.2314	37.4130
																		d_m [mg]	3.3	3.0	3.4	3.8	4.1	4.3	4.2	4.0	3.6	-8.3031
								[%$_v$]	100.0	4.4	48.6	4.7	2.6	2.6	7.8	14.6	14.6	T [°C]	777.40	833.10	888.40	936.30	973.90	959.70	1000.00	985.80	953.60	
								[g]	136.9	7.3	62.3	9.4	3.4	0.2	0.7	26.8	26.8											[g]/[l$_{HCl}$]
								[%$_{out}$]	100.0	5.4	45.5	6.9	2.5	0.2	0.5	19.5	19.5											0.6326
VII	VII/AlNb/470_1050°C	470	660	1050	440	1000	170	[l/h]	100.5	4.5	49.8	4.8	2.7	2.7	6.0	15.0	15.0	m_v [g]	10.2224	10.1496	10.1841	10.1885	10.2285	10.1685	10.1506	10.1757	10.1615	49.9861
																		m_n [g]	10.2242	10.1514	10.1863	10.1913	10.2318	10.1722	10.1546	10.1793	10.1643	42.4656
																		d_m [mg]	1.8	1.8	2.2	2.8	3.3	3.7	4.0	3.6	2.8	-7.5205
								[%$_v$]	100.0	4.5	49.6	4.8	2.7	2.7	6.0	14.9	14.9	T [°C]	777.40	833.10	888.40	936.30	973.90	959.70	1000.00	985.80	953.60	
								[g]	136.7	7.3	62.3	9.4	3.4	0.2	0.5	26.8	26.8	s [µm]				1.6		1.7				[g]/[l$_{HCl}$]
								[%$_{out}$]	100.0	5.4	45.6	6.9	2.5	0.2	0.4	19.6	19.6											0.5730
VIII	VIII/AlNb/470_1050°C	470	660	1050	449	1002	170	[l/h]	101.0	4.5	49.8	4.8	2.7	2.7	6.0	**4.5**	**26.0**	m_v [g]	10.2127	10.1638	10.2175	10.2006	10.2216	10.1726	10.1591	10.1500	10.1568	77.2712
																		m_n [g]	10.2158	10.1666	10.2209	10.2042	10.2257	10.1770	10.1633	10.1539	10.1600	69.1397
																		d_m [mg]	3.1	2.8	3.4	3.6	4.1	4.4	4.2	3.9	3.2	-8.1315
								[%$_v$]	100.0	4.5	49.3	4.8	2.7	2.7	5.9	4.5	25.7	T [°C]	777.40	833.10	888.40	936.30	973.90	959.70	1000.00	985.80	953.60	
								[g]	137.6	7.3	62.3	9.4	3.4	0.2	0.5	8.0	46.4											[g]/[l$_{HCl}$]
								[%$_{out}$]	100.0	5.3	45.3	6.9	2.5	0.2	0.4	5.8	33.7											0.6195
IX	IX/AlSr/640_1035°C	640	820	1035	599	999	170	[l/h]	100.5	4.5	49.8	4.8	2.7	2.7	6.0	15.0	15.0	m_v [g]	10.2201	10.1685	10.1508	10.2196	10.2218	10.1505	10.1664	10.1500	10.2242	50.5212
																		m_n [g]	10.2220	10.1707	10.1532	10.2224	10.2249	10.1540	10.1694	10.1528	10.2209	38.5240
																		d_m [mg]	1.9	2.2	2.4	2.8	3.1	3.5	3.0	2.8	-3.3	-11.9972
								[%$_v$]	100.0	4.5	49.6	4.8	2.7	2.7	6.0	14.9	14.9	T [°C]										
								[g]	136.7	7.3	62.3	9.4	3.4	0.2	0.5	26.8	26.8	s [µm]				1.7		1.5				[g]/[l$_{HCl}$]
								[%$_{out}$]	100.0	5.4	45.6	6.9	2.5	0.2	0.4	19.6	19.6											0.9141
X	X/AlCr/640_1035°C	640	820	1035	597	998	170	[l/h]	100.5	4.5	49.8	4.8	2.7	2.7	6.0	15.0	15.0	m_v [g]	10.1411	10.2267	10.1382	10.1914	10.2319	10.2298	10.1750	10.1721	10.2306	42.7985
																		m_n [g]	10.4368	10.3882	10.2304	10.2032	10.2406	10.2390	10.1833	10.1796	10.2361	36.7660
																		d_m [mg]	295.7	161.5	92.2	11.8	8.7	9.2	8.3	7.5	5.5	-6.0325
								[%$_v$]	100.0	4.5	49.6	4.8	2.7	2.7	6.0	14.9	14.9	T [°C]										
								[g]	136.7	7.3	62.3	9.4	3.4	0.2	0.5	26.8	26.8											[g]/[l$_{HCl}$]
								[%$_{out}$]	100.0	5.4	45.6	6.9	2.5	0.2	0.4	19.6	19.6											0.4596
XI	XI/AlCr/640_1035°C	640	820	1035			170	[l/h]	80.5	4.5	**33.2**	**3.2**	**1.8**	**1.8**	6.0	15.0	15.0	m_v [g]	10.2003	10.2238	10.2175	10.1984	10.2312	10.1422	10.2114	10.1490	10.1766	42.4939
																		m_n [g]	10.3444	10.3327	10.2708	10.2034	10.2370	10.1479	10.2170	10.1543	10.1810	36.9242
																		d_m [mg]	144.1	108.9	53.3	5.0	5.8	5.7	5.6	5.3	4.4	-5.5697
								[%$_v$]	100.0	5.6	41.2	4.0	2.2	2.2	7.5	18.6	18.6	d_m [mg/cm²h]	8.87	6.70	3.28	0.31	0.36	0.35	0.34	0.33	0.27	
								[g]	111.6	7.3	41.5	6.3	2.3	0.2	0.5	26.8	26.8											[g]/[l$_{HCl}$]
								[%$_{out}$]	100.0	6.6	37.2	5.6	2.0	0.1	0.5	24.0	24.0											0.4244
XII	XII/AlCr/640_1035°C /+100 % CO2	640	820	1035			170	[l/h]	105.3	4.5	49.8	**9.6**	2.7	2.7	6.0	15.0	15.0	m_v [g]	10.1485	10.1426	10.2378	10.2383	10.1114	10.2049	10.1633	10.2252	10.1562	34.1564
																		m_n [g]	10.3181	10.1820	10.2491	10.2467	10.1195	10.2140	10.1716	10.2324	10.1620	28.3562
																		d_m [mg]	169.6	39.4	11.3	8.4	8.1	9.1	8.3	7.2	5.8	-5.8002
								[%$_v$]	100.0	4.3	47.3	9.1	2.6	2.6	5.7	14.2	14.2	d_m [mg/cm²h]	10.44	2.42	0.70	0.52	0.50	0.56	0.51	0.44	0.36	
								[g]	146.1	7.3	62.3	18.9	3.4	0.2	0.5	26.8	26.8	s [µm]				3.2		4.6				[g]/[l$_{HCl}$]
								[%$_{out}$]	100.0	5.0	42.6	12.9	2.3	0.2	0.4	18.3	18.3											0.4419
XIII	XIII/AlCr/640_1035°C /+140 % CO2	640	820	1035			170	[l/h]	107.5	4.5	49.8	**11.8**	2.7	2.7	6.0	15.0	15.0	m_v [g]	10.1981	10.1466	10.1870	10.2054	10.1810	10.1395	10.1602	10.2058	10.1669	25.3825
																		m_n [g]	10.3415	10.1879	10.2013	10.2228	10.2045	10.1696	10.1965	10.2278	10.1747	19.6367
																		d_m [mg]	143.4	41.3	14.3	17.4	23.5	30.1	36.3	22.0	7.8	-5.7458
								[%$_v$]	100.0	4.2	46.3	11.0	2.5	2.5	5.6	14.0	14.0	d_m [mg/cm²h]	8.83	2.54	0.88	1.07	1.45	1.85	2.23	1.35	0.48	
								[g]	150.5	7.3	62.3	23.2	3.4	0.2	0.5	26.8	26.8					5.0		12.0				[g]/[l$_{HCl}$]
								[%$_{out}$]	100.0	4.9	41.4	15.4	2.2	0.2	0.4	17.8	17.8											0.4378
XIV	XIV/AlCr(Mo)/640_1035°C / -50% gas	640	820	1035			170	[l/h]	**52.4**	**2.0**	**24.9**	**4.8**	**1.4**	**1.4**	**3.0**	**7.5**	**7.5**	m_v [g]	6.8089	6.8636	6.8442	6.8547	6.8889	6.8322	6.8154	6.8703	6.8159	25.5394
																		m_n [g]	6.8131	6.8668	6.8482	6.8597	6.8957	6.8401	6.8230	6.8773	6.8210	22.2541
																		d_m [mg]	4.2	3.2	4.0	5.0	6.8	7.9	7.6	7.0	5.1	-3.2853
								[%$_v$]	100.0	3.8	47.5	9.2	2.6	2.6	5.7	14.3	14.3	d_m [mg/cm²h]	0.26	0.20	0.25	0.31	0.42	0.49	0.47	0.43	0.31	
								[g]	72.7	3.3	31.1	9.4	1.7	0.1	0.3	13.4	13.4											[g]/[l$_{HCl}$]
								[%$_{out}$]	100.0	4.5	42.9	13.0	2.3	0.2	0.4	18.4	18.4											0.5632
XV	XV/AlSn(Mo)/470_1050°C	470	690	1050	332	1005	170	[l/h]	105.5	4.5	49.8	**9.8**	2.7	2.7	6.0	15.0	15.0	m_v [g]	6.8562	6.8198	6.8400	6.8049	6.8712	6.9131	6.8859	6.7935	6.8466	51.0162
																		m_n [g]	6.8596	6.8234	6.8438	6.8113	6.8791	6.9182	6.8922	6.7985	6.8503	42.1986
																		d_m [mg]	3.4	3.6	3.8	6.4	7.9	5.1	6.3	5.0	3.7	-8.8176
								[%$_v$]	100.0	4.3	47.2	9.3	2.6	2.6	5.7	14.2	14.2	d_m [mg/cm²h]	0.21	0.22	0.23	0.39	0.49	0.31	0.39	0.31	0.23	
								[g]	146.5	7.3	62.3	19.3	3.4	0.2	0.5	26.8	26.8											[g]/[l$_{HCl}$]
								[%$_{out}$]	100.0	5.0	42.5	13.1	2.3	0.2	0.4	18.3	18.3											0.6718
XVI	XVI/AlSr/960_1015°C	960	980	1015	887	1002	**65**	[l/h]	100.5	4.5	49.8	4.8	2.7	2.7	6.0	14.9	14.9	m_v [g]	10.1454	10.1510	10.1668	10.1514	10.1862	10.2220	10.1490	10.1456	10.1719	8.2770
																		m_n [g]	10.1470	10.1524	10.1683	10.1530	10.1877	10.2237	10.1506	10.1468	10.1730	7.6366
																		d_m [mg]	1.6	1.4	1.5	1.6	1.5	1.7	1.6	1.2	1.1	-0.6404
								[%$_v$]	100.0	4.5	49.6	4.8	2.7	2.7	6.0	14.9	14.9	d_m [mg/cm²h]	0.26	0.23	0.24	0.26	0.24	0.27	0.26	0.19	0.18	
								[g]	136.7	7.3	62.3	9.4	3.4	0.2	0.5	26.8	26.8											[g]/[l$_{HCl}$]
								[%$_{out}$]	100.0	5.4	45.6	6.9	2.5	0.2	0.4	19.6	19.6											0.1220
XVII	XVII/AlCr/640_1035°C /ohne CO	640	820	1035	596	1001	170	[l/h]	**98.0**	**4.5**	**50.0**	**4.8**		**2.7**	**6.0**	**15.0**	**15.0**	m_v [g]	10.2235	10.1630	10.1366	10.2125	10.1785	10.1541	10.1543	10.1772	10.1747	22.1900
																		m_n [g]	10.2758	10.1838	10.1469	10.2213	10.1898	10.1677	10.1672	10.1865	10.1832	16.5999
																		d_m [mg]	52.3	20.8	10.3	8.8	11.3	13.6	12.9	9.3	8.5	-5.5901
								[%$_v$]	100.0	4.6	51.0	4.9	0.0	2.8	6.1	15.3	15.3	d_m [mg/cm²h]	3.22	1.28	0.63	0.54	0.70	0.84	0.79	0.57	0.52	
								[g]	133.6	7.3	62.5	9.4	0.0	0.2	0.5	26.8	26.8	s [µm]				4.1		6.7				[g]/[l$_{HCl}$]
								[%$_{out}$]	100.0	5.5	46.8	7.1	0.0	0.2	0.4	20.0	20.0											0.4259
XVIII	XVIII/AlSr/960_1015°C	960	980	1015	887	1002	170	[l/h]	100.5	4.5	49.8	4.8	2.7	2.7	6.0	15.0	15.0	m_v [g]	10.1813	10.2203	10.2235	10.1546	10.2289	10.1401	10.1928	10.2048	10.2211	7.6366
																		m_n [g]	10.1831	10.2207	10.2243	10.1540	10.2248	10.1366	10.1927	10.2059	10.2234	0.0000
																		d_m [mg]	1.8	0.4	0.8	-0.6	-4.1	-3.5	-0.1	1.1	2.3	-7.6366
								[%$_v$]	100.0	4.5	49.6	4.8	2.7	2.7	6.0	14.9	14.9	d_m [mg/cm²h]	0.11	0.02	0.05	-0.04	0.25	0.22	-0.01	0.07	0.14	
								[g]	136.7	7.3	62.3	9.4	3.4	0.2	0.5	26.8	26.8											[g]/[l$_{HCl}$]
								[%$_{out}$]	100.0	5.4	45.6	6.9	2.5	0.2	0.4	19.6	19.6											0.5818
XIX	XIX/AlSr/960_1015°C / +100% CO2	960	980	1015	887	1002	80	[l/h]	105.3	4.5	49.8	**9.6**	2.7	2.7	6.0	15.0	15.0	m_v [g]	10.1473	10.1663	10.2097	10.2161	10.2171	10.2271	10.1487	10.2119	10.2260	4.2395
																		m_n [g]	10.1498	10.1688	10.2123	10.2187	10.2197	10.2298	10.1508	10.2136	10.2272	4.2349
																		d_m [mg]	2.5	2.5	2.6	2.6	2.6	2.7	2.1	1.7	1.2	-0.0046
								[%$_v$]	100.0	4.3	47.3	9.1	2.6	2.6	5.7	14.2	14.2	d_m [mg/cm²h]	0.33	0.33	0.34	0.34	0.34	0.35	0.27	0.22	0.16	
								[g]	146.1	7.3	62.3	18.9	3.4	0.2	0.5	26.8	26.8	s [µm]				1.2		1.2				[g]/[l$_{HCl}$]
								[%$_{out}$]	100.0	5.0	42.6	12.9	2.3	0.2	0.4	18.3	18.3											0.0007
XX	XX/AlSr/960_1015°C	960	980	1015	887	1002	80	[l/h]	102.8	4.5	50.0	**9.6**		2.7	6.0	15.0	15.0	m_v [g]	10.1244	10.2034	10.1492	10.1578	10.1490	10.1621	10.2236	10.2174	10.1640	4.2349
																		m_n [g]	10.1280	10.2073	10.1531	10.1615	10.1527	10.1660	10.2268	10.2202	10.1661	4.2234
																		d_m [mg]	3.6	3.9	3.9	3.7	3.7	3.9	3.2	2.8	2.1	-0.0115
								[%$_v$]	100.0	4.4	48.6	9.3	0.0	2.6	5.8	14.6	14.6	d_m [mg/cm²h]	0.47	0.51	0.51	0.48	0.48	0.51	0.42	0.37	0.27	
								[g]	143.0	7.3	62.5	18.9	0.0	0.2	0.5	26.8	26.8											[g]/[l$_{HCl}$]
								[%$_{out}$]	100.0	5.1	43.7	13.2	0.0	0.2	0.4	18.7	18.7											0.0018
XXI	XXI/AlSn(Mo)/300_700°C / +100% CO2	300	500	700	298	665	170	[l/h]	100.5	4.5	49.8	4.8	2.7	2.7	6.0	15.0	15.0	m_v [g]	6.7985	6.8546	6.8390	6.8146	6.8515	6.9897	6.8155	6.7878	6.8549	49.7264
																		m_n [g]	6.7936	6.8500	6.8367	6.8113	6.8485	6.9877	6.8140	6.7866	6.8537	41.7426
																		d_m [mg]	-4.9	-4.6	-2.3	-3.3	-3.0	-2.0	-1.5	-1.2	-1.2	-7.9838
								[%$_v$]	100.0	4.5	49.6	4.8	2.7	2.7	6.0	14.9	14.9	d_m [mg/cm²h]	-0.30	-0.28	-0.14	-0.20	-0.18	-0.12	-0.09	-0.07	-0.07	
								[g]	136.7	7.3	62.3	9.4	3.4	0.2	0.5	26.8	26.8											[g]/[l$_{HCl}$]
								[%$_{out}$]	100.0	5.4	45.6	6.9	2.5	0.2	0.4	19.6	19.6											0.6083
XXII	XXII/AlSn(Mo)/272_850°C	272	501	850	292	784	170	[l/h]	100.5	4.5	49.8	4.8	2.7	2.7	6.0	15.0	15.0	m_v [g]	6.8533	6.8708	6.8364	6.8392	6.8108	6.8139	6.8145	6.8333	6.8515	49.7982
																		m_n [g]	6.8543	6.8721	6.8386	6.8415	6.8128	6.8158	6.8164	6.8350	6.8528	40.6783
																		d_m [mg]	1.0	1.3	2.2	2.3	2.0	1.9	1.9	1.7	1.3	-9.1199
								[%$_v$]	100.0	4.5	49.6	4.8	2.7	2.7	6.0	14.9	14.9	d_m [mg/cm²h]	0.06	0.08	0.14	0.14	0.12	0.12	0.12	0.10	0.08	
								[g]	136.7	7.3	62.3	9.4	3.4	0.2	0.5	26.8	26.8											[g]/[l$_{HCl}$]
								[%$_{out}$]	100.0	5.4	45.6	6.9	2.5	0.2	0.4	19.6	19.6											0.6948

Specimen position not used / Value not accessable